Experimental Investigation of Small-Scale Breaking Waves: Flow Visualization across the Air-Water Interface

by

Angus Kai McDonald

Submitted to the Department of Ocean Engineering
in partial fulfillment of the requirements for the degree of

Master of Science in Ocean Engineering
at the
MASSACHUSETTS INSTITUTE OF TECHNOLOGY

May 2005 [June 2005]

Signature of Author...
Department of Ocean Engineering
May 6, 2005

Certified by...
Alexandra H. Techet
Assistant Professor of Mechanical and Ocean Engineering

Accepted by...
Michael S. Triantafyllou
Professor of Mechanical and Ocean Engineering
Chairman, Departmental Committee on Graduate Students

Experimental Investigation of Small-Scale Breaking Waves: Flow Visualization across the Air-Water Interface

by

Angus Kai McDonald

Submitted to the Department of Ocean Engineering
On May 6, 2005 in Partial Fulfillment of the
Requirements for the Degree of Master of Science in
Ocean Engineering

ABSTRACT

The dynamics of breaking waves significantly affect air-sea fluxes of heat, momentum, mass and energy across the ocean interface. Breaking waves also contribute considerable loading to offshore and coastal structures, and furthermore, the quasi-steady bow wave on a ship increases drag and ease of detection by the bubbly wake. However, the complexity of the phenomenon has severely limited our ability to describe it and predict its occurrence. Research has typically involved field observations, controlled laboratory studies, and numerical simulations. A recent simulation presented new information about local energy dissipation and the coupled air-water effects of small breaking waves. In light of these findings, the objective of this thesis is to experimentally study small-scale breaking waves and examine the combined air-water flow fields using advanced visualization techniques.

This research was performed in a narrow wavetank which was 2.5m long. Waves were generated with a hinged paddle and breaking occurred as the train propagated up a 15 degree slope to a level plateau. Waves were studied using surface piercing wave probes, high speed video, and Particle Image Velocimetry (PIV). Surface tension was found to have a significant effect on the breaking dynamics at this scale. After a thorough exploration of its effect on surface tension, isopropyl alcohol was added to distilled water in a 10% solution by volume, which reduced the surface tension to approximately 43 dynes/cm. A wave breaking database was created which included 26 different wave trains over a frequency band of 1.5-4Hz. The corresponding Weber numbers ranged from 400 through 14,600 with Reynolds numbers from 38,200 through 280,000. The wave probes measured significant potential energy losses to breaking which are expected. The air-water flow fields are studied by seeding the air and water with reflective particle and processing the video results with PIV software. Qualitative results from PIV including vector and vorticity maps agree well with previous theory and recent numerical results.

Thesis Supervisor: Alexandra H. Techet
Title: Assistant Professor of Mechanical and Ocean Engineering

Acknowledgements

As I reflect upon the conclusion of my graduate studies, I must first express my sincere gratitude to my advisor, Professor Alex Techet, for her guidance and support throughout this process. Her friendly demeanor and tireless devotion to my fellow students and me has made this experience memorable. I also wish to thank Dr. Kelli Hendrickson, our local breaking wave expert, for providing direction and scientific insight to this transplanted California surfer who knew of mushy waves and barrels but nothing of parasitic capillaries or plunging breakers. On the experimental side, I wish to express my appreciation to Dr. Susan Brown for passing on valuable knowledge and sacrificing both time and energy to help me complete my research.

I am also thankful to the UROP students who helped make this research possible: Chris Rhodes for his assistance with the motor wiring, Jesse Chandler for spearheading the wave probe development, and Alex Hornstein for his all-around engineering talent. The staff and equipment at the Edgerton Center were vital to this research. I would especially like to thank Fred Cote for his instruction and advice in the Machine Shop, and Anthony Caloggero for his assistance with high-speed video.

Finally, I would like to thank my family for their unceasing love and support. My inspiration for ocean research and breaking waves comes from surfing, and I will always cherish the memories of our many surf trips together.

Contents

Chapter 1

Introduction

Understanding the nature of surface waves on water has been important for as long as humans have engaged the seas. The dangers of violent breaking waves must have been of vital interest to early fishermen, ocean traders, and all others whose livelihood depended upon their successful nautical ventures. Early explorers were particularly vulnerable, as they often put to sea in ships barely longer than most contemporary cruising yachts [37]. While formal investigation of waves in the past couple centuries has produced some valuable insight, the complexity of the dynamics has severely limited knowledge of this non-linear wave phenomena.

The same perils that haunted early ocean-goers still exist today, as vessels are lost in steep and breaking seas. Severe waves also influence the mapping of shipping lanes and navigation routes. Furthermore, the use of the deep ocean in the expanding search for crude oil necessitates accurate prediction of offshore operating conditions. Breaking waves contribute significant dynamic loading to offshore platforms and other fixed structures [25], and these loads can cause failure due to fatigue or sheer magnitude of the wave force. Coastal areas are also at risk, as breaking waves exacerbate beach erosion and can damage piers, jetties, seawalls or other coastal structures. The tragic effects of the recent Asian tsunami illustrate the destructive potential of massive wave disturbances.

On a global scale, breaking waves can influence atmospheric and oceanic circulations. To begin with, breaking effects heat transfer when the warmer surface layer mixes with cooler water below. Breaking events also convert some momentum flux of the wave field into ocean currents. Turbulence and bubble entrainment from broken waves enhance the gas transfer from the air to the water in addition to dissipating surface energy. Each of these changes has a direct influence on the circulations which effect global climate. For example, gas transfer in the oceans is important to the reduction of atmospheric CO_2 because the seas naturally uptake around two Gigatons of carbon (~7 Gt CO_2) per year through the carbon cycle [5]. The extent to which wave breaking plays a role in this process is not well understood.

The study of breaking waves is also important in ship design, as the breaking bow wave off a traveling ship is partially responsible for the bubbly wake and is a significant source of drag. Naval defense forces are interested in minimizing the easily detectable wake signature in their design of faster stealth surface crafts. Additionally, the resistance associated with breaking bow wave can account for up to 15% of the total drag on ship [3]. Understanding the breaking bow wave will allow for design of more efficient vessels across the maritime industry as well as making remote detection of the bubbly wake more difficult.

Aside from their significance in engineering and scientific realm, breaking waves inspire awe by the nature of their aesthetic form. Musicians, writers, artists, and poets have all reflected upon and conveyed the dynamical wonder of breakers in their creative expressions. In the following poem from *Leaves of Grass*, Walt Whitman (1819-1892) eloquently describes features of breaking waves that researchers still struggle to characterize today:

“After the Sea-Ship”

After the sea-ship, after the whistling winds,
After the white-gray sails taut to their spars and ropes,
Below, a myriad myriad waves hastening, lifting up their necks,
Tending in ceaseless flow toward the track of the ship,
Waves of the ocean bubbling and gurgling, blithely prying,
Waves, undulating waves, liquid, uneven, emulous waves,
Toward that whirling current, laughing and buoyant, with curves,
Where the great vessel, sailing and tacking displaced the surface,
Larger and smaller waves in the spread of the ocean yearnfully
    flowing,
The wake of the sea-ship after she passes, flashing and frolicsome
    under the sun,
A motley procession with many a fleck of foam and many fragments,
Following the stately and rapid ship, in the wake following.
-Walt Whitman

Though significant advances have been made since the time of Whitman, most oceanographic or engineering descriptions of the ocean surface are still based upon the linear wave theory developed in the nineteenth century [37]. Steep and breaking waves are inherently nonlinear, and Stokes initially investigated weak nonlinear effects on surface waves in 1847 [49]. He established that the theoretical limit to wave steepness is, $ak = 0.4422$, where a is the wave amplitude and k is the wavenumber. Equivalently, this limit implies a 120 degree corner flow at the wave crest. At this angle, the speed of the particles in the crest matches the phase speed and anything steeper will lead to a breaking wave. Experiments have shown that waves tend to break well before reaching the Stokes limit. One type of breaker is caused by Benjamin-Feir instabilities, where the instability in a wavetrain consisting of a central frequency with small amplitude sidebands results in breaking after many wave periods (O(100) cycles) [19]. Numerical simulations have shown breaking due to Benjamin-Feir instabilities for wave slopes as small as 0.1 [33].

In the open ocean, waves break as a result of wave-wave, wave-current, and wind-wave interactions. Near the shore and in rivers, waves break due to interaction with the shallow bottom. The relative fluid motion against obstacles can also cause breaking, such as in the case of the ship bow wave. Wave-wave interaction can be caused by dispersive focusing, where different wave components converge and cause breaking. Further details of this process and a laboratory method of wave focusing are detailed in Chapter 4.

Waves propagating against a current may also break. This occurrence can be observed as waves travel against a rip current near the shore or toward an estuary during an outgoing tide. The reflection of the wave energy off the current leads to breaking. A trip to the beach during afternoon onshore winds can demonstrate breaking due to wind-wave interaction. Such whitecaps have been observed to begin at wind speeds of approximately 3 m s^{-1} [37]. The many different mechanisms leading to wave breaking along with the intrinsic instabilities result in no two breaking events being exactly alike in nature. Despite these differences, researchers have developed criteria for characterizing certain types of wave breaking.

1.1. Breaking Wave Classification

The current terminology used to describe the types of breaking waves dates back to World War II, when surf zone conditions were characterized for amphibious landings [19][25]. The waves were defined as either plunging, spilling or surging. Since then a fourth category, collapsing breakers, has also been identified [40]. Deep water waves only include the spilling and plunging types of breaking. Being the most dramatic, plunging waves feature the formation of a jet at the crest that projects out from the front face and impacts the free surface with a splash at or below the mean water level. As the front face of the wave overturns, air is entrained and a two-phase turbulent flow ensues. In the more gentle case, spilling breaking waves begin with a small rough zone or bulge forming on the forward tip of the crest. Depending upon the scale, this bulge can include bubbles and droplets or, for smaller scales, a smooth bulge with a train of capillary waves developing beneath it. The turbulent bulge grows by spreading downslope and engulfing the face of the wave. Further discussion of crest geometry and scale can be found in Chapter 3.

Surging and collapsing waves occur at the shoreline and are closely related. Reflections are significant in these shallow water events. In surging breaking, there is no significant disturbance in the wave profile except at the moving shoreline. The collapsing wave combines characteristics of both surging and plunging breakers, whereby a plunging jet forms on the lower portion of the face of an otherwise surging wave. Neither collapsing nor surging waves were examined in this study.

In addition to their breaking shape and kinematics, breaking waves are classified by their temporal evolution as steady, unsteady, or quasi-steady. Unsteady breaking waves are the most commonly occurring class of breakers in the open ocean and near the shoreline. The breaking event is brief, typically ending within a wave period, though turbulence may still be present in the flow. Once the excess energy that led to the breaking event has dissipated, the breaking expires. The attributes which expire in the unsteady case are sustained over time in steady breaking. Steady flow over fixed objects or flow over objects in tow can result in steady wave breaking, and the breaking continues to dissipate energy as long as the input energy source is maintained. Quasi-steady waves always take the form of a spilling breaker. However, the turbulent bulge near the crest does not propagate down the front face of the wave as it does in the unsteady spilling breaker. The wave off a ship in transit is characterized as quasi-steady, though it often has a plunging component.

While all physical breaking waves have three spatial dimensions, most experimental and numerical investigations have focused on two-dimensional waves. The two-dimensional simplification is acceptable up to point when the flow ceases to be laminar. Turbulence implies that the flow has three significant dimensions, and as such, dissipation and other arguments based on 2D turbulent structures are an oversimplification which is subject to considerable error. However, the high degree of complexity requires that such simplifications be made in order establish the foundation of knowledge for future research.

1.2. Overview of Breaking Wave Study

The investigation of breaking waves has traditionally been divided into three unique approaches: field measurements of full-scale waves, experimental measurements of breaking waves generated in a controlled tank, and numerical simulation of breaking waves by approximating the governing equations. An argument could be made for a fourth method being the pure analytical investigation of the equations as performed by early hydrodynamicists such as Stokes. However, this work seems to have been completely replaced by numerical simulations through use of a computer, as the non-linear equations prevented further analytical solutions. Each approach has rendered valuable information regarding the breaking event.

The observation of breaking waves in the field is important for understanding the true dynamics of full-scale waves. Unfortunately, the wave fields in the open ocean tend to be strongly non-linear as well as being vast and having many scales of interest. Typical studies involve the use of acoustical and microwave remote sensing as well as point information from buoys. Field measurements of breaking waves are beyond the scope of this thesis, and the reader is referred to [37] for further information on the techniques.

Controlled laboratory studies have proven to be valuable in measuring the kinematics and dynamics of wave breaking. Typical unsteady wave experiments are performed in long, open-air tanks, with a wave generator at one end and an energy absorbing beach at the other. The wavemaker creates waves which are relatively constant in the crosstank direction, i.e. 2D plane waves, and they break at some distance along the tank. The breaking event is usually measured with video, point wave gauges, advanced fluid measurement techniques such as Particle Image Velocimetry (PIV), or some combination of these methods.

Numerical simulations, in parallel with experimental studies, have served to augment the understanding of breaking waves by carefully solving equations which govern the fluid dynamics. Because the entire flow is well-defined, numerical results can effectively provide full field and local process information at a higher resolution than with experiments. However, solving for this complex wave breaking phenomenon requires the use of approximations and assumptions that can limit the scale and physical accuracy of the simulations. Physical experiments are thus needed to verify the numerical results. Further discussion of experimental breaking wave generation and numerical simulations can be found in Chapter 4.

1.3. Dimensionless Parameters

Breaking waves occur over many scales in nature, from microbreakers, with wavelengths less than 30cm, through massive waves greater than 100m in wavelength. The waves in this study fall in the range of microbreakers and are smaller than those examined in most other experimental research. As will be discussed further in chapter 3, surface tension becomes an important factor affecting breaking waves with wavelengths less than 2m. To resolve issues of scale and generalize the results according the significant quantities, Hendrickson uses the Reynolds number and Weber number to characterize her results. The same scaling factors are used in this study and they are defined as

$$\text{Reynolds number:} \quad Re = \frac{\rho U \lambda}{\mu} \tag{1.11}$$

where ρ, μ are the fluid density and viscosity, respectively, and U, λ are the phase speed and wavelength of the associated wave. The other relevant scaling factor is

$$\text{Weber number:} \quad We = \frac{\rho U^2 \lambda}{\sigma} \tag{1.2}$$

where the only new variable, σ, is the value of surface tension at the fluid surface. Justifying the scalability of micro to macroscale waves is beyond the scope of this thesis, but these factors should contain most of the relevant parameters.

The values of phase speed, wavelength, and surface tension were determined directly through experiments or indirectly and the methods will be discussed in the chapters that follow. Since the fluid used was a 10% mixture of isopropyl alcohol and distilled water, the values of density and viscosity had to be derived. Viscosity was calculated using the empirical relation from [26]:

$$\log\eta = x_1 \log\eta_1 + x_2 \log\eta_2 \tag{1.3}$$

Where $\eta_{1,2}$ are the viscosities of the two pure components (IPA and water), and $x_{1,2}$ are their mole fractions. The density for the solution of 10% alcohol by volume was calculated as:

$$\rho = 0.1\rho_{IPA} + 0.9\rho_{water} \tag{1.4}$$

1.4. Scope of Thesis

The objective of this thesis is to experimentally investigate the flow fields around two-dimensional plunging and spilling breaking waves on a small scale. Part of the motivation for this work is derived from the recent numerical simulations performed in [25]. In these simulations, described section 4.2, Hendrickson uses a level set technique to create spilling through plunging waves and also captures the flow of the air above the water. The scale of these waves ranges from millimeters to a few centimeters in wavelength. Most current experimental results describe breaking waves on the order of 1m in wavelength. The goal of this work is to create and study waves which fall between Hendrickson's and those in current experimental studies and also to capture the air-water flow fields through the use of PIV. Keeping in mind the differences in scale, the experimental results will be compared to Hendrickson's simulations.

This thesis is organized as follows. *Chapter 2* describes the experimental facility and techniques for measuring breaking waves. The development of the hinged-paddle wavemaker and energy absorbing beach is discussed. The measurement instruments including resistance-type wave gauges, Wilhelmy plate, high-speed video, and PIV are presented along with the data acquisition system which allowed for integration of the different signals and measurements.

The influence of surface tension on small-scale waves is covered in *Chapter 3*. The fundamental properties of the surface free energy and methods of measurement are discussed first. The relevance of surface tension to breaking waves is presented, making note of previous experimental and numerical findings. Early results from adding isopropyl alcohol to the water displayed the importance of surface tension on the waves in this study. The experimental results characterizing the effects of isopropyl alcohol over various operating conditions are plotted to display control over surface tension during the subsequent wave breaking experiments.

Chapter 4 begins with an overview of the experimental and numerical methods of generating breaking waves. The shoal section used to induce breaking in these experiments is described, in addition to basic details of Hendrickson's simulations. This chapter also contains tables with relevant information for all of the breaking waves studied, referred to as the breaking wave database. Wave gauge data and screenshots from each experimental run are also included.

The results from PIV are presented in *Chapter 5*, and the velocity and vorticity maps from a plunging and spilling breaker are displayed. The flow field results agree with previous theory, but are primarily qualitative. A MATLAB edge detection algorithm was also implemented to capture the surface deformation during the breaking event. The combined air-water flow fields were analyzed by seeding both the air and water. The processed PIV data is presented and compared with results from Hendrickson's simulations.

Finally, *Chapter 6* summarizes the significant results of this investigation within the context of wave breaking research. Suggestions are made for improvements and future research.

Chapter 2

The Experimental Facility

The wave tank facility and methods used for flow and wave measurements are described in this section. A schematic of the wave tank is shown in figure 2-1. Waves propagate down the tank from the wave paddle and break as they travel up a fixed slope. Wave probes are mounted along the tank to measure the surface elevation and a beach is placed at the far end of the tank to minimize reflections. Surface tension measurements, high speed video analysis and Particle Image Velocimetry (PIV) methods are also presented in this chapter.

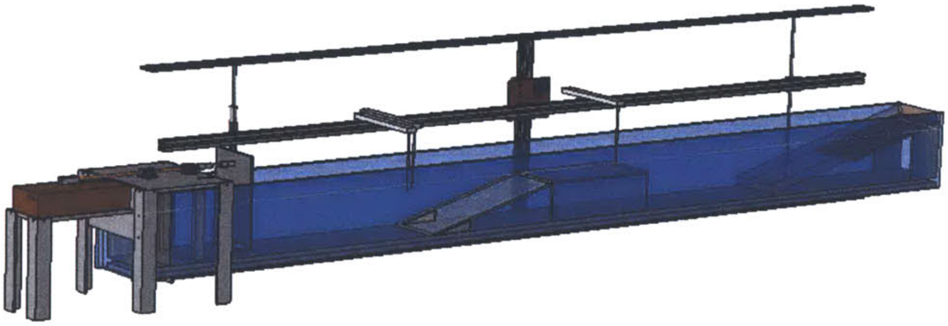

Figure 2-1: SolidWorks view of the tank, wavemaker, and wave gauge mounting rack. The energy absorbing beach and shoal section are also shown.

2.1 The Wave Tank

The experiments described in this thesis were performed in an existing acrylic wave tank with inner dimensions of 2.5 m in length, 16cm wide and 18 cm high. A piston-driven wave paddle creates precise, small-scale waves at one end of the tank, while an energy absorbing beach mitigates reflections at the opposite end. The wavemaker is driven by a servo-controlled, moving coil, SMAC linear actuator (model # LAS55-50-53-5) which has an encoder resolution of 5 micron, a 5 cm stroke length, and a maximum load capacity of 2.5lbs. A PC and external motion controller provide closed loop control for the wavemaker during actuation. The control system includes a Galil motion controller (DMC-1425) and interconnect module (ICM-1460), as well as a PWM servo amplifier (12A8) and power supply (PS2X300W) manufactured by Advanced Motion Controls. Motion profiles were programmed using the Galil control language and uploaded to controller memory to be called during testing.

In order to generate waves, the linear actuator is attached to a paddle at the upstream end of the wave channel. Motion of the connecting stainless steel shaft is constrained by linear bearings, ensuring actuation in the x-dimension only. Two types of polycarbonate wave paddles were studied: a piston-like, horizontally oscillating plate, and a bottom-hinged, pivoting paddle. The hinged-paddle created fewer transverse waves over a larger range of frequencies and amplitudes than the rigid plate. Also, since the velocity profile of deep water Airy waves decays exponentially with depth, the hinged paddle motion imposes a more accurate boundary condition. Thus, it was chosen to be used in the experimental research.

Another improvement to the existing system was the creation of an energy absorbing beach at the far end of the tank. The beach was designed to absorb maximum wave energy with materials that would not corrode in water. The new beach consisted of a perforated polypropylene plate mounted on angle brackets which could set the angle from 0-45 degrees. Reticulated, polyurethane foam (2.54 cm thick) covered the beach slope and far walls. A study of beach angle versus reflected wave amplitude revealed the best angle for wave attenuation. Wave probes measuring the free surface displacement in time captured the change in amplitude of the reflected wave packet. The beach was most effective at a 15 degree slope angle, where it dissipated the waves with reflections of less than 5.6% of the incident amplitude or 0.3% of incident energy, assuming energy is proportional to the square of the amplitude. In the following wave breaking experiments, measurements were completed on the first few waves of the incident packet, before the most energetic wave frequencies could be reflected back to the measurement window. This further reduces the influence of far wall reflections.

Dimensional drawings of the wave tank along with the mounting rack and wave probe locations are shown in figure 2-2.

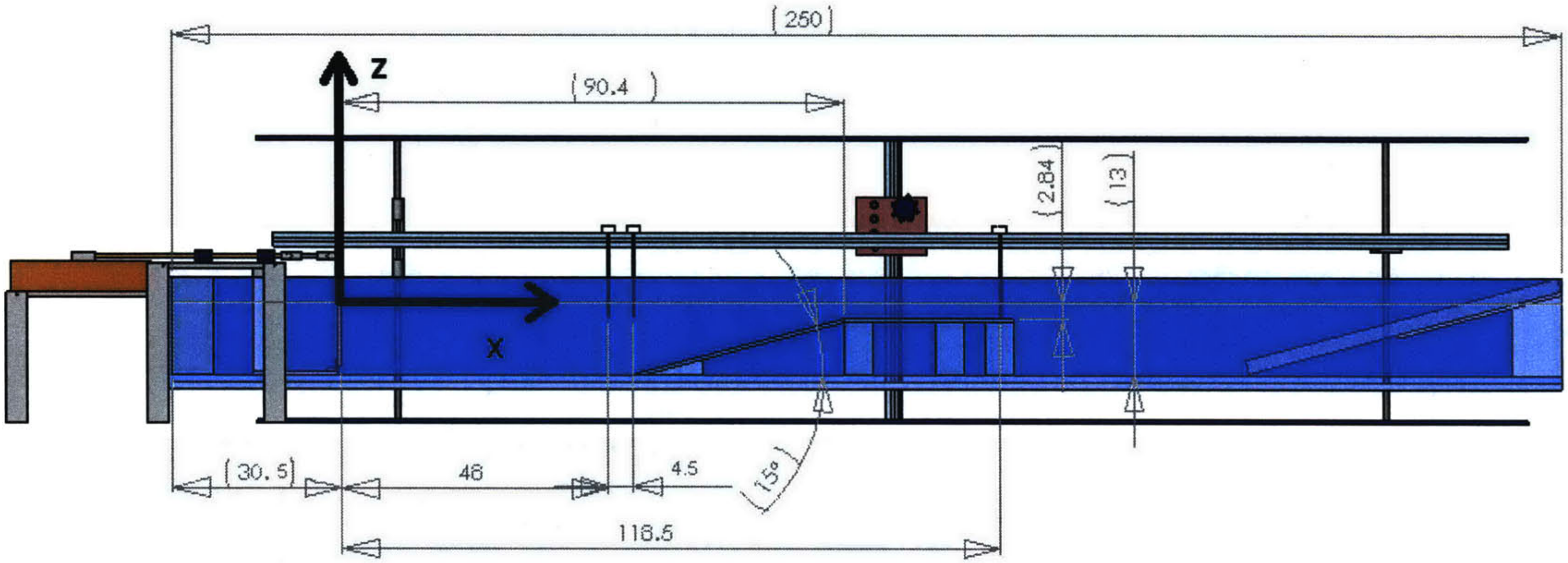

Figure 2-2: Dimensional profile of the wave tank generated in SolidWorks. The origin is centered at the intersection of the free surface and the mean wave paddle position. The wave probe and shoal locations are also featured, and the dimensions are in cm.

2.2 Wave Gauges

The free surface displacement in time was measured using a set of three resistance-type, surface piercing wave gauges designed for freshwater. Constructed and characterized in lab, the probes are primarily based off a design for freshwater wave gauges described by Chen [11]. The probes work by measuring the electrical resistance between two wire probes, which is inversely proportional to depth of submergence of the wires. Since water is a much more conductive medium than air, increasing the submergence will decrease the resistance between the two wires. If the wires are mounted at a fixed depth, passing waves result in a quantifiable change in resistance over time. A simple calibration function is then used to calculate the surface height profile in time. Figure 2-3 illustrates the electrical resistance for the probes.

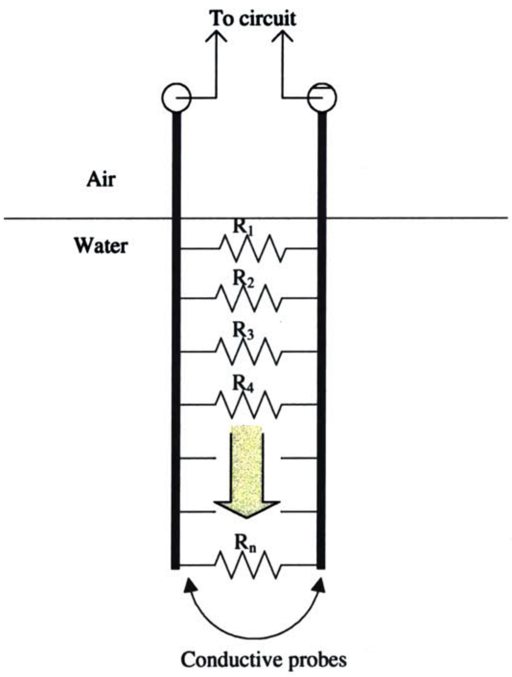

Figure 2-3: Model illustrating the resistance measured by the wave probe.

The sunken portion of the probes is analogous to a chain of resistors in parallel, and the number of resistors is proportional to the depth of submergence. As the water level and number of resistors increase, the overall resistance will decrease.

Three probes were constructed for use in the experiments. Each probe was made from two parallel, 1.58 mm diameter stainless steel rods which were 20 cm long. These wires had a diameter much smaller than the wavelength of the studied waves to minimize diffraction, but were sufficiently stiff to ensure rigidity over the length. For the small wavelength transverse waves and capillary waves, probe interactions become significant. Thus, these wave probes cannot be used to analyze these phenomena. To maintain the design separation distance of 6.35 mm, the wires were press-fitted into a rectangular block of Delrin on one end and a small, thin polycarbonate plate on the submerged end. On the air side, shielded coaxial cables connected the wire tips to gauge circuit. Electrical noise and interference from the wave paddle motor required that the circuit be housed in a grounded aluminum box. The wave gauges were mounted to an extruded aluminum bar on a frame behind the wave tank, as shown in figure 2-4. A rack and pinion system allowed for accurate vertical positioning of the bar during calibration. The probes could be fixed anywhere along the length of the wave tank during testing, but typically two probes were placed upstream of the breaking region and one downstream. A schematic of the wave probe amplifier is illustrated in figure 2-4.

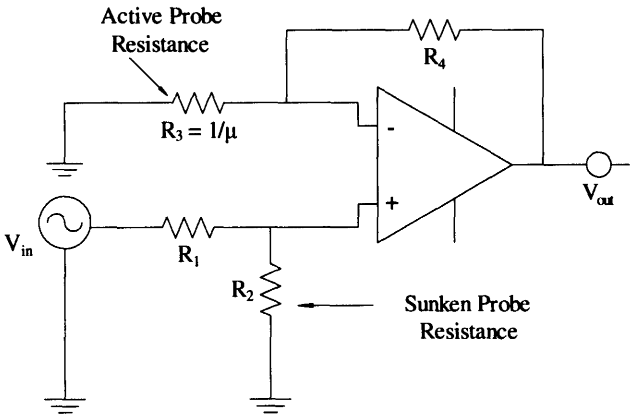

Figure 2-4: Diagram of the amplifier design for the wave gauges. The resistance of R_3 depends on the depth of wire submergence, while the sunken probe resistance, R_2, varies with the conductivity of the bulk fluid.

Each wave gauge features an additional sunken probe, which compensates for changes in water conductivity and improves calibration repeatability over time. The output voltage of the circuit is

$$V_{out} = V_{in} \times \left(\frac{R_2}{R_1 + R_2} \right) \times [1 + \mu R_4] \tag{2.1}$$

where μ is the probe conductance. For large R1 and R2, this equation becomes

$$V_{out} \approx V_{in} \times \left(\frac{R_2 R_4}{R_1} \right) \times \mu \tag{2.2}$$

Only one sunken probe was used during the course of this study. It was positioned at the far end of the tank under the energy absorbing beach. Because the sunken probes require shielded wires to pass through the free surface and potentially disrupt the flow, they were not positioned near the upstream probes. It is important to note that the excitation voltage is a constant amplitude AC signal, since electrolysis would occur at the probes if a DC current was used, and the resulting gas bubbles would ruin the measurement. The gauge circuit included a RMS-to-DC converter, high pass and low pass filters, a gain adjust Op-amp, and several other components.

The custom wave gauges built for this study worked fairly well, but problems with drift and a small signal made repeatable measurements in time difficult to obtain. The probes worked best in tap water, with a signal difference of about 2 volts over 7cm. However, the use of distilled water and IPA, both with lower conductance values, brought the range down to .5 volt over 7cm. Independent calibrations curves were quite linear with maximum deviations of around .5 mm over a length of 5 cm. However, the slope of the calibration curve changed appreciably in time, even with sunken probes placed near the actives. Over the course of a few hours, the measured probe error was around 10-13%. This large error should be considered when interpreting the experimental results that follow.

2.3 Surface Tension Measurements

Surface tension at the air-water interface was an important factor effecting small-scale wave breaking in these experiments. In order to reduce the surface tension, isopropyl alcohol and water were mixed and the ratio was varied to observe changes in wave breaking dynamics. Therefore it was necessary to quantify surface tension changes as a function of the mixture ratio. There are several different methods for measuring the value of surface tension that are commonly used, such as the DuNoüy ring technique and drop analysis methods. In this study, the Wilhelmy plate technique was used in this study. Details of surface tension measurements and the technique are discussed in Chapter 3.

2.4 Hi-Speed Imaging

High speed video was used to record both qualitative and quantitative information as wave progressed through the breaking event. Under normal lighting conditions, information such as breaker type and shape in time was captured. Halogen floodlights were used to illuminate the wave tank while the X Stream Vision XS-3 camera (maximum frame rate of 628 frames/sec at 1K x 1K resolution, from IDT, Inc.) recorded the break. The images were recorded at 500 fps and saved as TIFF files for post-processing. High Speed Particle Image Velocimetry (PIV) was used for quantitative measurements. A IR laser sheet illuminated the location of interest, which was seed with neutrally buoyant silver coated hollow glass spheres with 14 μm diameter. The particles were added near the point of measurement and mixed until optimum seeding was achieved. To capture the flow field on the air-side of the interface, a water-based fog was injected into the tank before test runs and allowed to fill the volume. The low-cost Lasiris Magnum near-IR TTL diode line generator laser operated under continuous illumination. Further information on the theory of PIV and its implementation in this study can be found in Chapter 5.

2.5 Data Acquisition

A National Instruments PC-based data acquisition system, with a LabView 7.0 interface, was used to coordinate motion commands and record data. The hardware consisted of a PCI-6221 data acquisition board installed in a PC. The board has 24 digital I/O lines, two 16-bit analog outputs, as well as 32-bit counters and digital triggering capability. The wave gauges and the camera trigger attached to a shielded BNC connector block (BNX-2110) which relayed signals to the acquisition board. A schematic of the experimental set-up and data pathways is illustrated in figure 2-5. A LabView virtual instrument interface was built to send commands to the motor controller, trigger the camera, and record wave gauge data. The wave gauge sampling rate was 100Hz and probe data was typically captured for 10 seconds. The high-speed camera used to capture breaking waves recorded images for six seconds at 500 fps. Wave train specifications such as frequency, amplitude, and number of waves were inputs in the VI before an experiment run. For each run, the motor and wave probe data acquisition started simultaneously and the camera was triggered to begin recording after a 1 second delay. Probe data was stored in the LabView Measurement File (*.lvm) format and could be loaded into MATLAB for post-processing.

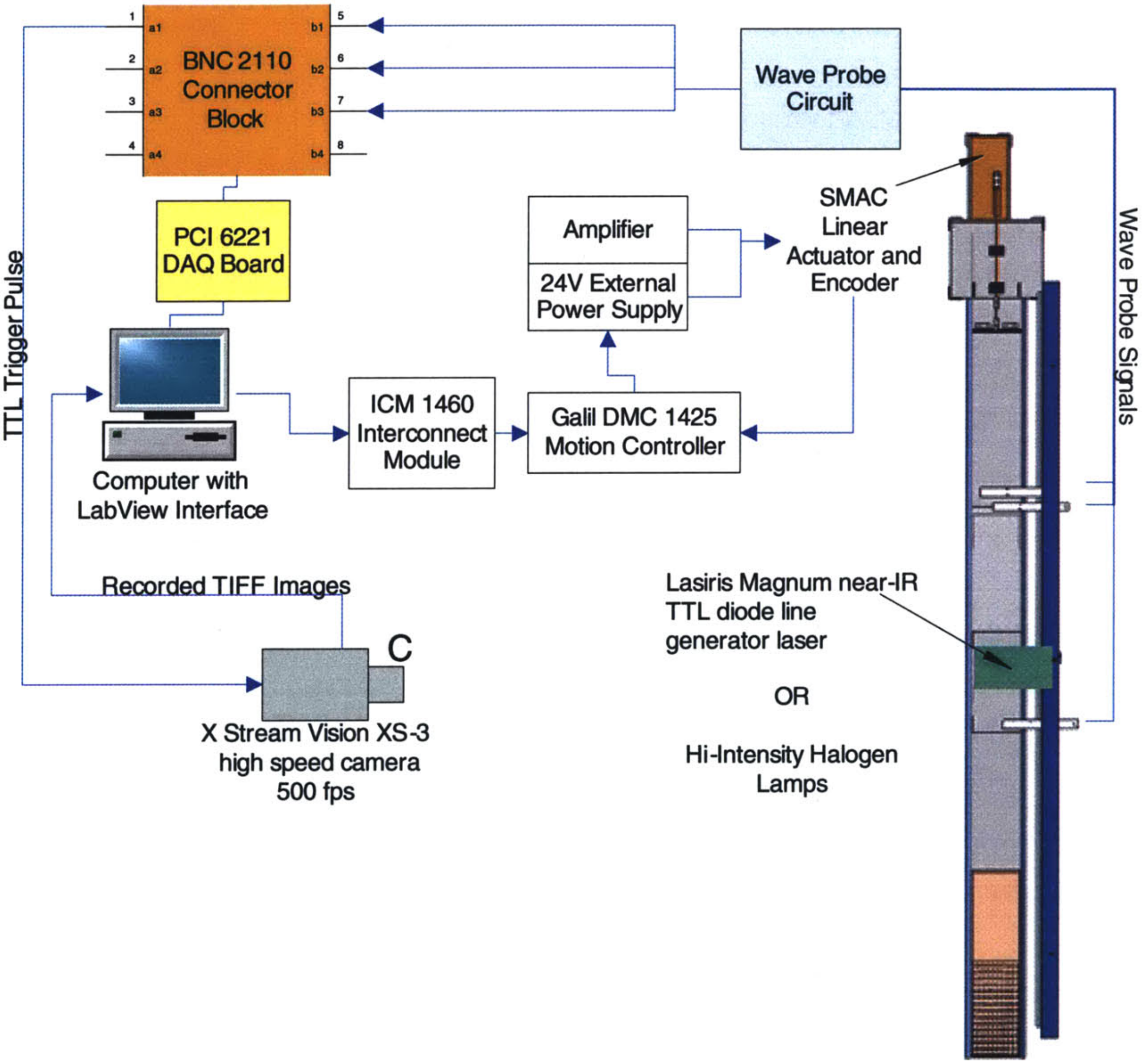

Figure 2-6: Schematic of the instrumentation and data pathways. A top-down view of the wave tank is illustrated at right.

Chapter 3

Surface Tension

The dynamics of fluids near an air-water interface are influenced by the surface free energy, or surface tension. The relative magnitude of this energy indicates how it will affect the physics at small scales. Since the thrust of this research has been on examining the wave breaking event in a small tank, the effects of surface tension have been explored thoroughly. The importance of surface tension in wave breaking has been noted in the literature, but its effect on waves of the scale studied in this research has not been rigorously addressed. This chapter details the fundamental attributes of surface tension and the characterization of it within the context of this wave breaking research.

3.1 Properties of Surface Tension

The effects of surface tension are widely recognized and unavoidable in daily life. The distinctive shapes of raindrops and tears illustrate the fundamental property that liquid surfaces tend to contract to the smallest possible area for a given volume. In the absence of external forces, such droplets would assume a purely spherical shape [1] [35]. The spontaneous contraction of the surface suggests that there is a free energy associated with it [1]. This free energy is a direct result of the net intermolecular forces of attraction in a fluid medium. In the interior of the liquid bulk, molecules are surrounded by neighbors on all sides, each neighbor exerting an attractive force on each other. On average these forces are uniform in all directions within the bulk. As illustrated in figure 3-1, molecules on the surface of a gas-liquid interface are only partially surrounded by neighbors. The distance between molecules in the gas is so large relative to those in the liquid that the attractive forces they exert on the surface can be ignored [44]. If the gas phase was replaced with another immiscible fluid, the interfacial free energy would likely be reduced, due to additional net intermolecular force across the interface. Interfacial waves across two immiscible fluids are beyond the scope of this research, and thus the discussion will be limited to surface tension across a gas-liquid interface.

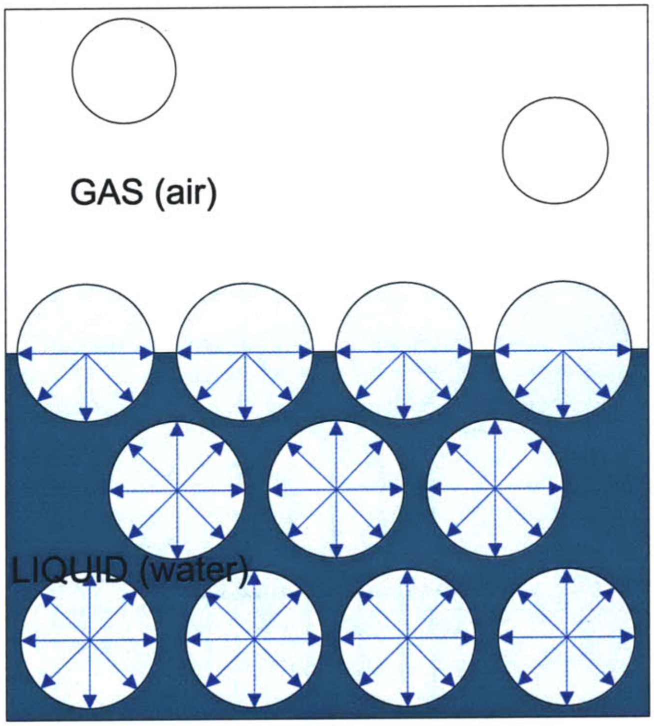

Figure 3-1: Schematic of the intermolecular forces on neighboring liquid molecules. The unbalanced force on free surface molecules results in a surface free energy or surface tension.

In order to deform the free surface from its contracted state, work must be must be done by moving bulk molecules to the interface against the inward force of attraction. To simplify the calculations of this work, a hypothetical tension acting parallel to the surface is substituted for the free energy. This tension is a mathematical simplification that has the same units and numerical magnitude as the surface energy per unit area. It is worth noting that molecules throughout a liquid are dynamic and the hypothetical tension does not imply the existence of a contractile skin or membrane surrounding the bulk. When the surface is displaced into a curved configuration, work is done to increase the area. This increase in area is supplied by the work of a pressure difference across the interface. Young and Laplace account for this in the fundamental equation of Capillarity:

$$\Delta p = \sigma\left(\frac{1}{R_1}+\frac{1}{R_2}\right) \tag{3.1}$$

where R_1 and R_2 are the principle radii of curvature [1]. As apparent in the formula, this pressure difference will not exist for surfaces lacking curvature. This equation is the foundation of most methods for experimentally measuring surface tension.

The discussion of surface tension thus far describes an ideal interface of separating pure fluid from a pure gas. In reality, surface tension is a sensitive quantity that can be easily affected. For example, when a fluid reaches critical temperature, surface tension vanishes completely and the particles move to the gaseous state. Temperature changes, fluid surfactants or solid particulates on the surface, an inhomogeneous bulk, etc. all can significantly change the measured surface tension. These factors were considered and characterized experimentally in this study.

3.2 Surface Tension Measurement

There are many different methods for determining the surface tension of a fluid surface, categorized as either static or dynamic methods. Static methods are used on surfaces which have been stationary for an appreciable amount of time. Dynamic methods capture the small changes in surface tension resulting from liquid vibrations. The vibrations cause periodic extensions and contraction of the surface [1]. These dynamic changes are too small to be significant to the breaking waves in this study. Hence, a static measurement technique was employed in this research.

One class of static surface tension measurement methods requires analyzing a drop of liquid. In the pendant drop method, the geometry of a liquid drop forming at the tip of a capillary tube is analyzed to determine the surface tension [28]. This method is subject to error of the eye of the operator or it requires costly equipment and analysis software. The drop-volume and drop-weight techniques both are based upon the amount of fluid in a drop which detaches from a capillary tube. The radius of the tube, volume or weight of the detached drop, and a correction factor are used to calculate a value for the surface tension. These methods require precise control over rate of drop formation and tube geometry, as well as accurate correction factors presented in [34]. The spinning drop method is best suited for characterizing very low surface tensions [28]. A drop of liquid is injected into a tube of a different, higher density, immiscible fluid. The tube is spun at a fixed rate and the centrifugal forces cause elongation of the drop. Analysis of the elongated shape provides a value of the surface tension.

Dating back to the early 1900's, the DuNoüy ring method is widely used [34]. A platinum-iridium ring of precise dimension (usually around 2cm diameter) is slowly retracted from within a fluid. The wetted ring pulls a small liquid volume, which depends upon fluid density and surface tension, above the free surface. A sensitive scale measures the force on the ring as it is pulled from the fluid. The surface tension is related to the maximum force required to detach the ring from the fluid minus the weight of the ring. A correction factor must also be used to account for the volume of fluid above the free surface, and the result is then divided by the perimeter of the ring to give correct units of surface tension. With a precise correction factor, ring tensiometry can provide an excellent measurement of the static surface tension [34].

Another technique is the Wilhelmy plate method, which is a similar detachment technique commonly used to measure surface tension. An advantage of the plate over the ring method is that there is no need for correction factors, and thus the density of the fluid does not have to be known. The Wilhelmy plate method was used in this study because of its accuracy and the availability of a system in the department.

In the Wilhelmy plate technique, a roughened, thin platinum plate suspended from a scale is slowly lowered towards the fluid surface. At the instant the fluid touches the plate, an additional force is detected. Assuming perfect wetting of the plate, the contact angle will be zero, and the force will be related to surface tension by

$$F = \sigma P \approx 2\sigma L \tag{3.2}$$

In the expression above, F is the additional force measured at time of contact, and P is the plate perimeter, which can be approximate as twice the length, L, for thin plates. To ensure proper wetting, the plate is roughened and cleaned of contaminants before each measurement with a torch flame. An illustration of the technique appears in figure 3-2.

It should be noted that contaminants such as airborne particles can affect the surface tension of the test fluid or the wetting ability of the platinum plate. Care was taken to ensure that the results from the surface tension tests accurately reflected the true surface tension. Powder-free chloroprene gloves were used to prevent oils from

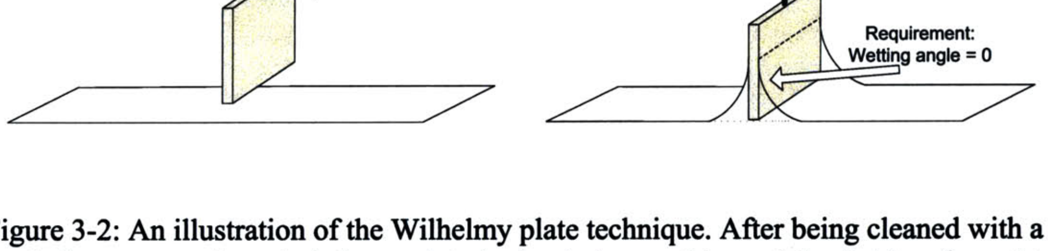

Figure 3-2: An illustration of the Wilhelmy plate technique. After being cleaned with a torch flame, a roughened platinum plate is slowly lowered toward the fluid surface. At the point of contact, the measured change in force divided by the perimeter is the surface tension.

contaminating the test vessels or water in the wave tank, and all test beakers used to measure surface tension were cleaned with a flame before testing.

3.3 Surface Tension and Breaking Waves

Quantifying surface tension through experiments was critical in this research because the surface free energy can dramatically effect wave deformation during breaking. Results from both numerical models and experiments have shown that, at certain scales, surface tension affects the crest of a wave and can alter the breaking process appreciably.

Duncan describes the effects of surface tension in his review of spilling breakers [19]. Waves of long wavelength are unaffected by surface tension while short wavelength waves are dominated by its effects. Mathematically, surface tension enters the equations of motion via the dynamic free surface boundary condition. The condition includes a pressure jump term equivalent to (3.1) in two-dimensions. For a given wave shape, the radius of curvature at the crest decreases with wavelength. The reduction in curvature causes an increase in the pressure change across the free surface. The pressure jump limits the size of the radius, and, unless the value of surface tension is reduced, short wavelength waves cannot support the same jet formation found in breaking at larger scales.

At long wavelengths, a small jet is formed at the crest which impacts the free surface well above the mean water level in the spilling case. The impact entrains air and starts the spilling process by creating a bubbly, turbulent region which propagates or "spills" down the face of the wave. At short wavelengths, the effects of surface tension suppress the formation of the small jet. A ripple pattern forms on the forward face of the crest. This pattern is characterized by a bulge and toe formation, with a train of capillary waves created under the toe. The crest instability then begins to spill down the wave face, creating turbulent flow without the bubbles and droplets of the long wavelength case. Figure 3-3 depicts these two cases.

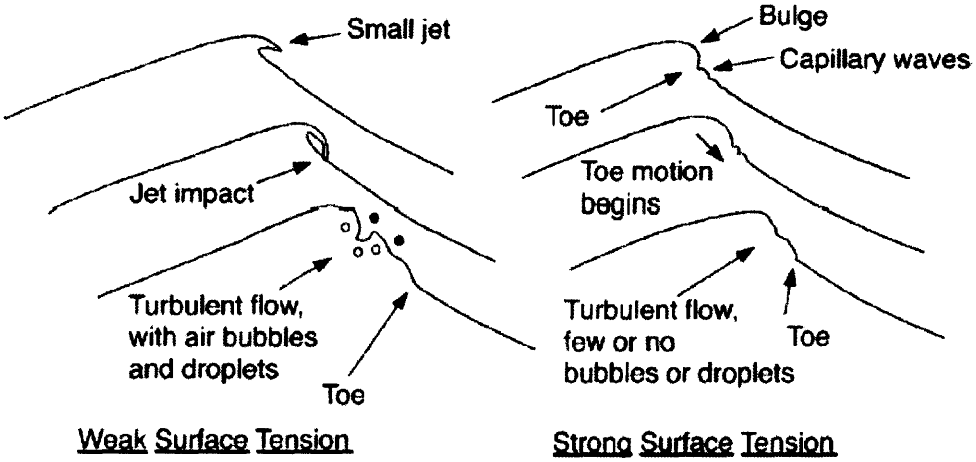

Figure 3-3: Schematic showing the influence of surface tension on spilling breaking waves. Reprinted from [19].

Several numerical studies have confirmed the importance of wavelength and surface tension in wave breaking. Duncan writes in his review that at zero surface tension, numerical techniques in two-dimensional time dependent domains predict the formation and impact of a small jet for all cases. Tulin [50] uses boundary element calculations to explore the effect of wavelength and surface tension at T=73 dyne/cm (distilled water). Presented in Figure 3-4, his results show that for wavelengths above 2m, the breaking begins with a small jet formation which is similar to the cases with zero surface tension. Below 2m, the jet becomes more rounded and is eventually replaced by a bulge and toe near 0.5m.

Computational limitations of Hendrickson's simulations required that the wavelengths be no greater than a few centimeters. Hendrickson overcomes the length restriction by using the Weber number to scale surface tension effects. With the same initial surface forcing, both a small plunging jet and a bulge formation are created by changing the Weber number.

Duncan and Liu [21] use an experimental technique to examine the effects of surfactants on spilling waves. Varying concentrations of the surfactant sodium dodecyl sulfate were added to a wave tank, and breaking waves generated using dispersive focusing were analyzed with hi-speed video. The four surfactant concentrations resulted

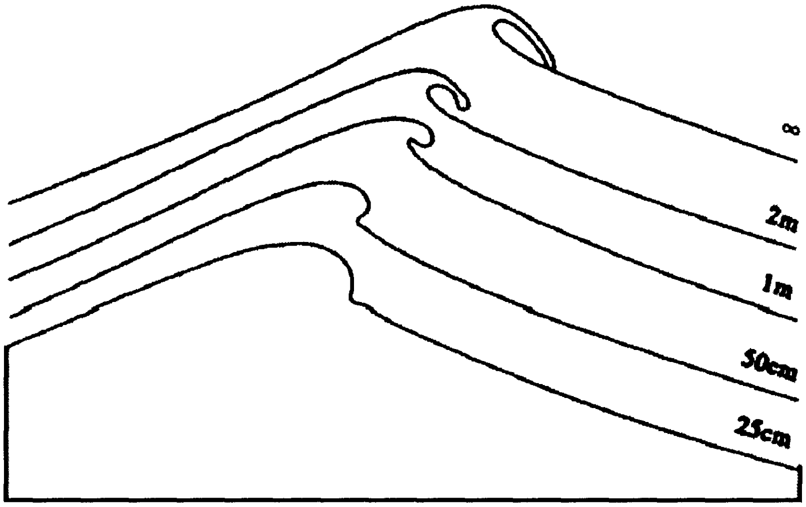

Figure 3-4: Numerical simulation results from [50] with a constant surface tension = 73 dynes/cm. The numbers on the right correspond to the wavelength of the central wave frequency for each case. Notice the small plunging jet is replaced by a bulge-toe formation as wavelengths get smaller.

in surface tension values spaced between 38 and 64 dyne/cm. The surfactant also changes viscosity and surface elasticity of the fluid. The average frequencies of focused waves were 1.15, 1.26, and 1.42 Hz. Their results show significant changes in the wave deformation and breaking. Without surfactant, the typical bulge-toe spilling breaker is created. As the surfactant concentration is increased, the size of the bulge and amplitude of capillary waves decrease. At the highest surfactant concentration, a small plunging jet ejects from the front face of the wave below the crest. Their measurements indicate that surface dynamic properties affect the behavior of the spilling breaker in a complex way.

3.4 Characterization of Surface Tension in this Study

The scales of interest to this study are within the region where the surface tension of pure water modifies wave deformation during breaking. With deep water wavelengths from 10-40cm, these waves are predicted by numerical techniques to form primarily bulge-toe structures at the onset of breaking [50]. Most experimental studies seek to avoid the influence of surface tension in the results by limiting the scale. Such experiments are performed in larger wave tanks (~30m x 1m x 1m) and typically do not include wavelengths shorter than 80cm [19] [21] [43] [4]. Perlin [41] uses wave focusing to generate a plunging breaker with an approximate wavelength of 70cm. This plunging breaker also features a significant bulge and capillary wave system on the underside of the jet. Ceniceros & Hou [8] use boundary element calculations in their simulation and find a similar structure at a wavelength 77cm.

Preliminary results from the breaking waves in this study did not feature the formation of a plunging jet for any case, as predicted by the literature. The initial experiments were performed with filtered tap water with an unknown surface tension, most likely near 74 dyne/cm. At a depth of 13cm before the shoaling section, waves were induced to break by propagation up a 15 degree slope to a level plateau. See Chapter 4 for further details on the generation of breaking waves. The bulge, toe and capillary wave system were apparent in all test runs, with a more pronounced bulge forming for the steepest waves of large amplitude. Since Hendrickson's simulations scaled surface tension effects to create gentle spilling through plunging breaking waves, an analogous experimental technique was employed to reduce the influence of surface tension on the waves in this study.

In an early attempt to create plunging breakers by reducing the surface tension of the fluid, Isopropyl Alcohol (IPA) was poured into the existing tap water. At a concentration of 3% IPA by volume, waves which had previously formed a large bulge and toe at the crest began to plunge. A frame grab from the early results is pictured in figure 3-5.

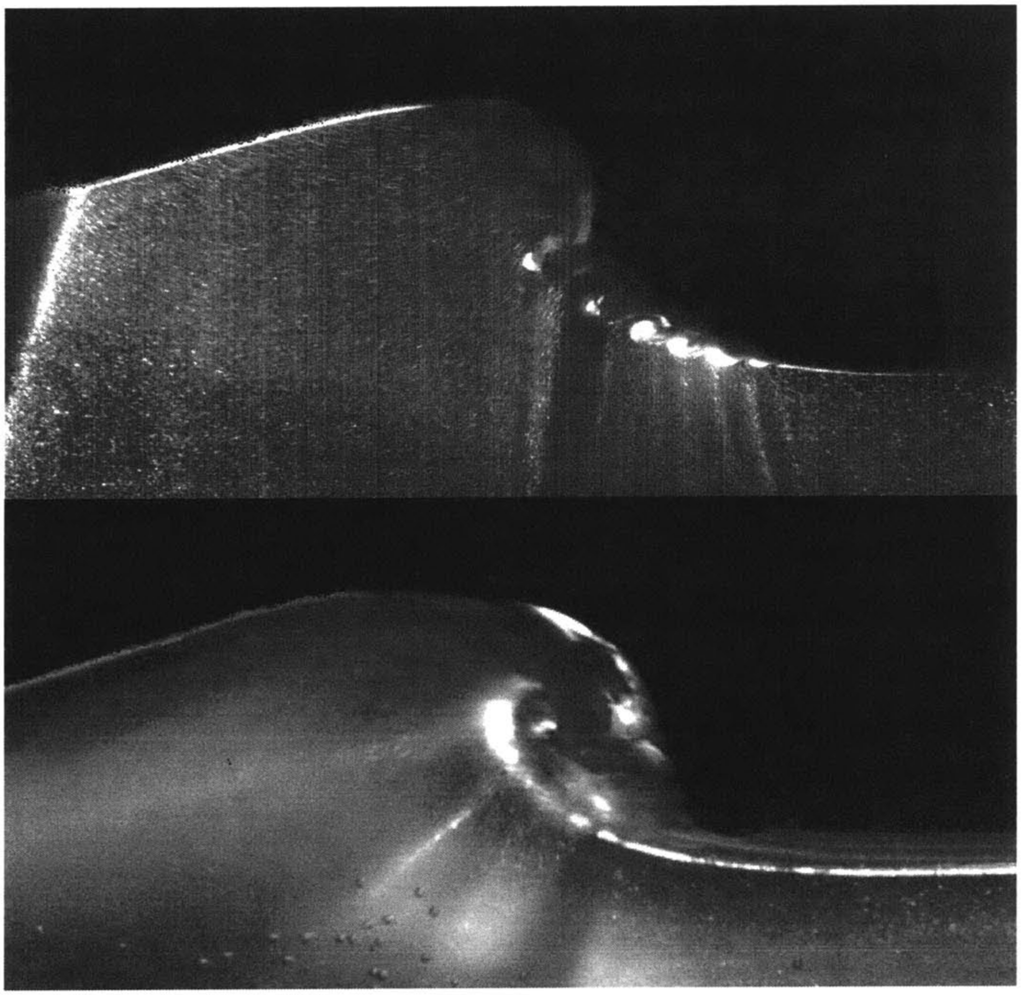

Figure 3-5: Effects of IPA on a 2Hz ($\lambda \approx 40$ cm) breaking wave with 2.25 cm input amplitude. (top) Distilled water with PIV particles. Notice the bulge-toe formation with shear layer vortices developing below. (bottom) Early image of a characteristic plunging breaker in a solution of 3% IPA by volume.

Isopropyl alcohol was added because of its low surface tension (22 dynes/cm) and complete miscibility in water at all concentrations. IPA also forms azeotropic mixtures with water, so there should be no change in the concentration due to evaporation of the mix. Varying concentrations of IPA and water have been used to control surface tension in the semiconductor industry for Marangoni wafer drying [29]. Further analysis of the final alcohol-tap water mix suggested that the assumption of complete miscibility may have been inadequate. Visual inspection of the water column revealed that the alcohol did not form a homogenous mix with the tap water. The fluid near the free surface appeared cloudy with horizontal striations, while it was much clearer at the bottom. With alcohol having a positively buoyant specific gravity of 0.79, it is reasonable to assume that most of the IPA remained near the surface after being poured, creating a stratified flow. Thus, although the mix was 3% IPA by volume, the surface tension may not reflect the same quantity as would be expected in a 3% mix. Since the composition of tap water can vary over time, distilled water was selected as replacement in future experiments.

To resolve the problems associated with the incomplete mixing and quantify the change in surface tension due to the IPA, a set of isolated experiments was performed. The Wilhelmy Plate method was used to measure the static surface tension in 100mL sample volumes of various IPA concentrations. Unfortunately *in-situ* measurements were not able to be performed. However, the results from the isolated tests provide useful insight into the surface tension changes versus IPA concentration, mixing, addition of PIV particles and fog particles. The fluid temperature remained constant in all tests at 23°C.

The first set of tests explored the importance of particulate contamination and IPA mixing on a concentration of 5% IPA. Three beakers were filled with 95% distilled water. One was initially stirred until the mix appeared homogenous and covered with a lid to prevent accumulation of airborne particulates. Alcohol was added to distilled water without stirring for the second and third cases, and one of the two was covered. The results from this test are shown in figure 3-6. The most dramatic change in surface tension, an increase of 4 dynes/cm, occurred in the non-stirred, open air case. The stirred, covered beaker remained at a relatively constant surface tension of around 52.5 dynes/cm. The surface tension is lower for both non-stirred cases, as expected if the IPA remains at a higher concentration near the surface. The results show that in order to maintain a relatively constant surface tension in time, the tank should be covered and the IPA should be well mixed before taking data.

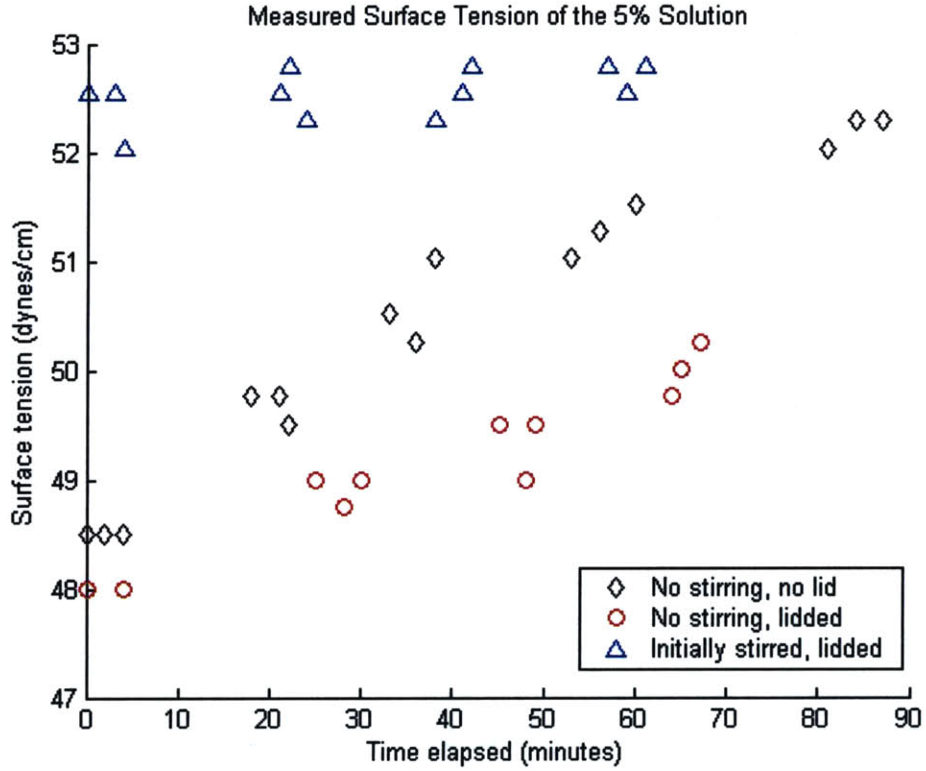

Figure 3-6: Wilhelmy plate results for the 5% IPA solution subject to 3 initial conditions. The surface tension for the mixed and lidded case remains fairly constant in time.

Tests were also performed on 10% and 20% concentrations of IPA, as well as on mixes in the presence of fog particles and PIV particles. Since plunging waves could be produced in the 3% non-mixed solution, well-mixed concentrations higher than 20% were not expected to be required for forming jets. A plot of the complete results is illustrated in figure 3-7. Neither the PIV particles nor the fog particles change the surface tension significantly. Both mixes remained relatively constant in time.

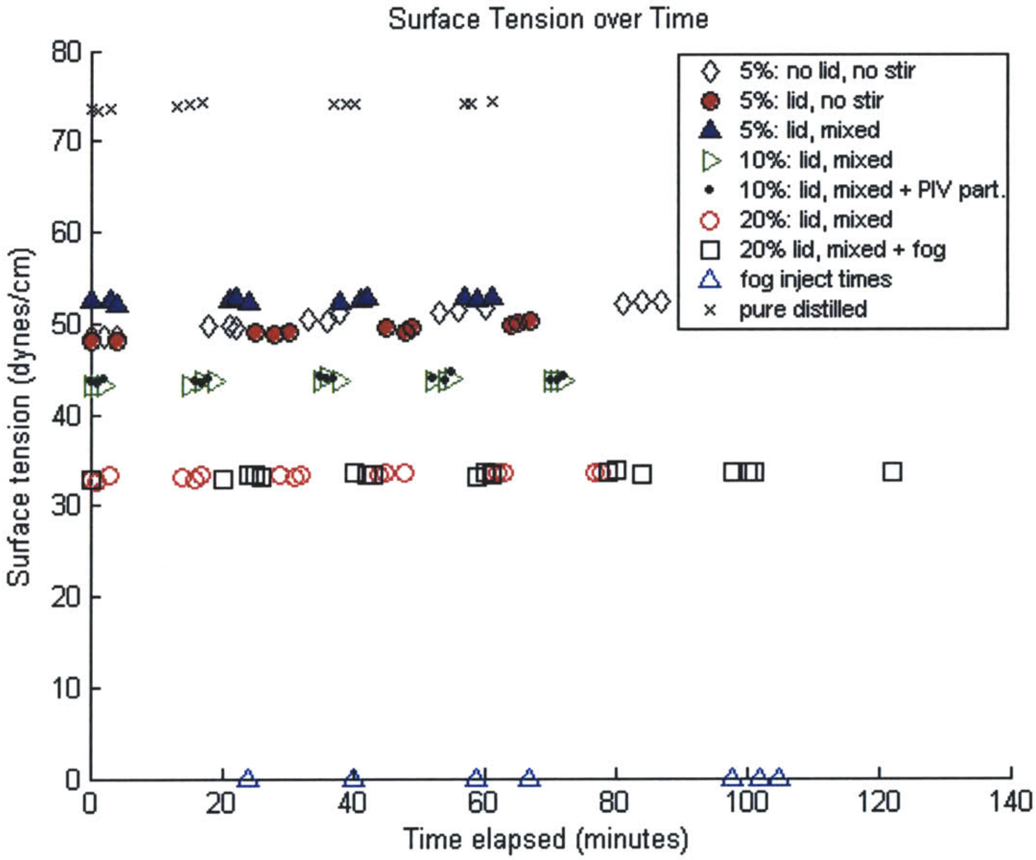

Figure 3-7: Surface tension measurement results for 3 different IPA concentrations over a total of 8 different cases.

As a control in the experiments, the surface tension of pure distilled water was also tested in time. Figure 3-7 shows that it stays relatively constant around 73.87, with a maximum value of 74.25. This result is slightly higher than the expected value of 73.0. This error (maximum 1.7%) can be attributed to an incorrect step in the Wilhelmy plate procedure. Rather than recording the additional force at first contact of the liquid surface, the results reflect the measurement of the maximum force before detachment minus the weight of the additional water droplets after detachment. This procedure was used across all test results and thus the actual surface tension may be slightly lower. Tests with distilled water and a 10% IPA solution were performed using the correct Wilhelmy plate procedure and the results are shown alongside the original measurements in figure 3-8.

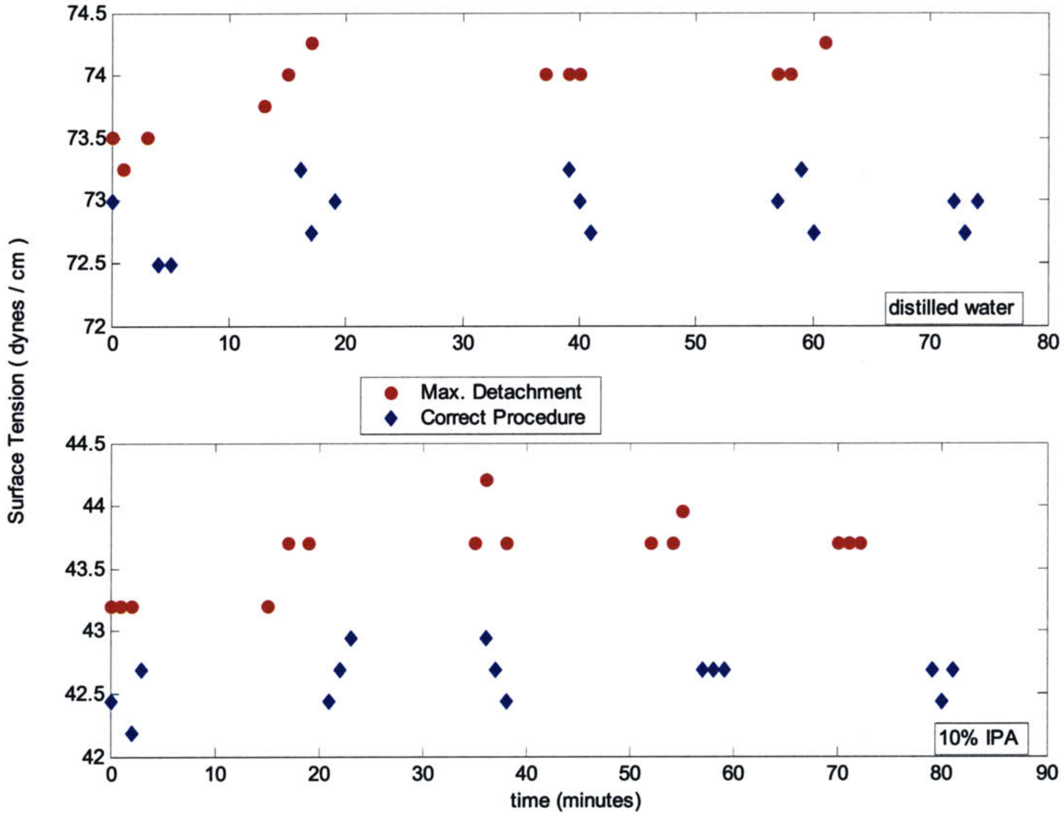

Figure 3-8: Comparison of measured surface tension using the maximum plate detachment force versus the correct procedure of using the force at initial free surface contact.

As expected, the measured surface tension using the corrected Wilhelmy plate procedure is slightly lower than in the maximum detachment results. In both the distilled case and 10% solution, there is approximately a 1 dyne/cm difference between the average measurements. This corresponds to a 1.3% error for distilled water and 2.3% error for the 10% IPA mix. Since the wave breaking experiments that follow were performed in a 10% IPA solution by volume, the corrected value was only measured for this mixture and the distilled control.

Notice in figure 3-7 that the relationship between percent composition of IPA and surface tension is not linear. The results of the average value of surface tension versus

IPA weight percentage are plotted alongside published results in figure 3-9. The measurements follow the published data well. Since the measured results were based upon solutions of IPA by percent volume, they had to be corrected in terms of percent weight for the plot.

The results from the Wilhelmy plate tests provide valuable information on the influence of isopropyl alcohol and distilled water on surface tension. While the precise value of surface tension during the wave breaking experiments remains unknown due to the lack of *in-situ* measurements, the sample volumes indicate the general operating point of a mixed IPA-distilled fluid. A 10% solution, 43.6 dynes/cm, was selected for wave testing, and early experiments showed that plunging waves did form in this mixture.

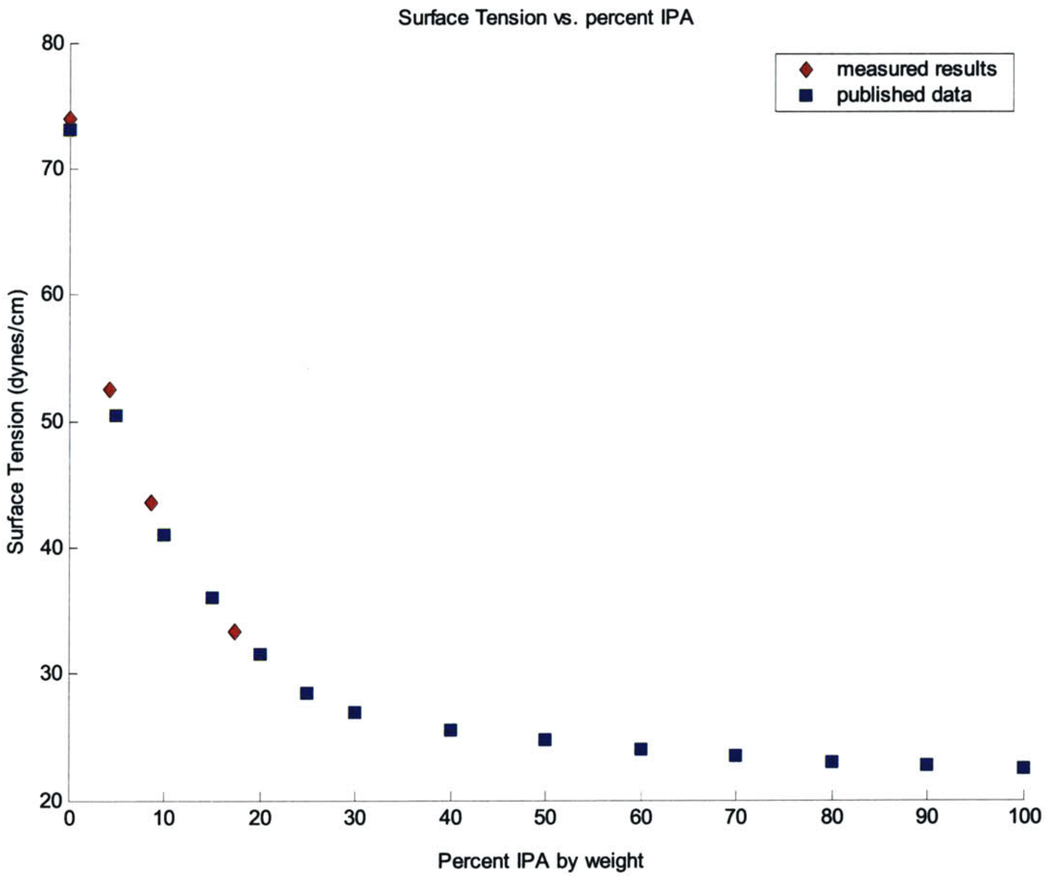

Figure 3-9: Plot of the change in surface tension versus the weight percentage of IPA in distilled water. The measured results are plotted alongside data published in [29].

Before filling the wave tank for testing, care was taken to ensure that the conditions of the tank reflected those of the isolated experiments. The inner walls were cleaned with pure IPA to remove contaminants. Unfortunately, torch cleaning was not possible, due to the acrylic walls. Gloves were worn to prevent hand oils from contaminating the fluid and affecting surface tension. The tank was also covered to contain the fog during PIV and to prevent airborne particulates from contaminating the surface. Additionally, a polycarbonate plate was used to skim the surface before testing. The generation of breaking waves and results from the 10% IPA solution are discussed next in Chapter 4.

Chapter 4

Breaking Waves

4.1 Experimental Breaking Wave Generation

This section reviews current research in the area of breaking waves. This work is separated into two categories: steady or unsteady deep water breaking waves and waves that break due to shoaling. Theories and nomenclature relevant to this thesis are also explored herein.

4.1.1 Steady Waves and Unsteady Deep Water Waves

Many techniques have been developed for generating breaking waves in a laboratory tank, and these methods have been used to create the full range of breaking wave types over various conditions. Steady and quasi-steady breakers have been experimentally produced by the flow across a submerged hydrofoil [5] [18]. Surface piercing ship hulls have also been used to create quasi-steady breakers, especially 3D breaking waves, due to the nature of the resulting wave shape [17][45]. Breaking is maintained by input of a steady source of energy proportional to the drag times the velocity of body [42]. Dabiri and Gharib [13] implemented a hydraulic jump by using a honeycomb screen section to create a pressure differential in a small channel. This produced a spilling breaking wave downstream of the screen.

Unsteady breaking waves have been realized by focusing wave energy in space. For deep water waves, researchers must limit the ratio of water depth to wavelength such that bottom effects are not significant. Converging channel walls have been used to induce wave growth past the limit breaking amplitude [52]. Advancing wave fronts from an impulsively started wavemaker have been shown to break if the amplitude overshoot of the Fresnel envelope is greater than the breaking limit [31].

While these techniques have effectively created breaking waves, wave focusing through the use of frequency dispersion has been a more widely practiced method of creating deep water breaking waves. Improvements to the fundamental principle have increased spatial and temporal repeatability. The dispersive focusing technique is believed to model a naturally occurring mechanism of unsteady breaking wave generation [42], whereby waves of different frequencies converge and break. Longuet-Higgins [31] describes a method of generation by linearly decreasing wavemaker frequency such that high and low frequency components meet at a defined distance down the tank to cause breaking. He uses linear theory to derive the following relationship between paddle frequency, ω, gravity, and the energy focal point, x_b:

$$\frac{d\omega}{dt} = \frac{-g}{2x_b} \tag{4.1}$$

The dispersion relation given by linear theory relates frequency, wavenumber, k, and water depth, h, and it is defined as:

$$\omega^2 = gk \tanh kh \tag{4.2}$$

The signal must be smoothly brought to zero at both ends of the pulse to reduce transient effects [42]. While this technique can produce gentle spilling through plunging breakers, x_b can only be defined to within a wavelength of the largest wave. To further tune the breaking location, the phase of the signal must be experimentally determined.

A similar focusing technique, involving of the summation of different frequency sinusoids, has been used by [43] as well as many other researchers since its introduction (sources). It has been reported to have spatial repeatability in the x-direction of +/- 0.02m over 7 meters of wave propagation and temporal repeatability to within 0.01s over 17s

[42]. The method requires generation of a quasi-periodic signal by summing 32 equal amplitude, evenly spaced frequency components over a band. The phase of each component at the paddle is determined such that the wave crests arrive simultaneously at a point downstream. A brief mathematical description is as follows:

The free surface displacement, η, is given by

$$\eta(x,t)=\sum_{n=1}^{N}a_n\cos(k_n x-\omega_n t-\varphi_n) \tag{4.3}$$

where a_n, k_n, ω_n, φ_n are the amplitude, wavenumber, frequency (radians), and phase of the nth component, respectively. N is the total number of sinusoids and has often been 32 to approximate a continuous spectrum and eliminate its dependence. The phase can be determined by setting the cosine term equal to 1 at the breaking time and location. The frequency spectrum is also simplified such that a_n is constant. Assuming a mean paddle position of zero, equation (4.3) can be further reduced to define the paddle displacement

$$\eta(0,t)=\sum_{n=1}^{N}a\cos\left(-k_n x_b-\omega_n(t-t_b)\right) \tag{4.4}$$

where x_b and t_b are the breaking location and time. Families of wave packets were calculated by varying three non-dimensional quantities which characterize the signal: $\Delta f/fc$, $x_b k_c$, and ak_c. $\Delta f/fc$ is the frequency band divided by central frequency, and k_c is the wavenumber corresponding to the central frequency, as determined by the dispersion relation. See [43] for further details on the derivation and method.

Other dispersive focusing techniques have been used to generate steep breaking waves as well. A shortcoming of the method discussed by Rapp and Melville is that is based solely on linear theory and does not account for nonlinear effects such as amplitude dispersion. Perlin and He [41] use weakly non-linear wave theory to modify a technique given by [15]. They were able to generate spilling through plunging waves while eliminating premature upstream breaking.

In this study, Rapp and Melville's dispersive focusing technique was briefly examined. Several wave packet families were calculated and implemented using a contour following motion program. The frequency band was limited to frequencies above

2.4Hz, to ensure deep water waves at 13cm water depth. The results yielded several cases of spilling breakers, but the more dramatic plunging waves were not created. As such, breaking waves generated using dispersive focusing are not included in the experimental results. However, the wave focusing technique was not studied extensively, and it is possible that plunging waves could be produced by fine-tuning the motion program and further varying the non-dimensional signal parameters.

4.1.2 Shoaling waves

In the results that follow, wave breaking was induced by propagating a monochromatic wave train over a constant slope section to a level plateau. In this shoaling method, the wave energy is focused into a smaller volume until breaking occurs. Since bottom effects become significant, these waves are fundamentally different from previously described deep water breaking waves. However, the geometries of the resulting breakers are similar to the deep water cases, and the breaking types are thus characterized using the same terminology (spilling, plunging, surging). Many researchers have utilized sloping bottoms to generate breaking waves in experimental facilities [40][47][51]. These sloped-bottom experiments model the near shore breakers apparent on coastlines around the world. In [40], Peregrine suggests that the results of such experiments depend on two parameters: the initial wave steepness, $a_0\varpi^2 / g$, and the bottom angle. Typical studies include a constant depth section before commencement of the gentle slope of less than 5 degrees, which is often closer to 1 degree. The small length scale of the tank used in these experiments required that the slope of the shoal be greater than those in previous studies.

The shoal section which induces breaking in this study is similar to that used by C.-P. Tsai et al [51]. With an angle of 15 degrees, or 1/(3.73), the slope is considered to be steep. Tsai et al. use experiments to test the applicability of current empirical formulas for wave shoaling and breaking indices on steep beaches of 1/3 and 1/5 slope, as well as a more gentle 1/10 slope. The formulas used in the comparison had been originally derived for gentle slopes (<1/10). They note that wave breaking over steep slopes becomes increasingly complex, due to the influence of reflected wave components and the short distance of shoaling. Their results show that for all slopes, the wave reflection coefficients are agreement with empirical formulas. For breaking criterion, slopes of 1/10 and 1/5 agree with empirical formulas, but those of 1/3 deviated considerably. The shoaling formula used by Shuto [47] to characterize wave transformation over changing depth did not correspond to the results for the 1/3 and 1/5 cases. Determining precise breaking parameters is beyond the scope of this study, and the reader is referred to [51] for more information on these coefficients. A more general implication of their study is that shoaling waves on steep slopes, such as the one used in this experiment, can result in complex wave transformation that is not well understood by current empirical models.

In a preliminary qualitative experiment, an adjustable angle slope was created to examine its influence on wave breaking. Angles of 5, 10, 15, 20, 30 and 45 degrees were tested by capturing video of the breaking event over various frequencies and amplitudes in filtered tap water. It became immediately apparent that spilling breakers were the most common type for all cases. The strength of the spilling breaker was directly related to wave steepness of the generated wave train. Waves with long wavelengths and small amplitudes resulted in gentle spilling waves, and conversely, steeper waves caused strong spilling. The fifteen degree slope was chosen for further study because it resulted in the most energetic breaking, and was thought to be best choice for creating plunging breakers.

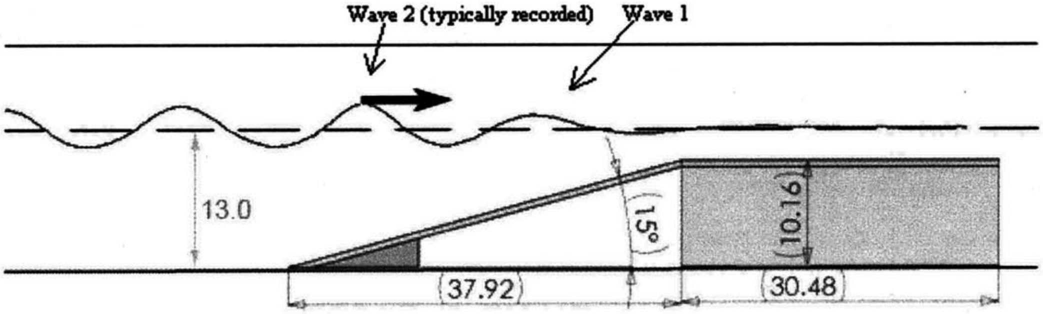

Figure 4-1: A dimensional illustration (cm) of the shoal section used to induce breaking and the free surface. The front of an advancing wave train (not to scale) is superimposed on the picture to show the small amplitude 1st wave.

The sloping shoal transitions to a flat plateau at a height of 10.2 cm. This plateau allows small amplitude waves at the front of the wave train to propagate down the tank without creating significant upstream disturbances. Since each case studied was defined by wave amplitude, frequency, and number of waves in the train, the wave chosen for post-processing had to have an amplitude near the average of its train. Unfortunately the constant amplitude wave near the center of the envelope could not be used, as reflections and disturbances due to leading waves affect the breaking characteristics of the waves that follow. Accordingly, the second wave in the packet was analyzed, as it tended to break most cleanly while maintaining a pre-breaking amplitude near that of the train. The length of the train was reduced to 5 paddle cycles, since waves after the second were typically disregarded. The ramp and plateau were made of polycarbonate plates to allow light transmission from beneath the tank and because of their resistance to corrosion.

4.2 Numerical Breaking Wave Generation

The methods for inducing wave breaking in the numerical realm are comparable to those used in experimental techniques, and they have also yielded similar results. Refinements in the original numerical schemes and increased computer processing capability have improved the methods through inclusion of more physical effects. Recent advancements have yielded simulations which include parameters such as viscosity, surface tension, and the air-effects, but they have also been limited to very small scales.

Developed by Longuet-Higgins and Cokelet [32], the boundary element method is a potential flow formulation which has been widely used to calculate the free surface deformation during the early stages of breaking. An integral equation is solved along the fluid surface to determine the spatial dependence of motion at discrete time steps. The results of [32] are appropriate for long wavelength waves because the viscosity and surface tension terms were neglected. After calculating the form of periodic gravity waves in water, they induce breaking by applying a sinusoidal pressure function, 90 degrees out of phase with the waves, to the water surface. This type of surface forcing is believed to be analogous to breaking caused by wind-wave interaction. A resulting jet forms near the wave crest and falls under gravity when pressure forcing is removed. The potential flow constraint of irrotational flow requires that such boundary element calculations stop before the jet impacts the surface.

Duncan cites several other important boundary element calculations in [19]. Shultz et al [46] simulate the effect of converging tank walls by modifying the dynamic free surface boundary condition, and their results are in general agreement with the experimental work performed in converging wave tank [52]. Dommermuth et al [16]used boundary element calculations to simulate an entire wave tank and wavemaker, and they are able to generate plunging breakers by dispersive focusing. They found the nonlinear potential theory to be excellent in comparison with experimental measurements. Grilli et al [24] use a similar technique to compute wave profiles for solitary waves on slopes of 1/100, 1/35, 1/15 and 1/8. They derive a breaking criterion for milder slopes based on a slope parameter and their results agree well with laboratory experiments.

To bypass the computational limitations which required waves to break close to the wavemaker, Tulin [50] divides the simulated tank into many subdomains along its length and is able to create breaking waves due to the Benjamin-Feir instability. In this method, breaking events are produced which occur at distances around 100 wavelengths from the wavemaker. The instability method produced a range of jet sizes for a given wavetrain as well as an important criterion regarding initial breaking conditions which has been verified since its introduction. The simulations showed that if fluid particle velocity in the crest of any wave reaches the linear group velocity, then the wave crest will break within 0.25 wave periods. Tulin also used boundary element calculations to explore the surface tension effects of short wavelength waves and spilling breakers. A plot from Tulin's results for short waves and discussion of the results are located in section 3.X of the previous chapter.

In addition to boundary element calculations, several numerical approaches have been used to examine the turbulence and fluid structures that develop over the entire breaking process. Chen et al [12] overcome the potential flow limitations by using a two-dimensional volume-of-fluid (VOF) method to create viscous plunging waves in a liquid-gas medium. In the VOF approach, two different phases are approximated by the flow of a single fluid whose physical properties, such as density and viscosity, change across the interface. A volume concentration function is used to locate the interface. Chen et al. implement a direct numerical simulation of the Navier-Stokes equations and compute the motion of a gas and liquid through jet impact and splash-up. A wave with an initial slope greater than the Stokes limit quickly evolves to form =a plunging breaker. They found that the liquid splash-up of the initial impact is primarily composed of fluid from the jet. Although the properties used in the simulation were not equivalent to air and water (ratio of fluid densities was $\overline{\rho}=10^{-2}$, and ratio of fluid viscosities was $\overline{\mu}=0.4$), the results appear qualitatively similar to a short wavelength plunging breaker. Images from the results are shown in figure 4-2.

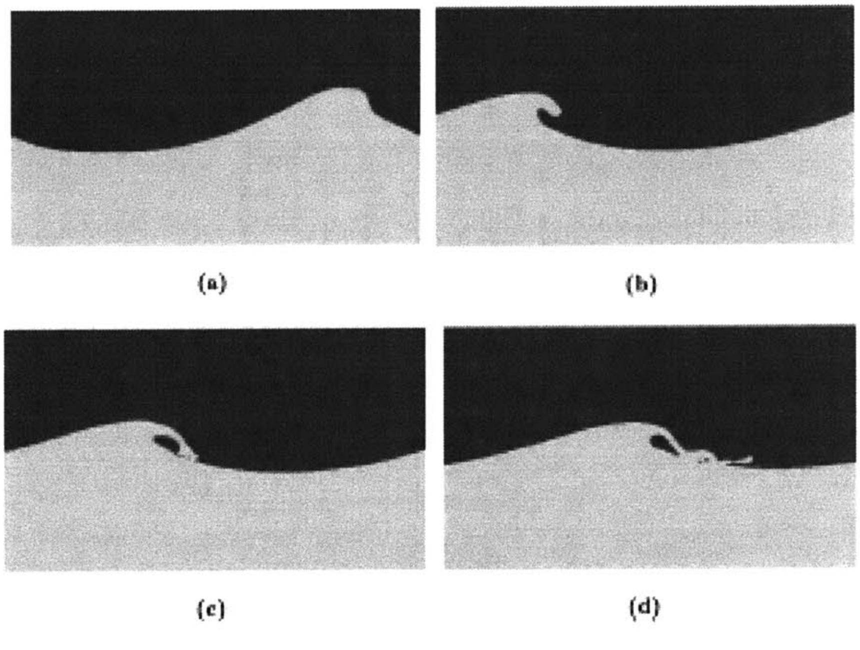

Figure 4-2: Sequence of images from the VOF simulations of a plunging breaker performed in [12]. The physical properties are not those of air and water, but the VOF method allowed them to simulate past the jet impact and track the gas motion.

Similar to the VOF method, the level set technique has also been implemented to solve for unsteady free surface flows. Rather than using volume concentration to locate the interface, the level set technique expresses fluid density and viscosity as a smooth function of distance from the interface. It is an Eulerian method in which the points on the grid represent the distance from the interface, and the sign of the function indicates in which fluid the points reside. Iafrati et al [27] use a Navier-Stokes solver with the level set method to simulate a plunging wave resulting from flow over a bump. They use the properties of air and water and establish qualitative agreement with the experimental observations of Bonmarin [7]. Though the results from VOF and level set method simulations have not been quantitatively verified through experiments, they mark a distinct improvement over potential theory in that they can incorporate viscosity and turbulence as well as the dynamics of flow on the air-side of the interface.

More recently, Hendrickson [25] creates breaking waves with a Direct Numerical Simulation of the Navier-Stokes equations using a modified level set method. At the air-water boundary, the traditional level set method is subject to shear discontinuities due to large velocity gradients near the surface of the air-side. To resolve the shear errors, Hendrickson implements an asymmetric smoothing function which extends the level set boundary layer on the air-side only. Having tested and analyzed the resulting modified level set, Hendrickson uses the improved method to generate a deep-water wave breaking database. The database includes 36 wave cases from non-breaking through plunging breakers, and the cases are used to examine energy dissipation due to breaking as well as the transfer of energy across the air-water interface.

Hendrickson uses several methods to initiate breaking waves in her study. She describes the first of the four as an impulsively started Airy wave. This technique is similar to that used by Chen et al., where the simulation begins with an overly steep wave that quickly breaks. This technique does not include a solution for the air, and the initially steep wave requires further velocity smoothing across the interface to reduce the resulting high surface vorticity. The second method includes a solution of the two-phase Airy wave problem satisfying all viscous free-surface boundary conditions. The two-fluid Airy wave solution creates waves with a better balance between kinetic and potential energy than in the impulsively started method. Both methods feature waves with a breaking threshold which lies between $0.2 < ak < 0.3$. If ak is sufficiently small for linear theory to apply, the generated waves will not break.

The other methods of generating breaking waves require the use of surface forcing. In one technique, Hendrickson applies a normal pressure force which moves at a given speed to an initially flat surface of quiescent fluid. Depending upon the magnitude of the initial surface forcing, the wave will either propagate without breaking or form a breaking wave once the forcing has been removed. This method requires a slow ramp-up of the surface tension to prevent it from damping out the developing wave. The other surface forcing technique is comparable to the Longuet-Higgins and Cokelet pressure forcing which was discussed previously. Both methods are robust and capable of generating the full range of breaking waves. The drawback to the flat surface forcing is that the plunging breaker tends to have an excess of horizontal momentum. The sinusoidal forcing works best when the amount of energy used is small and applied to waves with slopes near the breaking limit. This use of surface forcing to initiate breaking is analogous to breaking caused by wind forcing in nature.

In addition to using these four wave breaking techniques, Hendrickson varies the value of surface tension to create different types of breaking waves. Further details of this modification are discussed in Chapter 3.

4.3 Breaking Wave Database

To characterize the experimental set-up and determine the range of possible breaking wave cases to study, tests were performed over various frequencies and amplitudes in a well-mixed 10% IPA solution. The following database includes the wave breaking results at six equally spaced frequencies between 1.5-4 Hz. At each test frequency, the paddle amplitude began at a maximum of 2.5cm and was stepped down by 0.25cm in each successive run until waves no longer broke at the shoal. In some cases, the input amplitude was too large for the driving frequency, causing wave breaking off the paddle. These waves broke again once they reached the shoal, but they tended be turbulent before shoaling. The results include data from the wave probes and high speed video.

The wave gauges were used to provide information needed for the Reynolds number, Weber number, as well as to give insight into the potential energy lost to breaking. Two closely spaced probes at the start of the ramp were used to determine the phase speed, C_p, of the wave train before shoaling. The distance between the two probes divided by the average time shift between the measured packets was calculated as phase speed (refer to figure 2-2 for probe spacing and tank layout). The wavelength was found by dividing the phase speed by the wave frequency. The third, downstream probe measured the amplitude of the wavetrain after the breaking event. Time traces for most test cases are included below. The fractional potential energy remaining between the upstream and downstream probes is also plotted for each frequency over various amplitudes and breaking types. Potential energy is proportional to the square of the amplitude for linear waves, and though these waves are non-linear, this information provides a rough, first order estimate of energy dissipation which has been used by others [43] [25]. These energy losses are plotted against non-dimensional slope parameter, ak, of the upstream probe.

Five frames from the high speed video are included to illustrate the type of breaking in each case. The camera was positioned at a slight angle to resolve the third dimension. The images clearly show that the waves break differently at the wall. In the plunging case, for example, the jet and air entrainment are much more pronounced at the center of the wave. Transverse waves are also present, and appear as smaller ripples on the primary wave train. Further discussion of the wave breaking database can be found in section 4.4.

This page intentionally left blank.

4.3.1 Wave Frequency: 1.5Hz

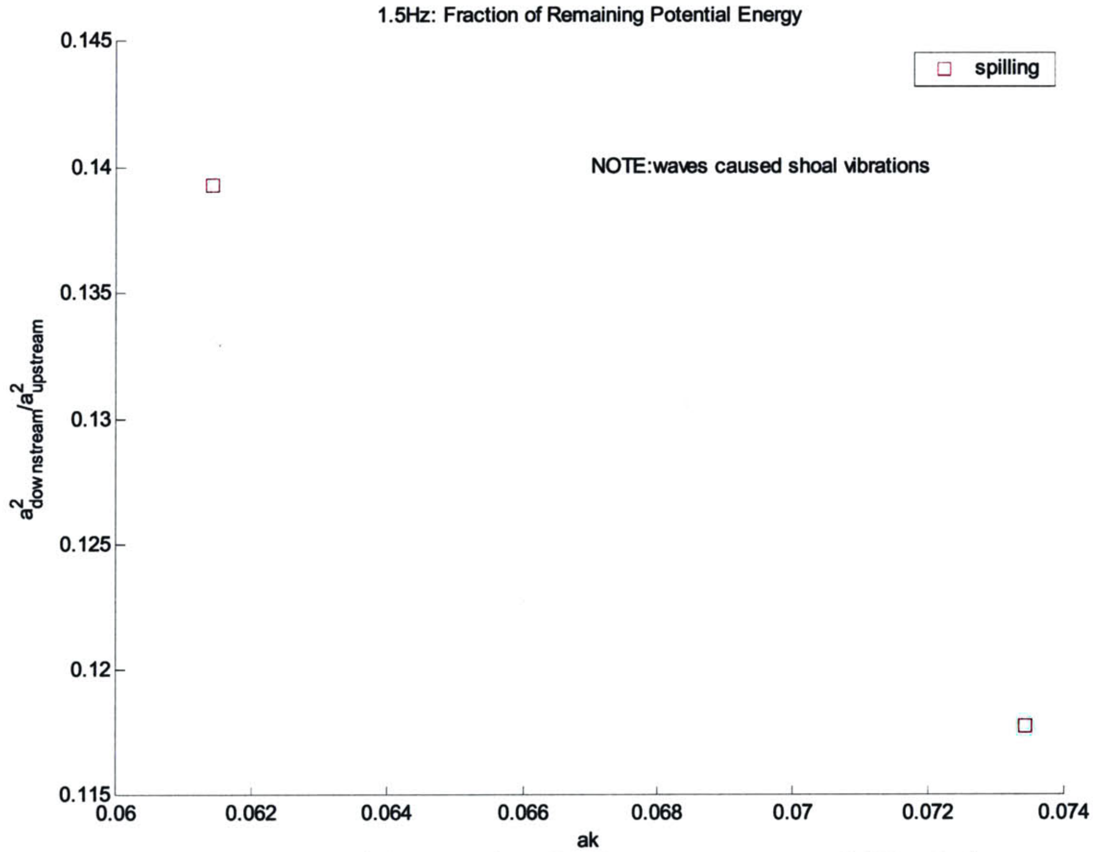

Figure4-3: Plot of the potential energy loss for the two test cases at 1.5Hz. Only two amplitudes were measured at this frequency, because tests were halted when the wave-induced shoal vibrations were observed.

freq. (Hz)	Upstream amp. (cm)	Upstream ak	Dwnstrm amp. (cm)	Energy Remaining Dwnstrm	WE	RE	lambda (cm)	meas. Cp (m/s)	Breaking Details
1.5	0.77	0.073	0.26	11.78%	14575	6.17E+05	65.6	0.98438	Spilling. waves moved shoal
1.5	0.68	0.061	0.26	13.93%	17688	7.02E+05	70.0	1.05	Spilling. waves moved shoal

Table 4-1: Summary of parameters and results for all 1.5Hz test cases.

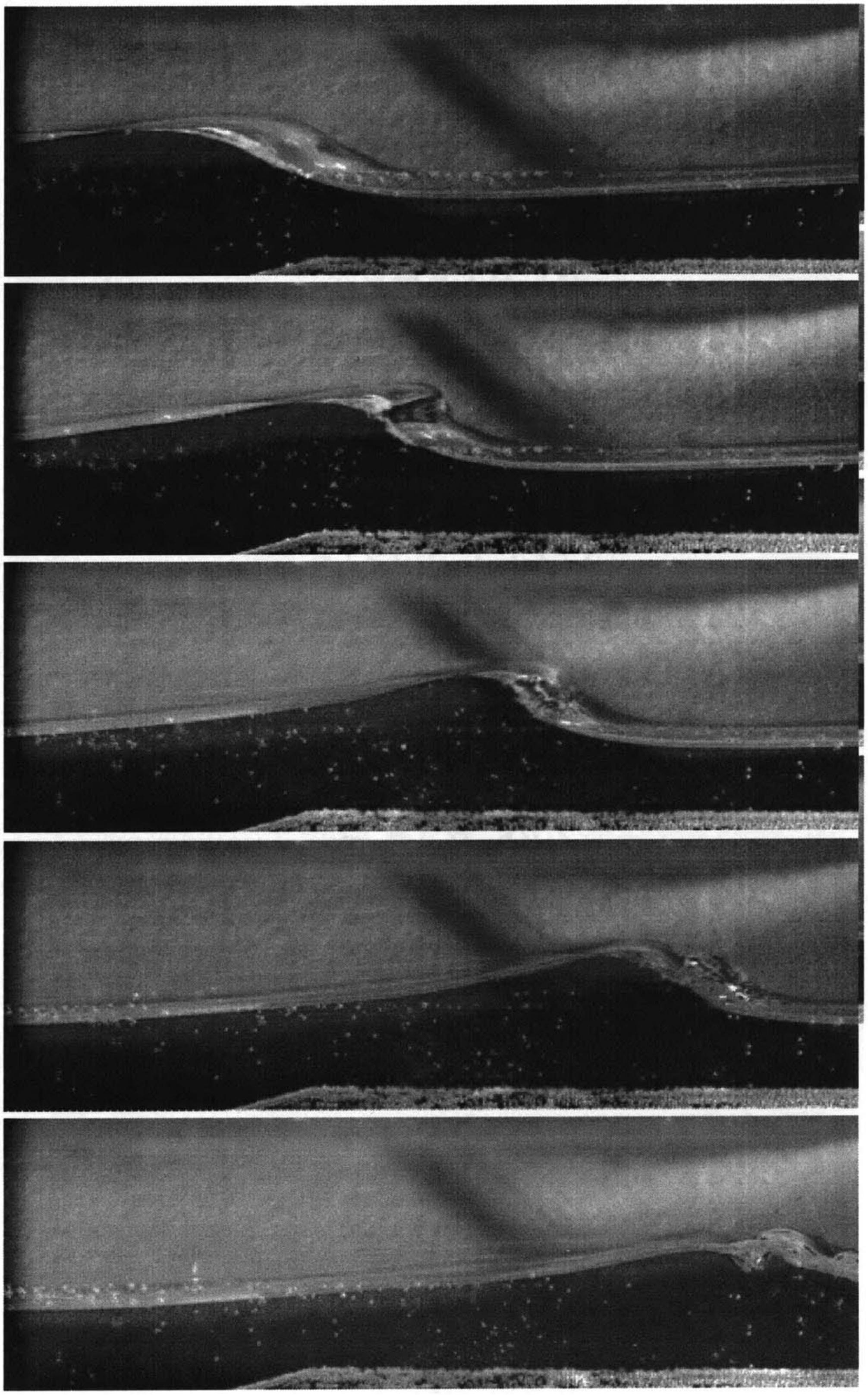

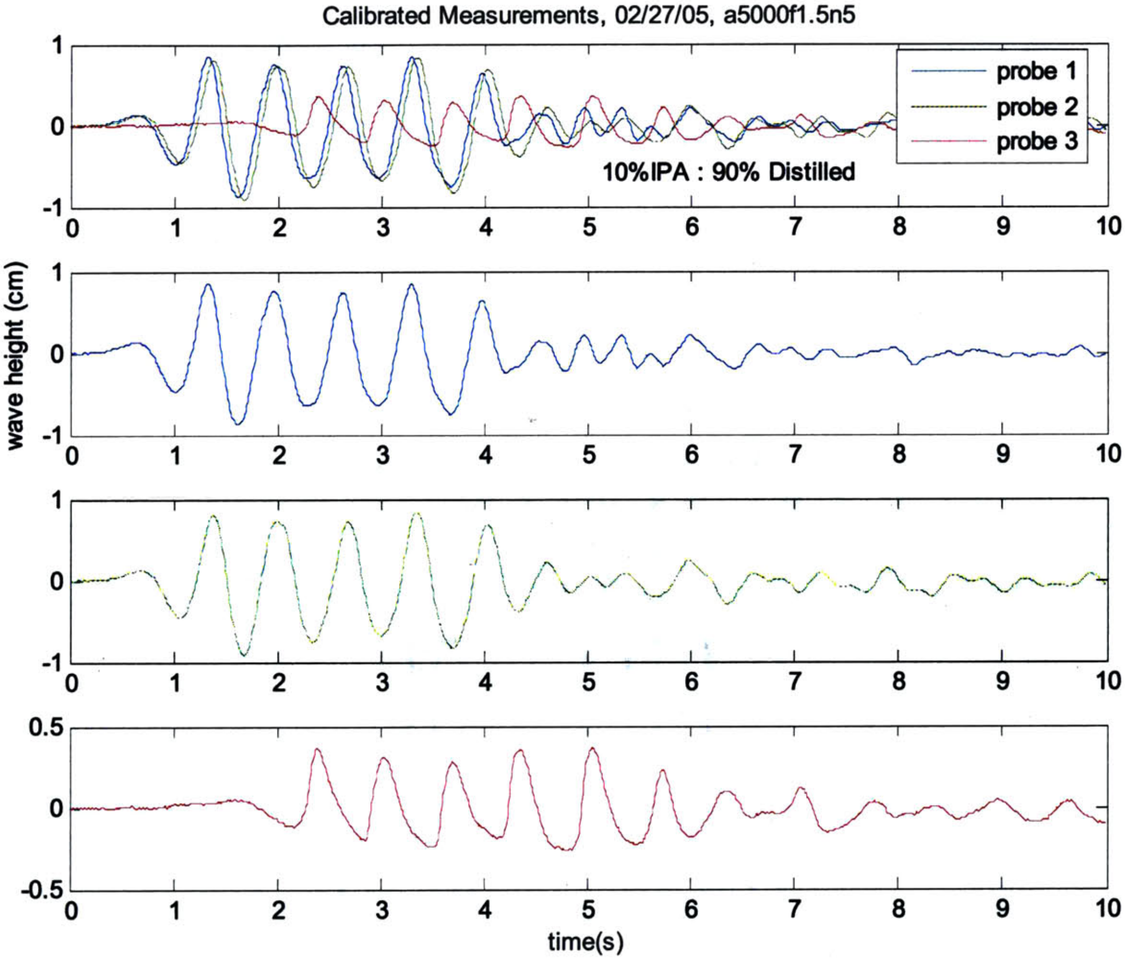

freq. (Hz)	Upstream amp. (cm)	Upstream ak	Dwnstrm amp. (cm)	Energy Remaining Dwnstrm	WE	RE	lambda (cm)	meas. Cp (m/s)	Breaking Details
1.5	0.77	0.073	0.26	11.78%	14575	6.17E+05	65.6	0.98438	Spilling. waves move shoal

Figure 4-4: Image frames (left page), probe data (top right), and wave kinematic (bottom right) parameters for the 1.5Hz frequency case generated in five wave paddle cycles. This was the largest input amplitude tested at 2.5 cm.

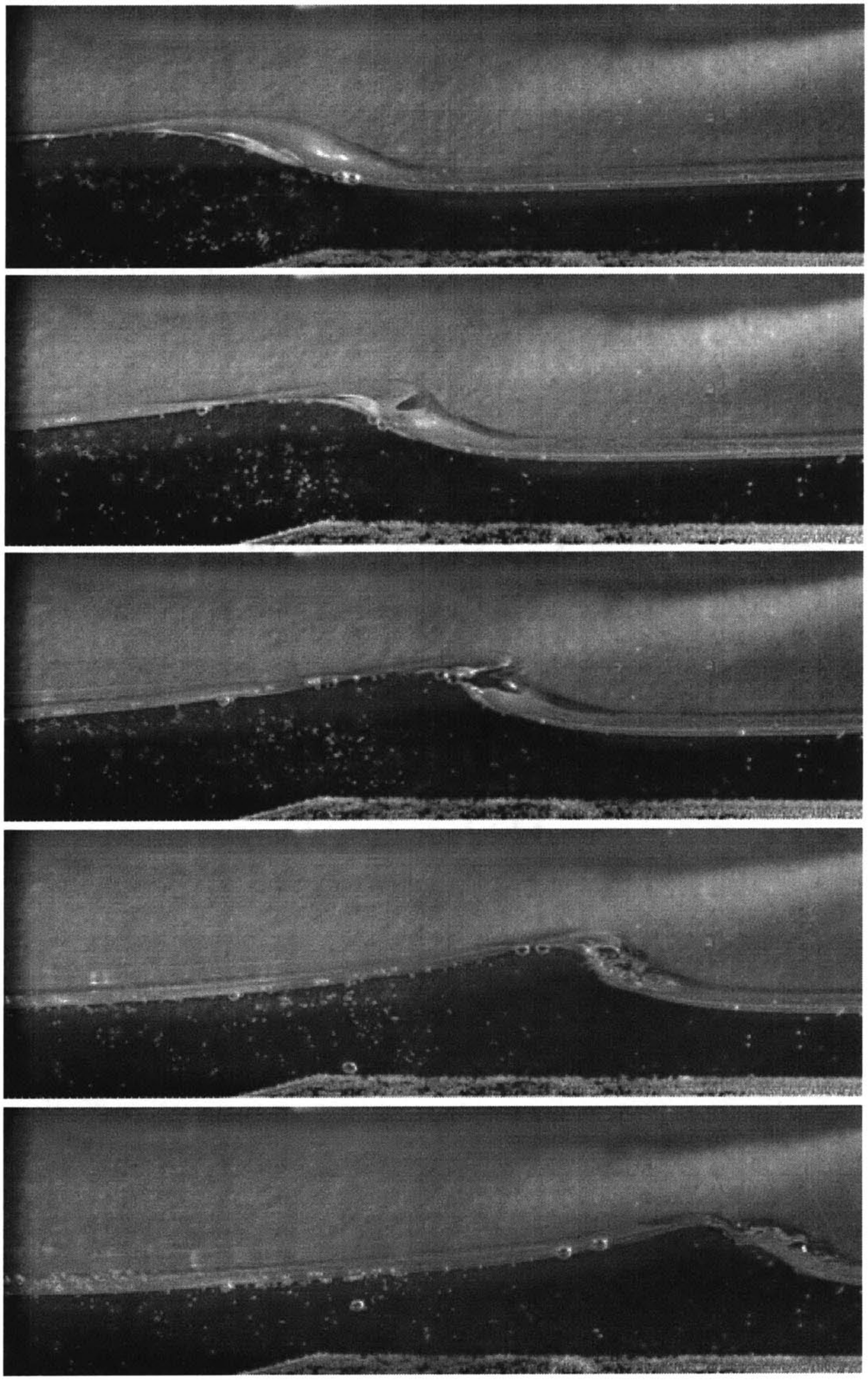

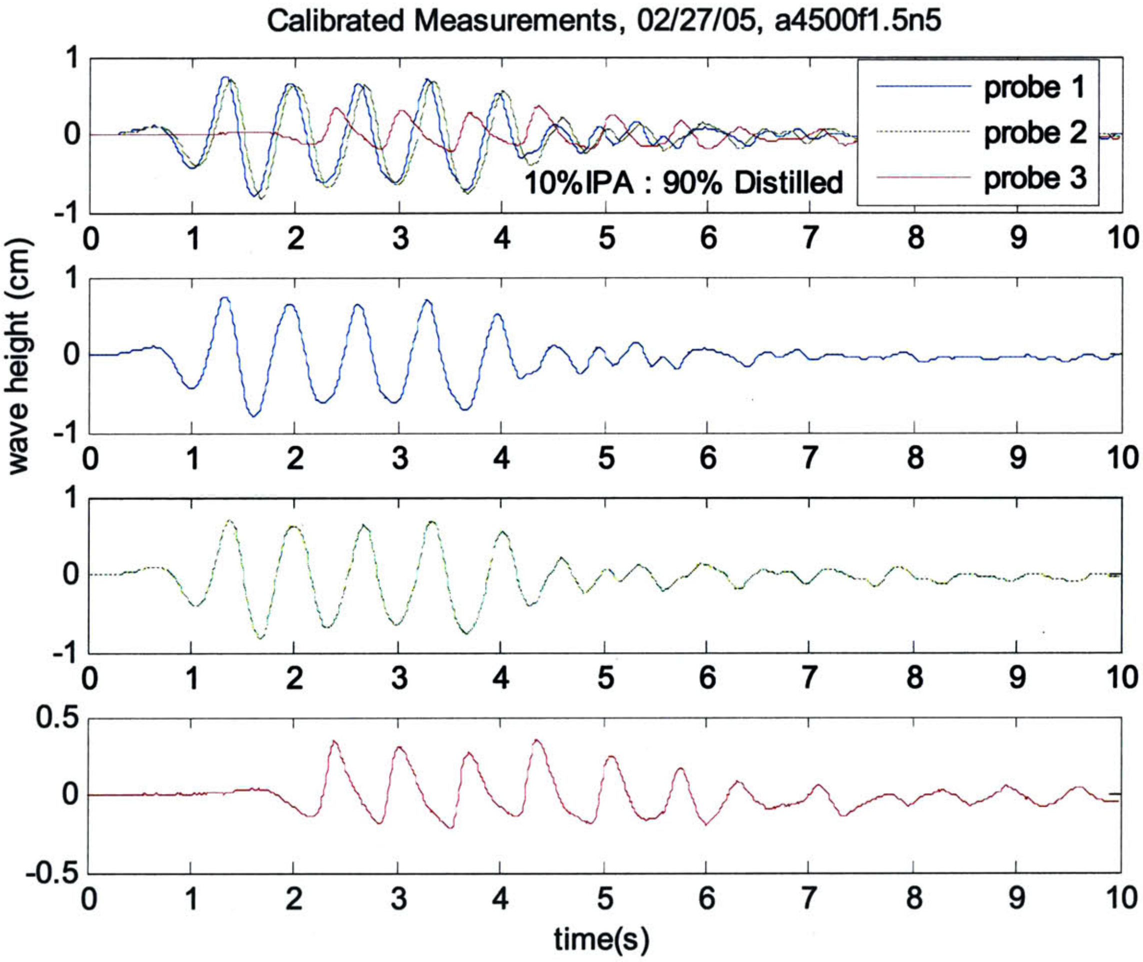

freq. (Hz)	Upstream amp. (cm)	Upstream ak	Dwnstrm amp. (cm)	Energy Remaining Dwnstrm	WE	RE	lambda (cm)	meas. Cp (m/s)	Breaking Details
1.5	0.68	0.061	0.26	13.93%	17688	7.02E+05	70.0	1.05	Spilling. waves move shoal

Figure 4-5: Image frames (left page), probe data (top right), and wave kinematic (bottom right) parameters for the 1.5Hz frequency case generated in five wave paddle cycles. The paddle amplitude was 2.25 cm.

This page intentionally left blank.

4.3.2 Wave Frequency: 2Hz

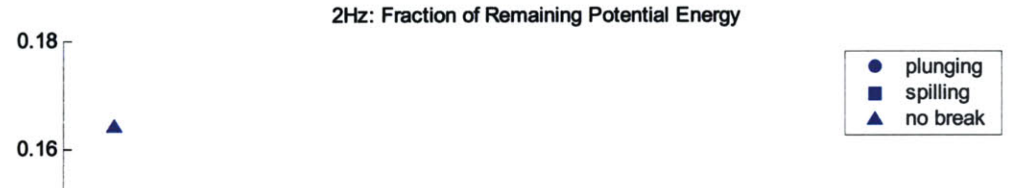

Figure 4-6: Plot of the potential energy loss for the 2Hz test cases. Notice the energy remaining lowers with increasing initial wave slope.

freq. (Hz)	Upstream amp. (cm)	Upstream ak	Dwnstrm amp. (cm)	Energy Remaining Dwnstrm	WE	RE	lambda (cm)	meas. Cp (m/s)	Breaking Details
2	1.08	0.186	0.23	4.46%	4505	2.56E+05	36.6	0.73256	plunging
2	0.97	0.159	0.22	5.06%	5197	2.82E+05	38.4	0.76829	plunging
2	0.84	0.135	0.20	5.60%	5597	2.96E+05	39.4	0.7875	spilling
2	0.70	0.112	0.17	6.15%	5597	2.96E+05	39.4	0.7875	spilling
2	0.58	0.088	0.15	6.48%	6528	3.28E+05	41.4	0.82895	spilling
2	0.46	0.068	0.19	16.41%	7072	3.46E+05	42.6	0.85135	no break

Table 4-2 Summary of parameters and results for all 2Hz test cases

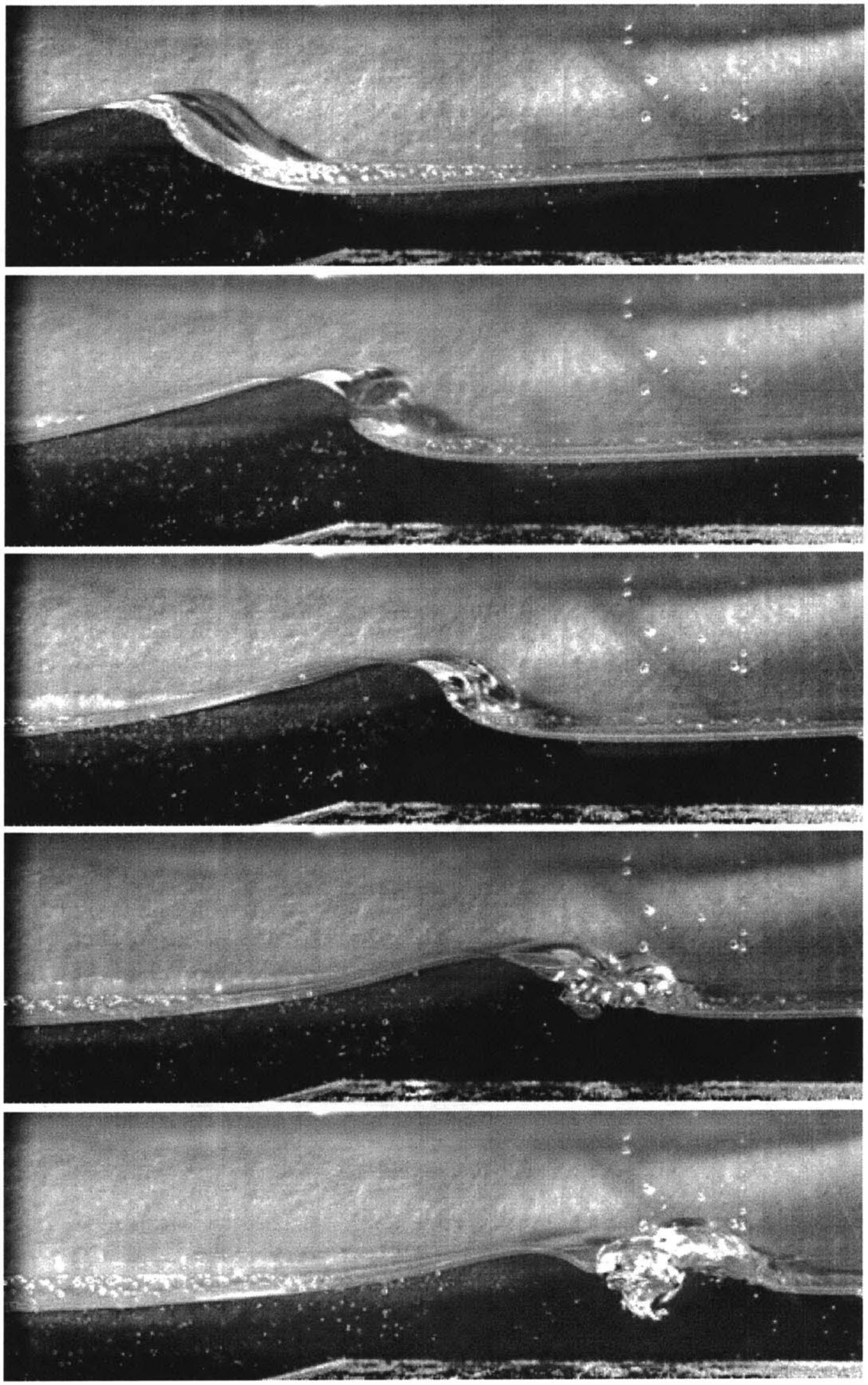

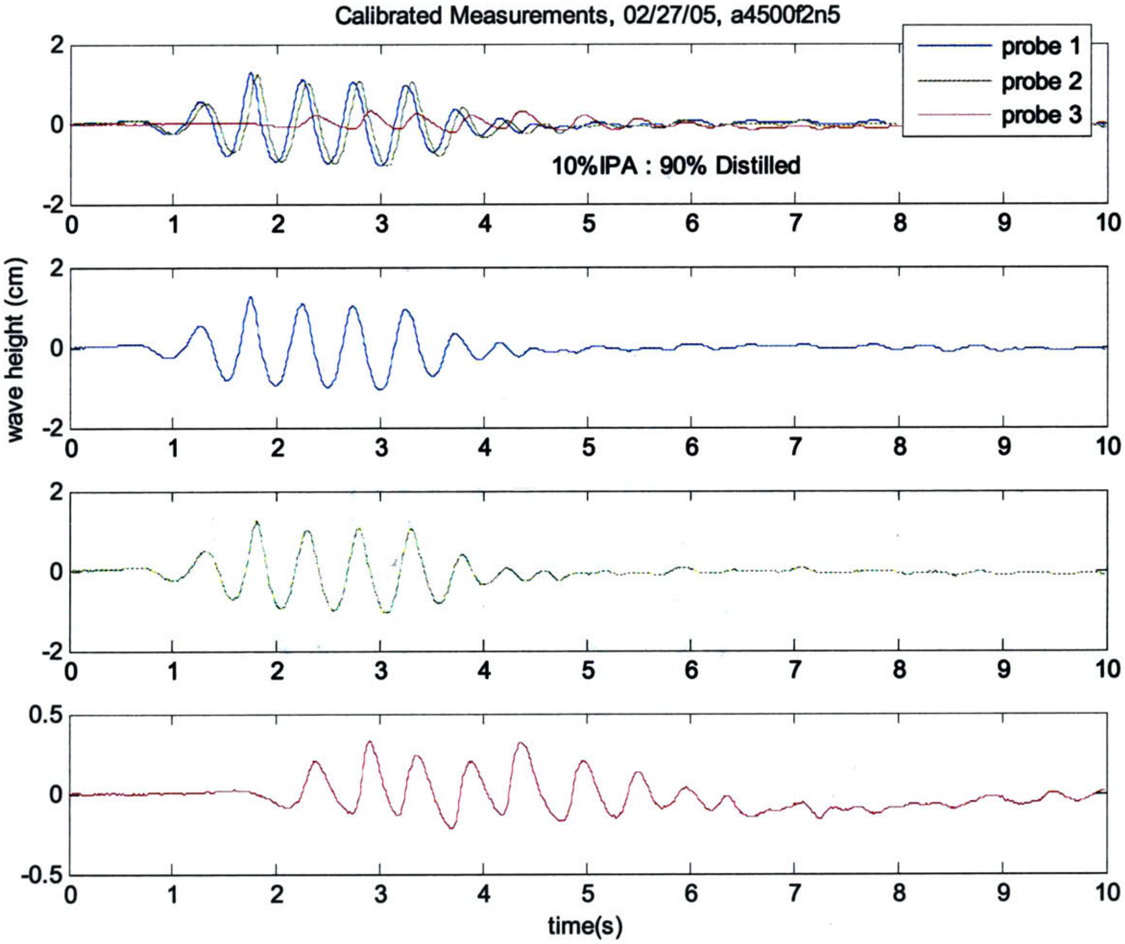

freq. (Hz)	Upstream amp. (cm)	Upstream ak	Dwnstrm amp. (cm)	Energy Remaining Dwnstrm	WE	RE	lambda (cm)	meas. Cp (m/s)	Breaking Details
2	1.08	0.186	0.23	4.46%	4505	2.56E+05	36.6	0.73256	plunging

Figure 4-7: Image frames (left page), probe data (top right), and wave kinematic (bottom right) parameters for the 2.0Hz frequency case generated in five wave paddle cycles. The paddle amplitude was 2.25 cm.

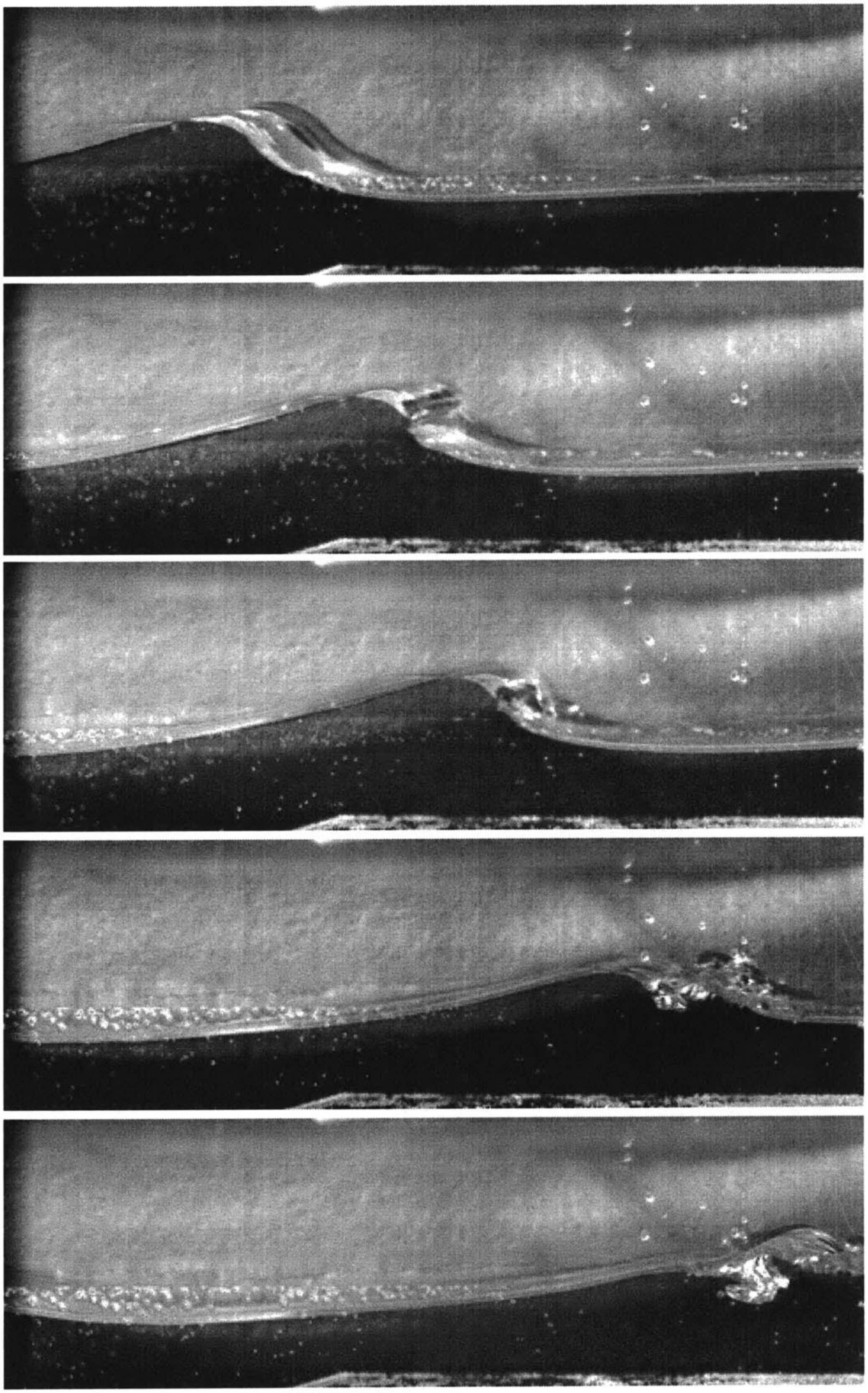

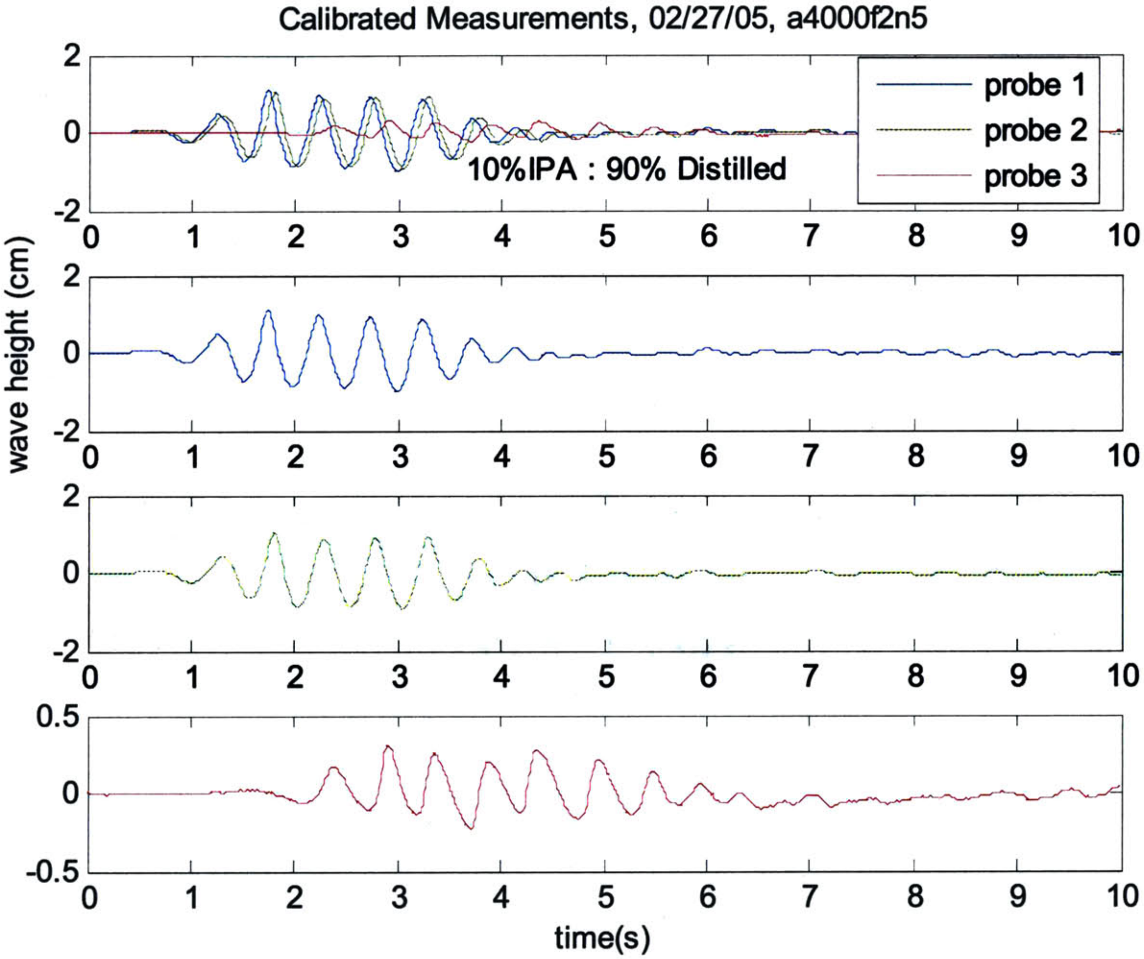

freq. (Hz)	Upstream amp. (cm)	Upstream ak	Dwnstrm amp. (cm)	Energy Remaining Dwnstrm	WE	RE	lambda (cm)	meas. Cp (m/s)	Breaking Details
2	0.97	0.159	0.22	5.06%	5197	2.82E+05	38.4	0.76829	plunging

Figure 4-8: Image frames (left page), probe data (top right), and wave kinematic (bottom right) parameters for the 2.0Hz frequency case generated in five wave paddle cycles. The paddle amplitude was 2.0 cm.

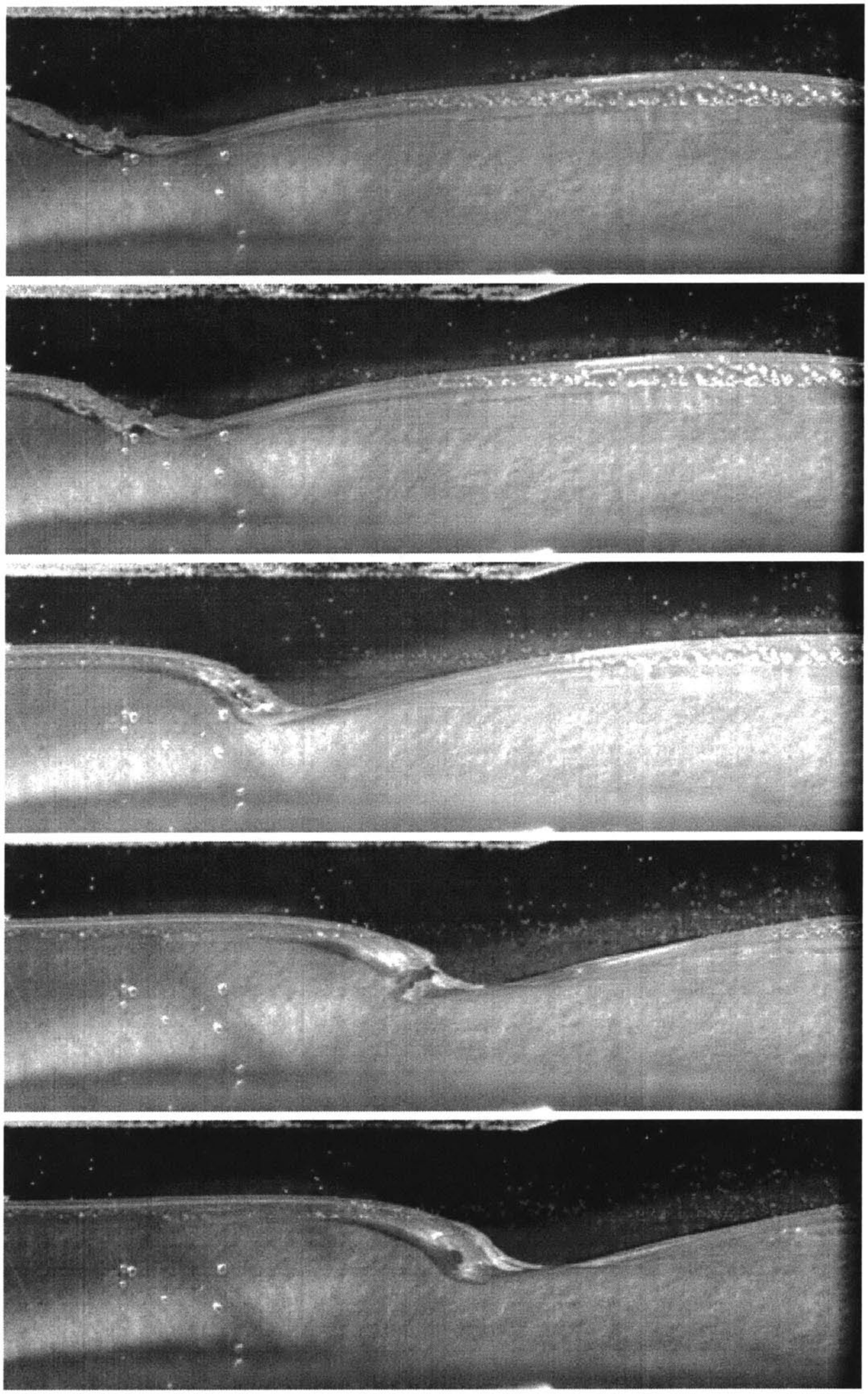

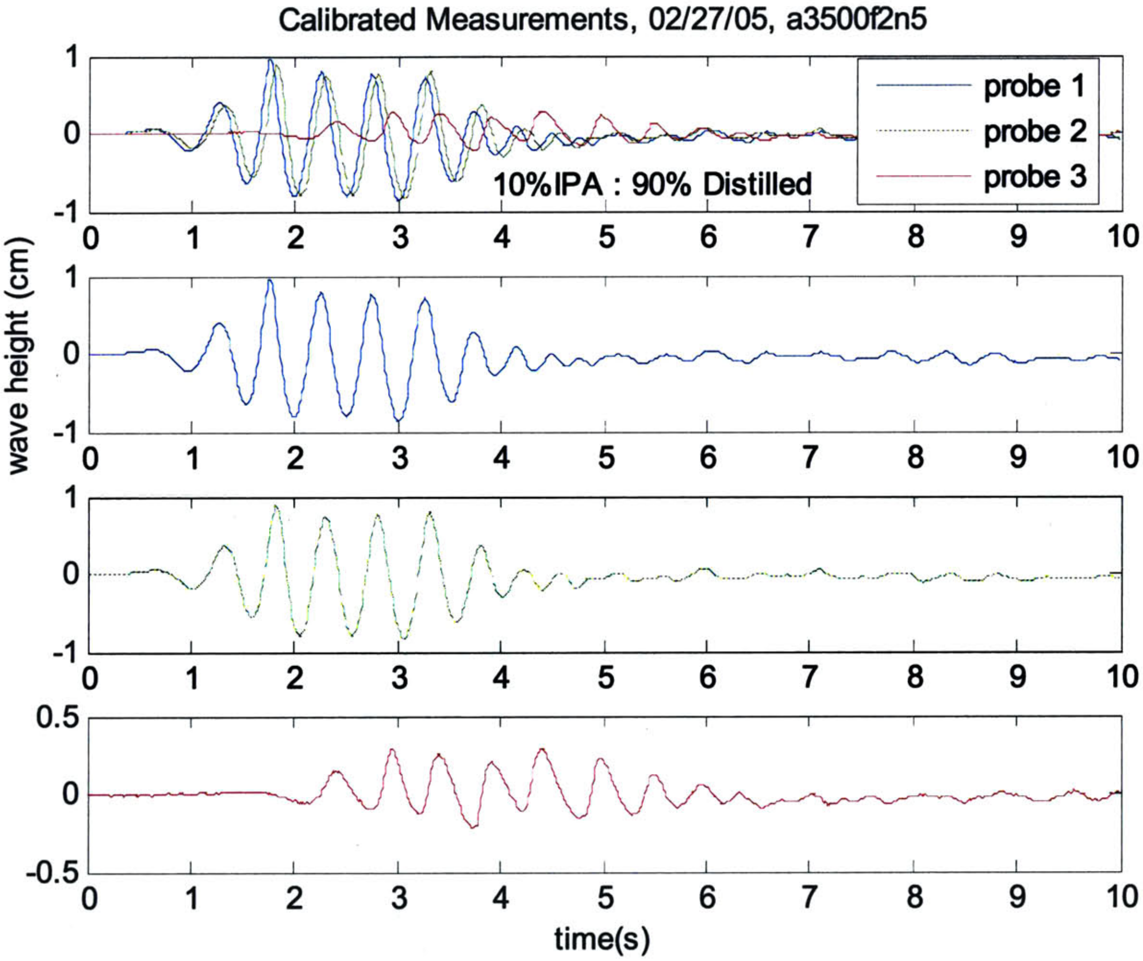

freq. (Hz)	Upstream amp. (cm)	Upstream ak	Dwnstrm amp. (cm)	Energy Remaining Dwnstrm	WE	RE	lambda (cm)	meas. Cp (m/s)	Breaking Details
2	0.84	0.135	0.20	5.60%	5597	2.96E+05	39.4	0.7875	spilling

Figure 4-9: Image frames (left page), probe data (top right), and wave kinematic (bottom right) parameters for the 2.0Hz frequency case generated in five wave paddle cycles. The paddle amplitude was 1.75 cm.

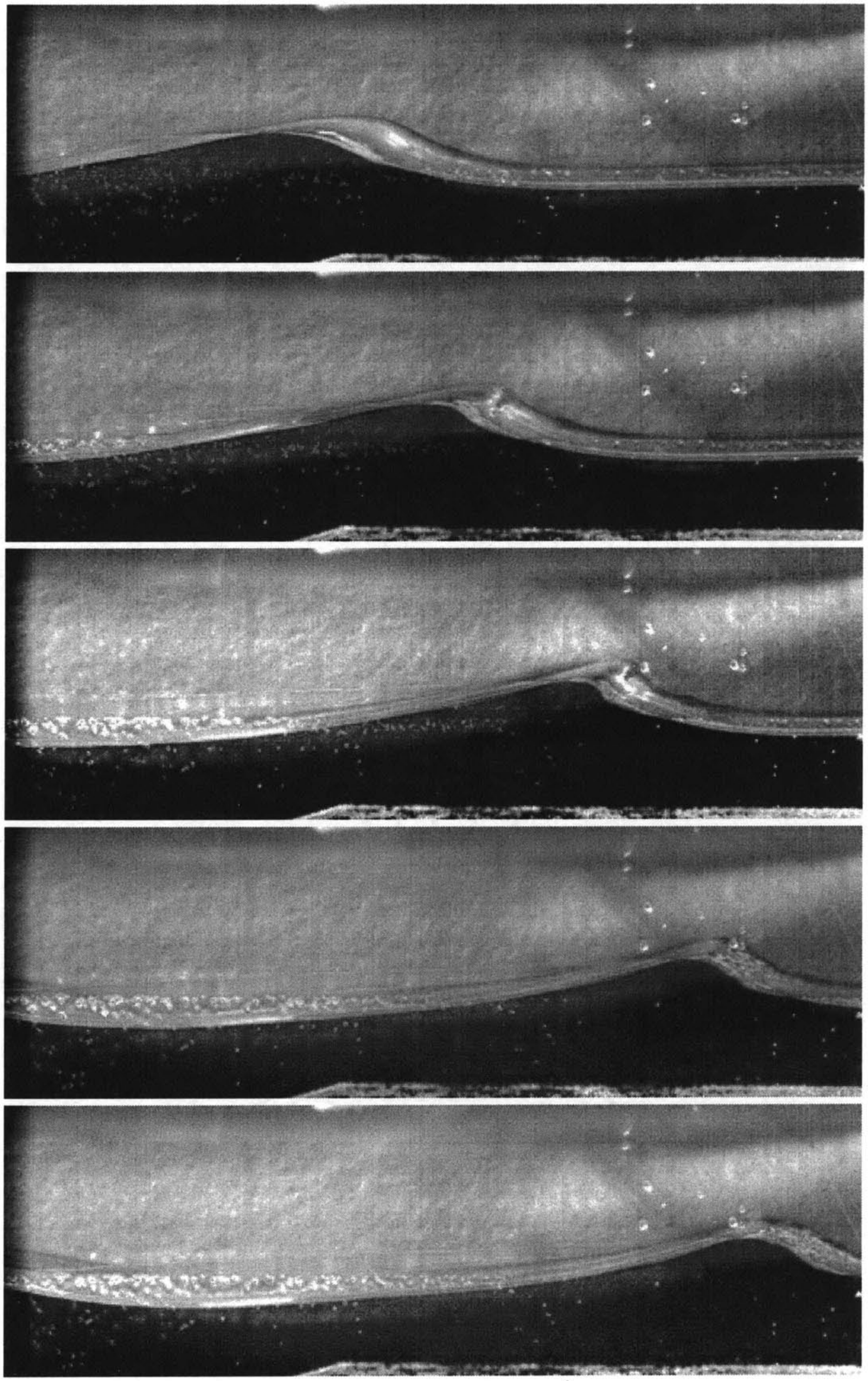

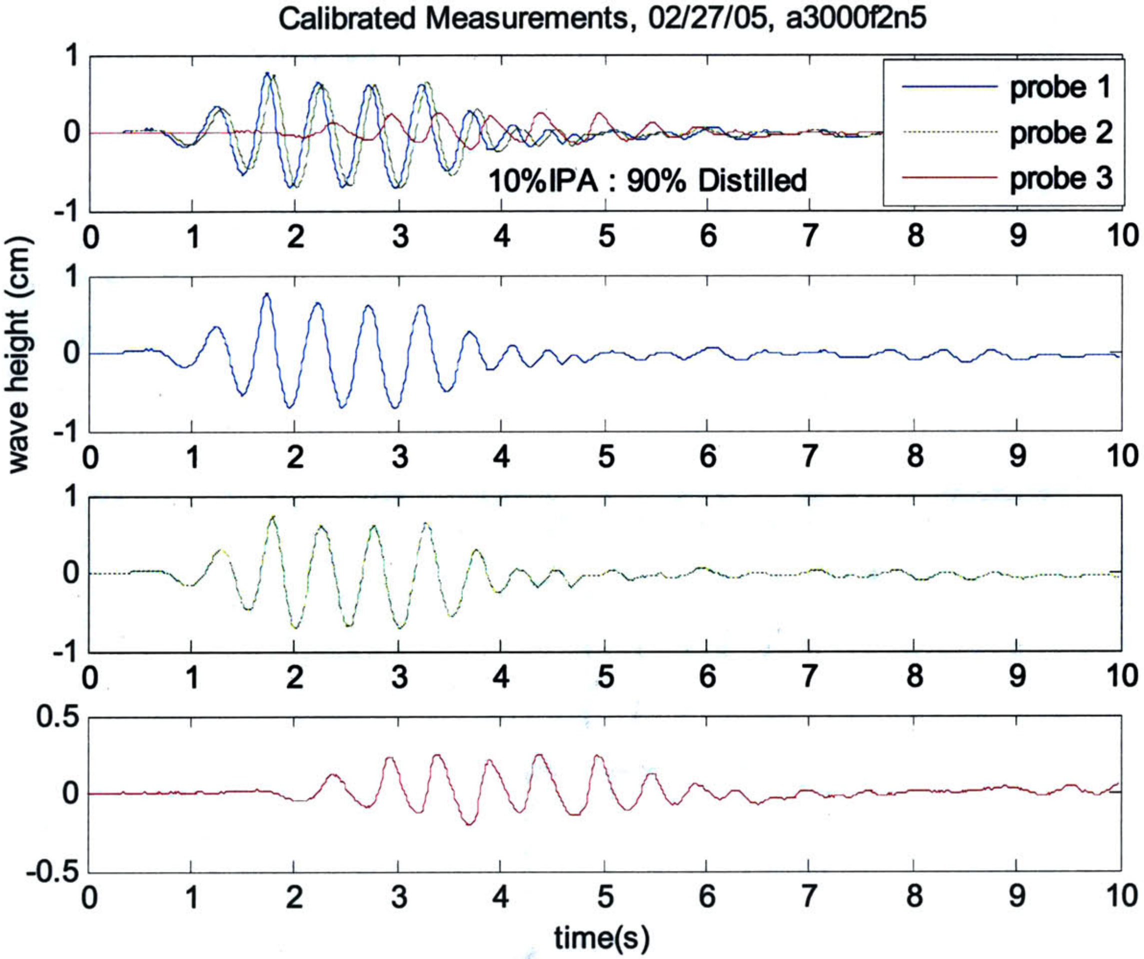

freq. (Hz)	Upstream amp. (cm)	Upstream ak	Dwnstrm amp. (cm)	Energy Remaining Dwnstrm	WE	RE	lambda (cm)	meas. Cp (m/s)	Breaking Details
2	0.70	0.112	0.17	6.15%	5597	2.96E+05	39.4	0.7875	spilling

Figure 4-10: Image frames (left page), probe data (top right), and wave kinematic (bottom right) parameters for the 2.0Hz frequency case generated in five wave paddle cycles. The paddle amplitude was 1.5 cm.

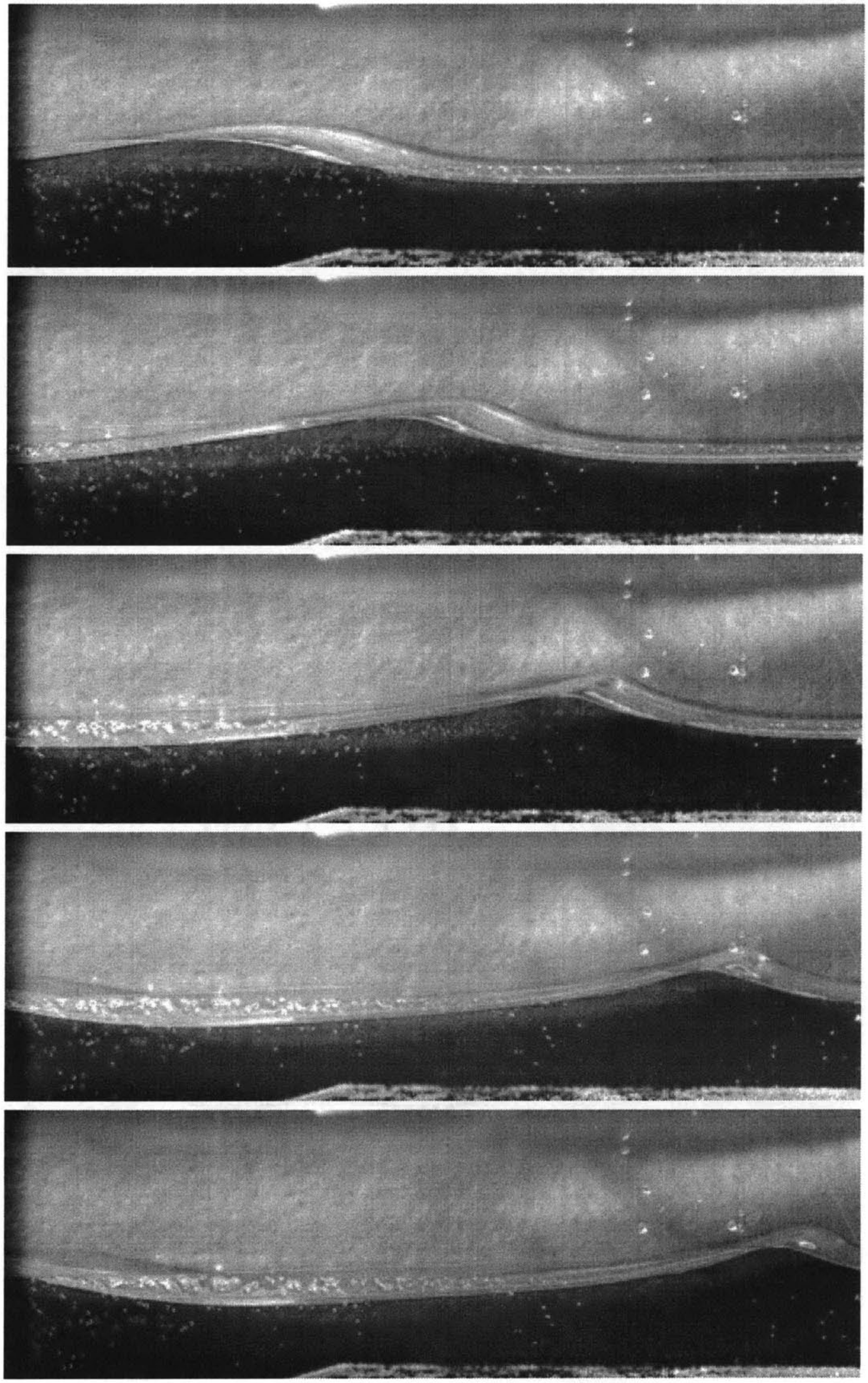

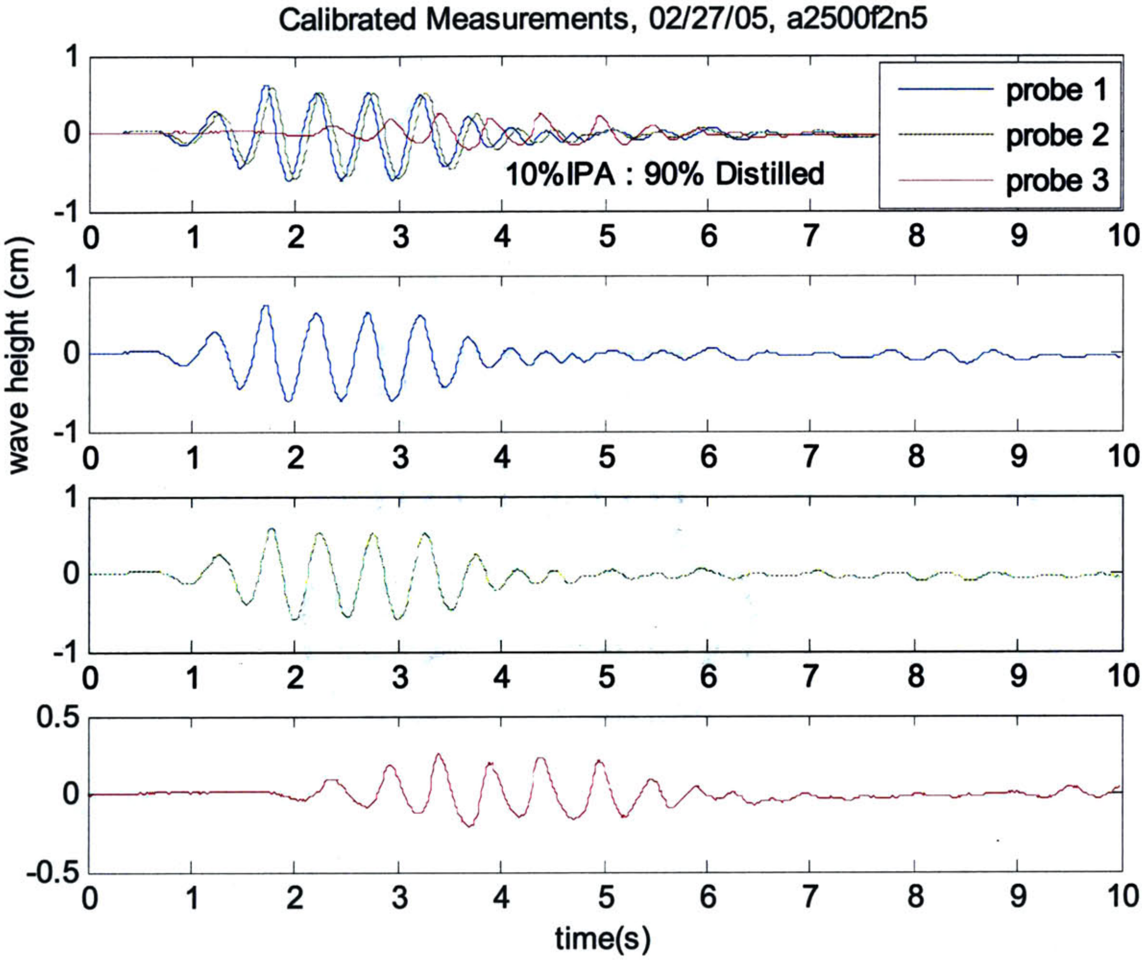

Calibrated Measurements, 02/27/05, a2500f2n5

freq. (Hz)	Upstream amp. (cm)	Upstream ak	Dwnstrm amp. (cm)	Energy Remaining Dwnstrm	WE	RE	lambda (cm)	meas. Cp (m/s)	Breaking Details
2	0.58	0.088	0.15	6.48%	6528	3.28E+05	41.4	0.82895	spilling

Figure 4-11: Image frames (left page), probe data (top right), and wave kinematic (bottom right) parameters for the 2.0Hz frequency case generated in five wave paddle cycles. The paddle amplitude was 1.25 cm.

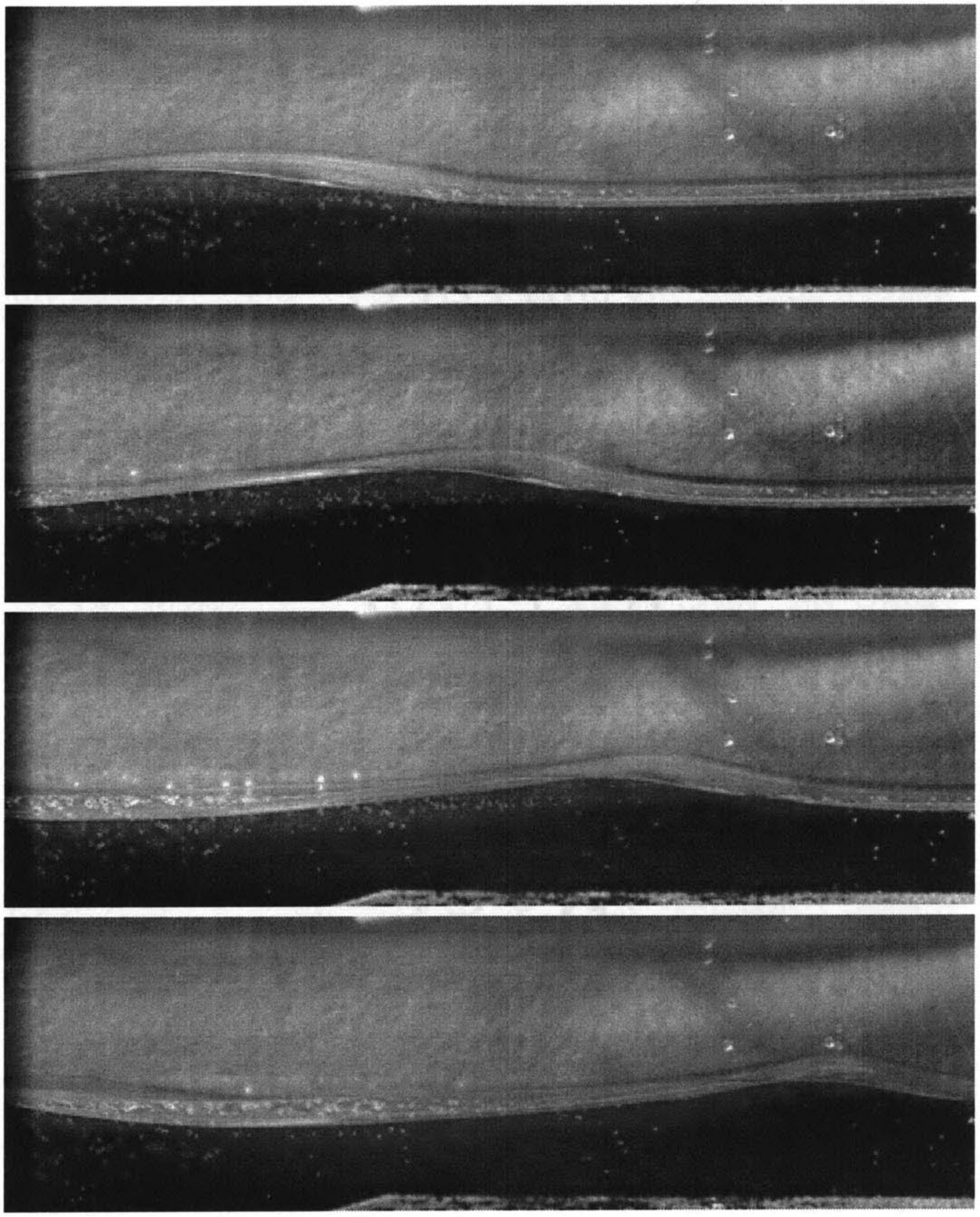

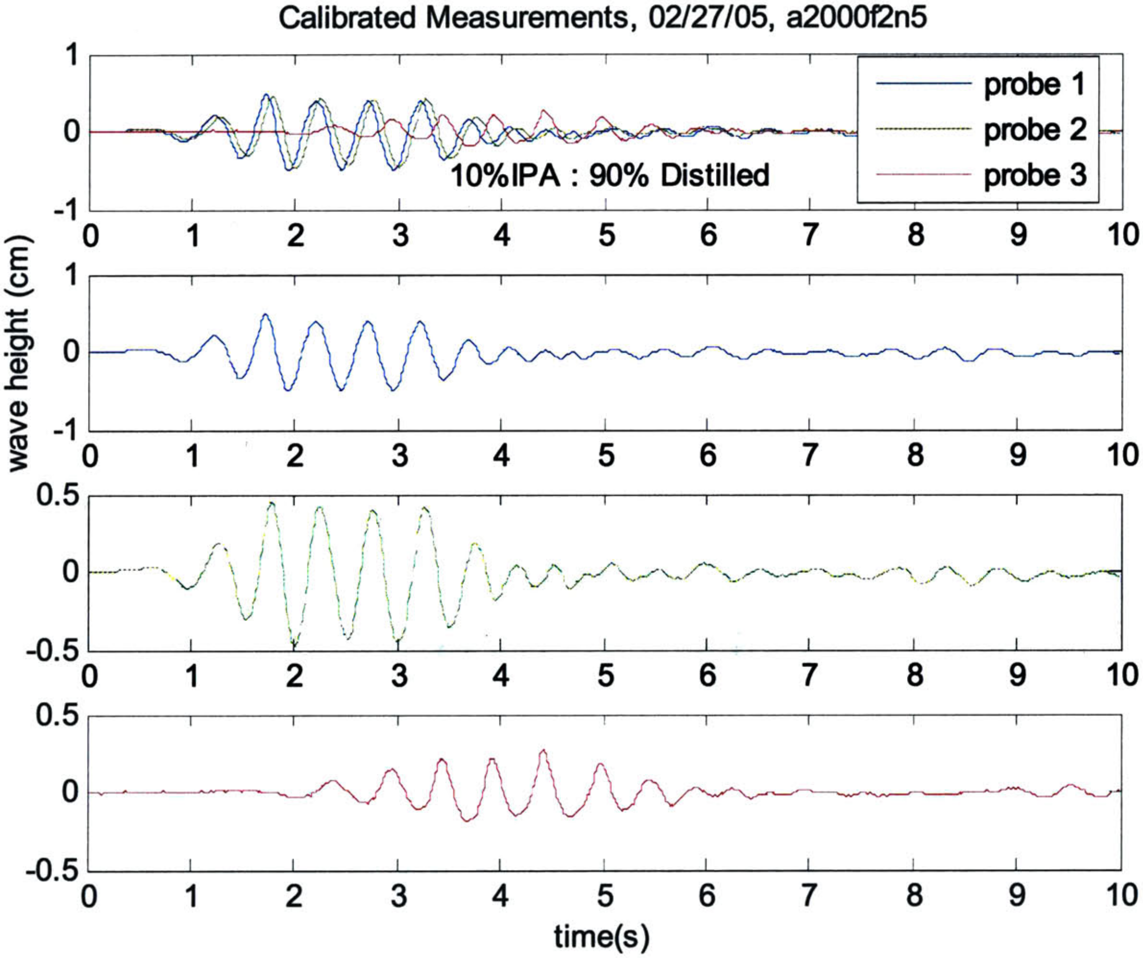

freq. (Hz)	Upstream amp. (cm)	Upstream ak	Dwnstrm amp. (cm)	Energy Remaining Dwnstrm	WE	RE	lambda (cm)	meas. Cp (m/s)	Breaking Details
2	0.46	0.068	0.19	16.41%	7072	3.46E+05	42.6	0.85135	no break

Figure 4-12: Image frames (left page), probe data (top right), and wave kinematic (bottom right) parameters for the 2.0Hz frequency case generated in five wave paddle cycles. The paddle amplitude was 1.0 cm.

This page intentionally left blank.

4.3.3 Wave Frequency: 2.5Hz

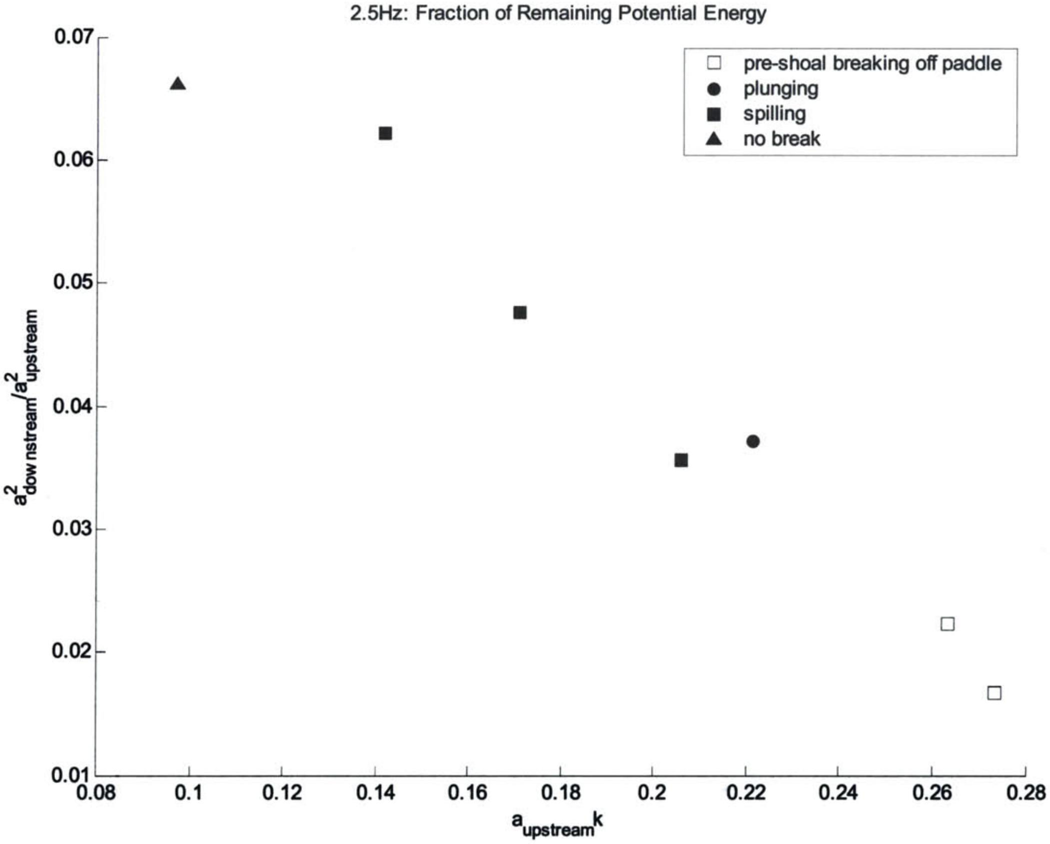

Figure 4-13 (top): Plot of the potential energy loss for the 2.5Hz test cases. Notice the energy remaining lowers with increasing upstream slope.

Freq. (Hz)	Upstream amp. (cm)	Upstream ak	Dwnstrm amp. (cm)	Energy Remaining Dwnstrm	WE	RE	lambda (cm)	meas. Cp (m/s)	Breaking Details
2.5	1.14	0.273	0.15	1.67%	2591	1.64E+05	26.3	0.65625	spilling breaks off paddle
2.5	1.08	0.263	0.16	2.23%	2436	1.58E+05	25.7	0.64286	spilling breaks off paddle
2.5	0.96	0.221	0.19	3.72%	2944	1.79E+05	27.4	0.68478	plunging
2.5	0.84	0.206	0.16	3.57%	2436	1.58E+05	25.7	0.64286	spilling
2.5	0.73	0.171	0.16	4.76%	2760	1.72E+05	26.8	0.67021	spilling
2.5	0.57	0.142	0.14	6.22%	2292	1.52E+05	25.2	0.63	spilling
2.5	0.41	0.097	0.10	6.61%	2591	1.64E+05	26.3	0.65625	no break (images not included)

Table 4-3: Summary of parameters and results for all 2.5 Hz test cases.

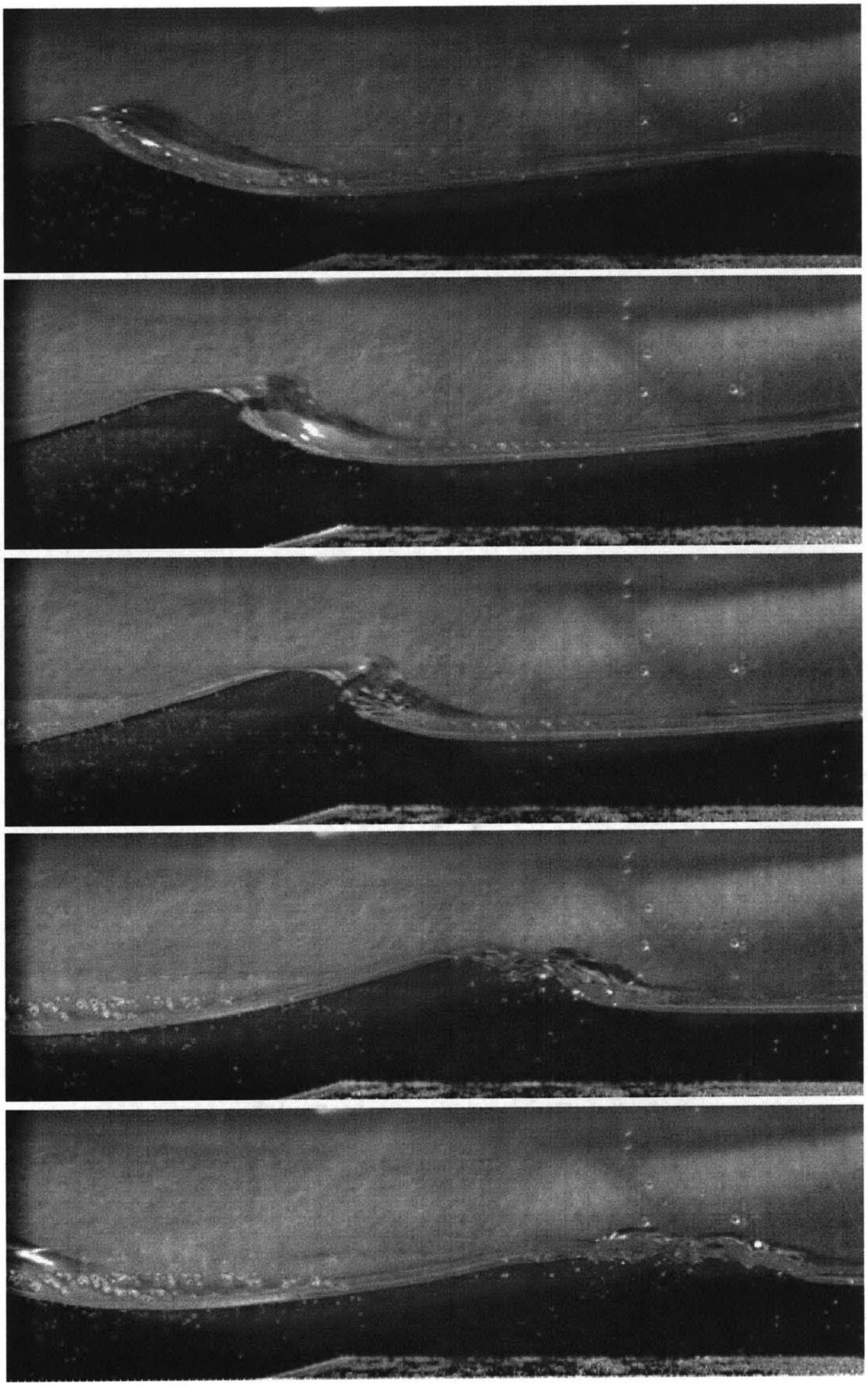

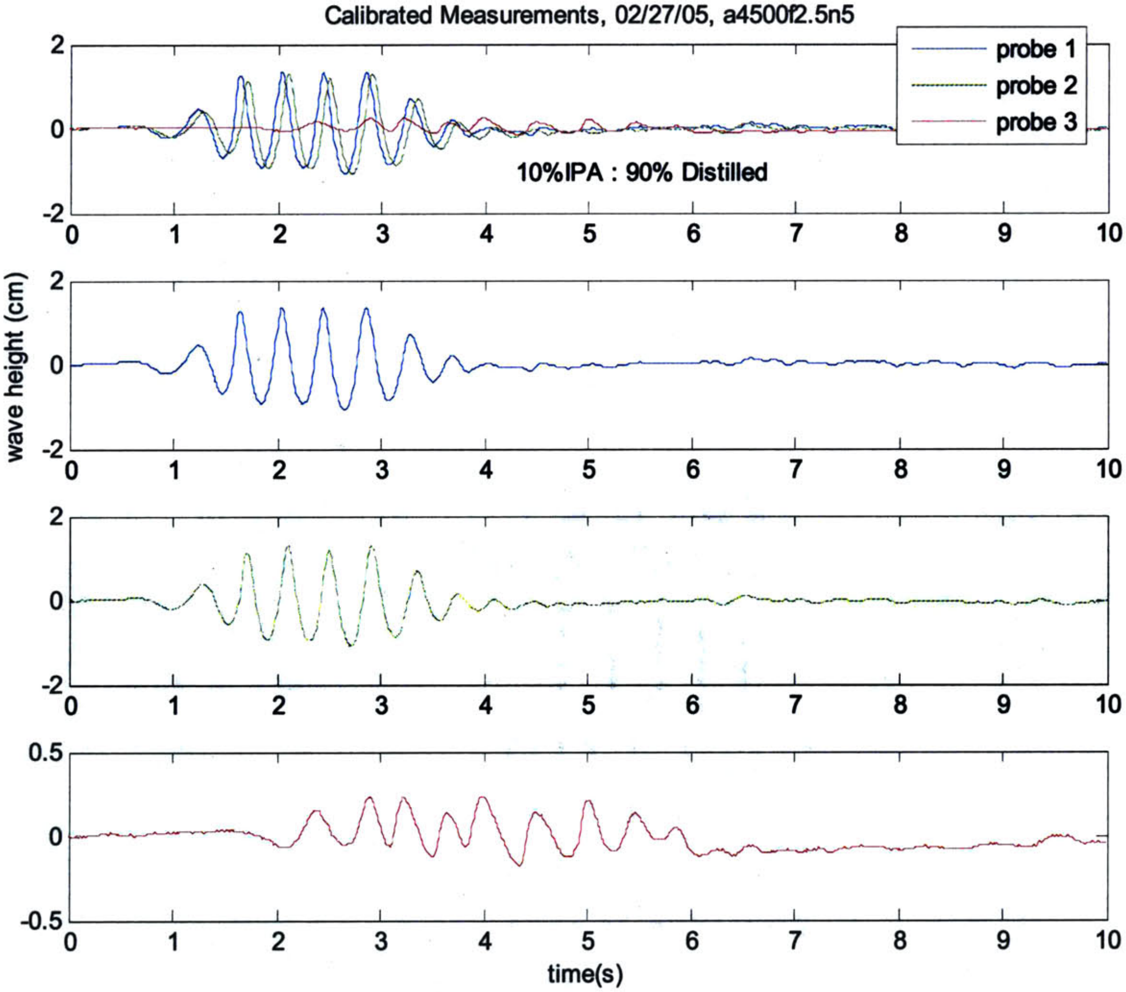

freq. (Hz)	Upstream amp. (cm)	Upstream ak	Dwnstrm amp. (cm)	Energy Remaining Dwnstrm	WE	RE	lambda (cm)	meas. Cp (m/s)	Breaking Details
2.5	1.14	0.273	0.15	1.67%	2591	1.64E+05	26.3	0.65625	spilling breaks off paddle

Figure 4-14: Image frames (left page), probe data (top right), and wave kinematic (bottom right) parameters for the 2.5 Hz frequency case generated in five wave paddle cycles. The paddle amplitude was 2.25 cm.

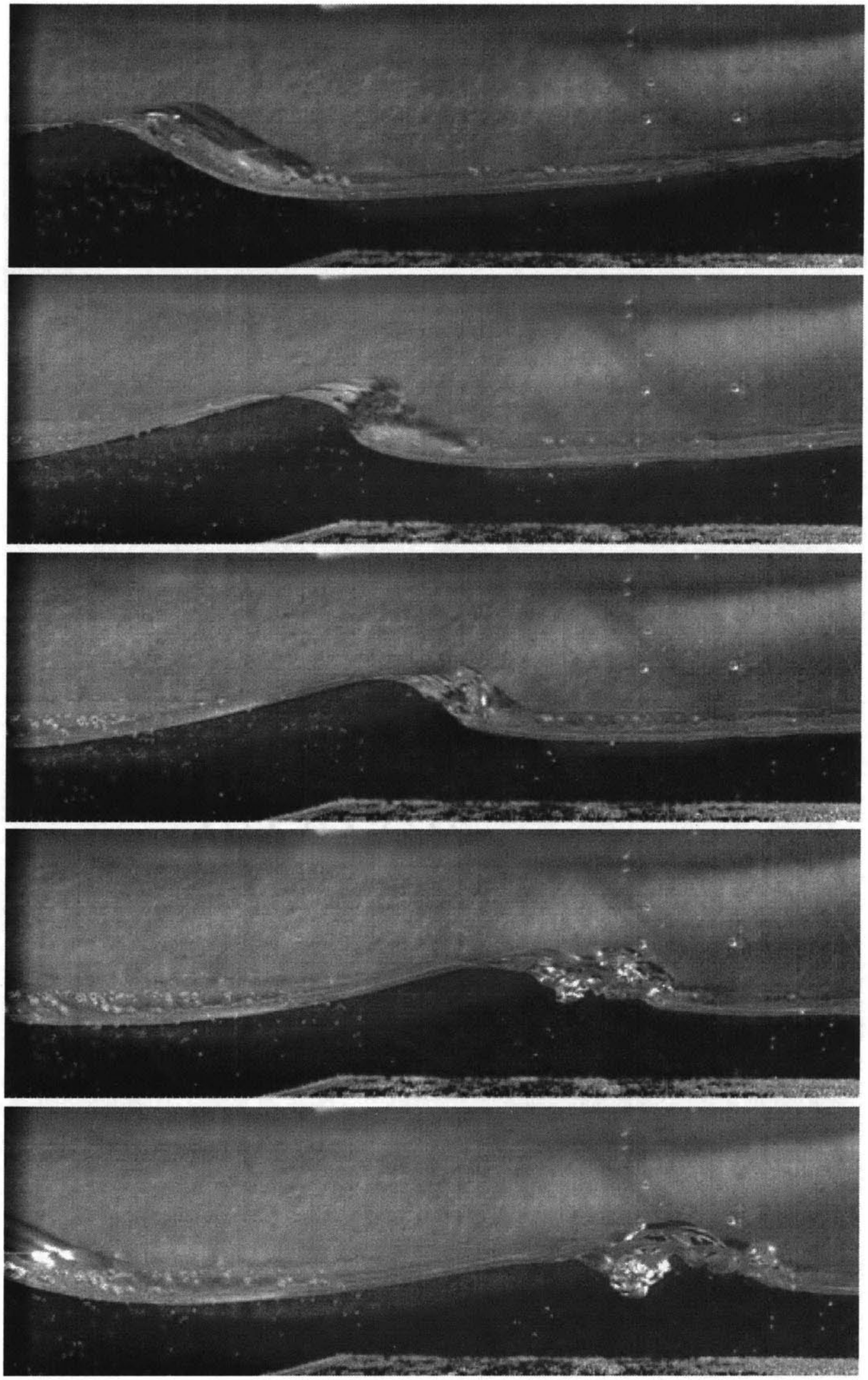

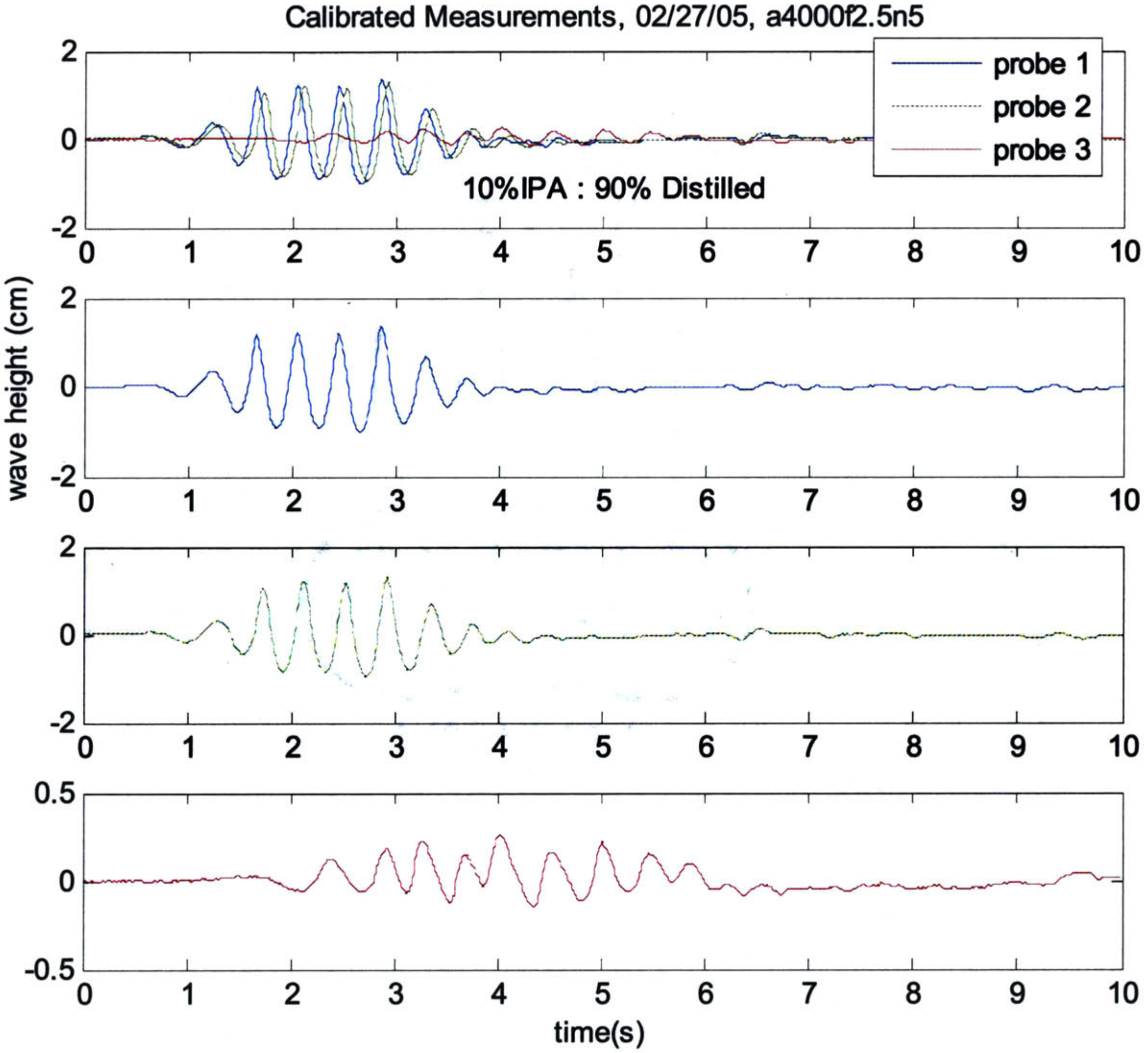

freq. (Hz)	Upstream amp. (cm)	Upstream ak	Dwnstrm amp. (cm)	Energy Remaining Dwnstrm	WE	RE	lambda (cm)	meas. Cp (m/s)	Breaking Details
2.5	1.08	0.263	0.16	2.23%	2436	1.58E+05	25.7	0.64286	spilling breaks off paddle

Figure 4-15: Image frames (left page), probe data (top right), and wave kinematic (bottom right) parameters for the 2.5 Hz frequency case generated in five wave paddle cycles. The paddle amplitude was 2.0 cm.

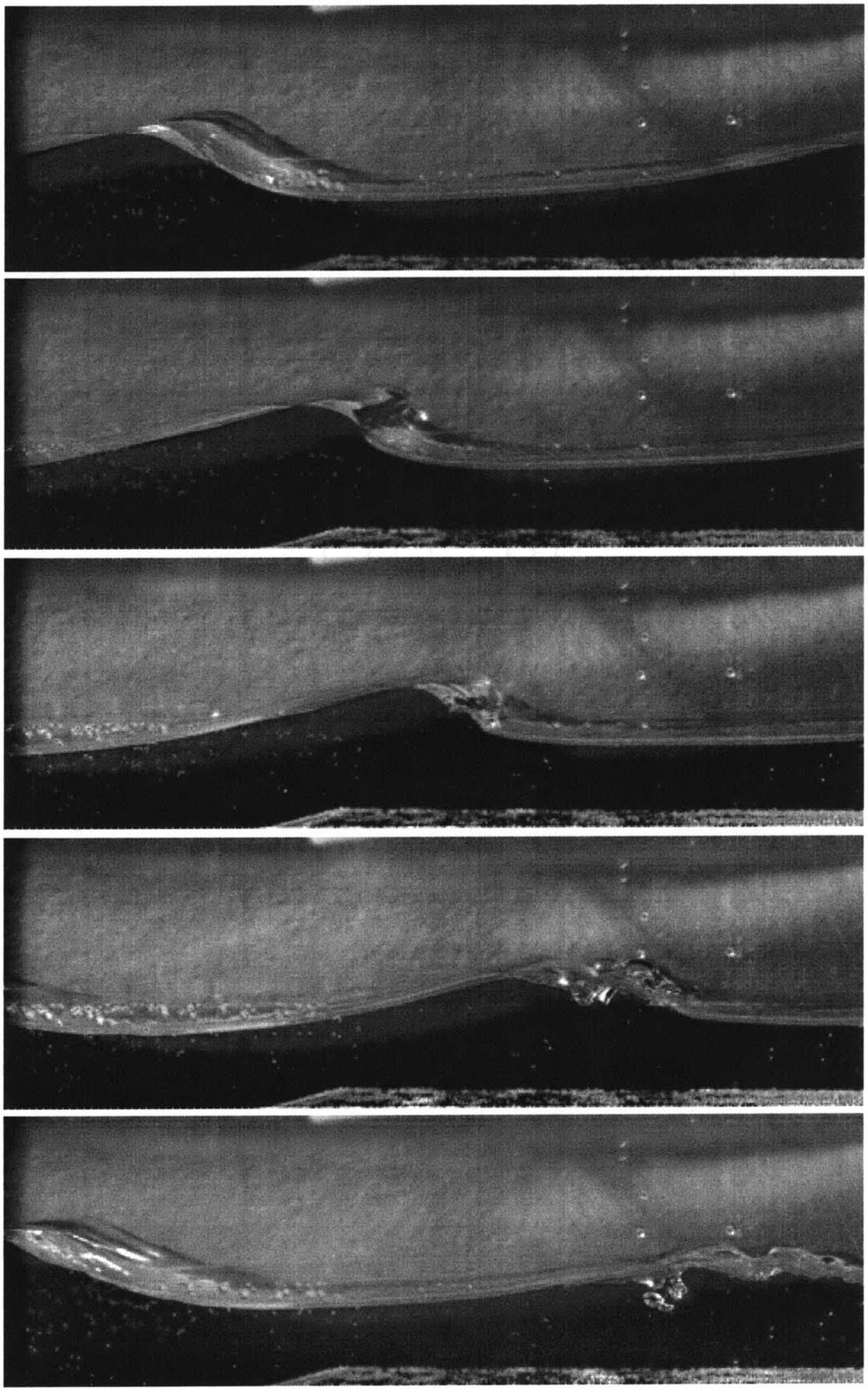

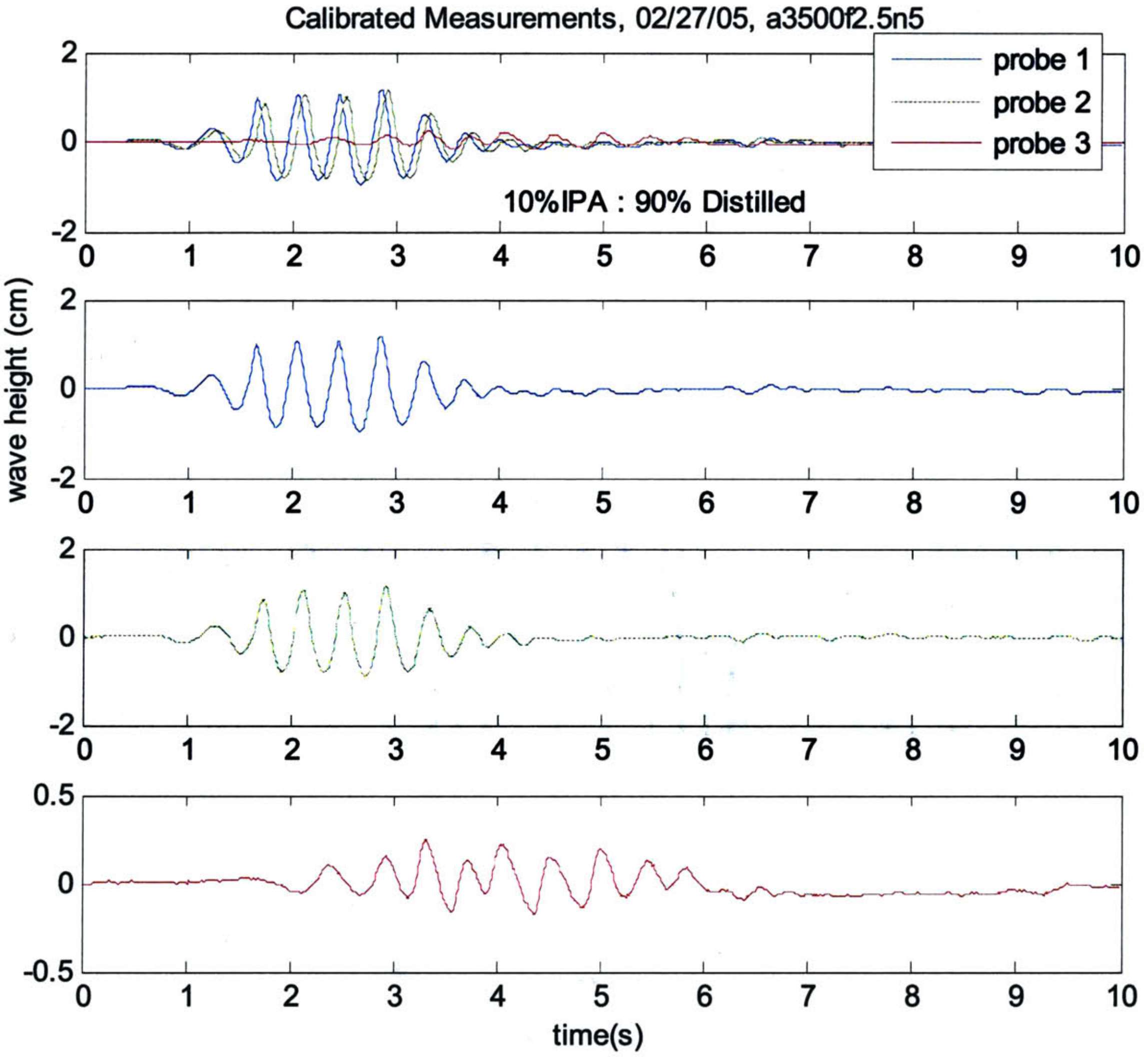

freq. (Hz)	Upstream amp. (cm)	Upstream ak	Dwnstrm amp. (cm)	Energy Remaining Dwnstrm	WE	RE	lambda (cm)	meas. Cp (m/s)	Breaking Details
2.5	0.96	0.221	0.19	3.72%	2944	1.79E+05	27.4	0.68478	plunging

Figure 4-16: Image frames (left page), probe data (top right), and wave kinematic (bottom right) parameters for the 2.5 Hz frequency case generated in five wave paddle cycles. The paddle amplitude was 1.75 cm.

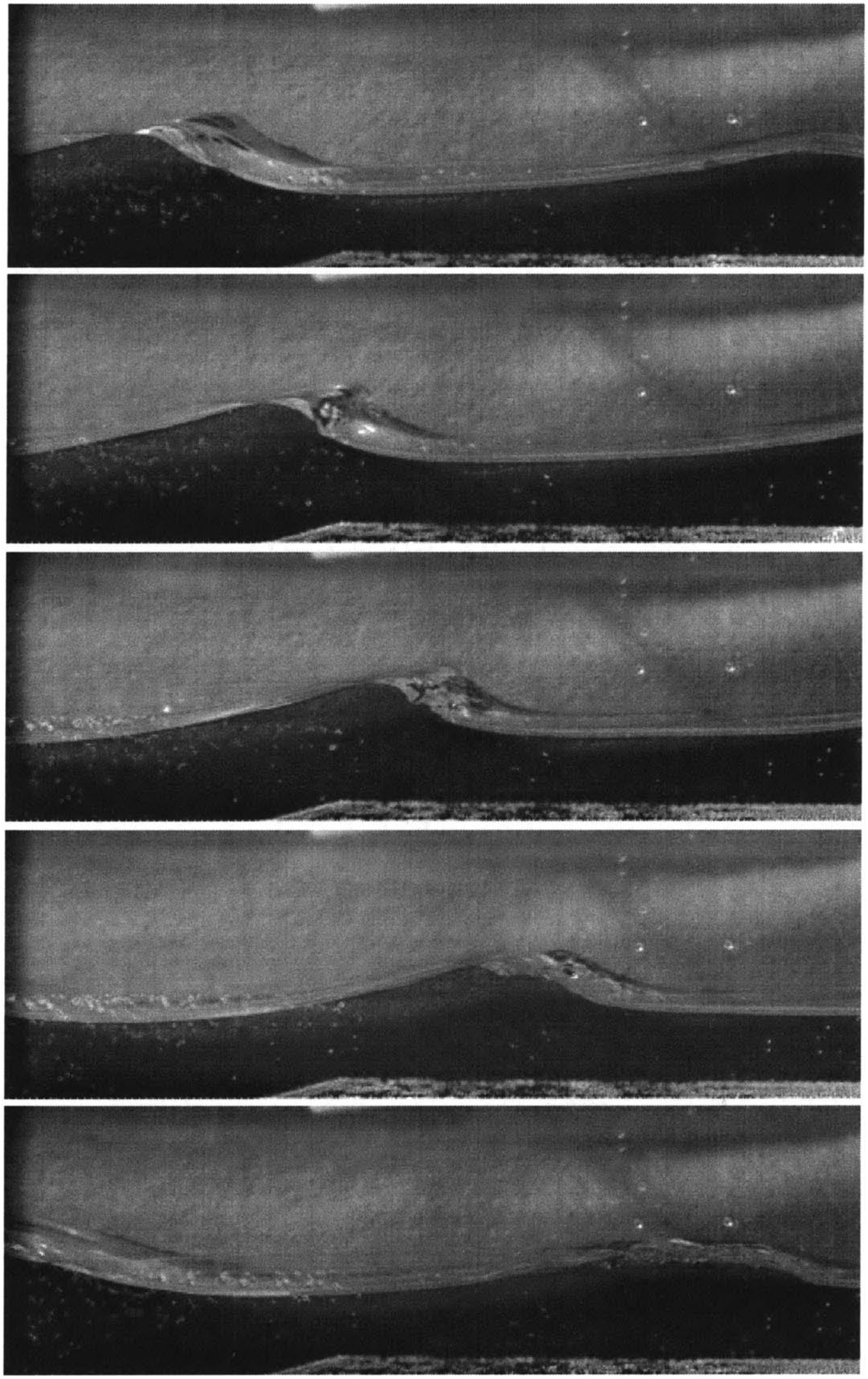

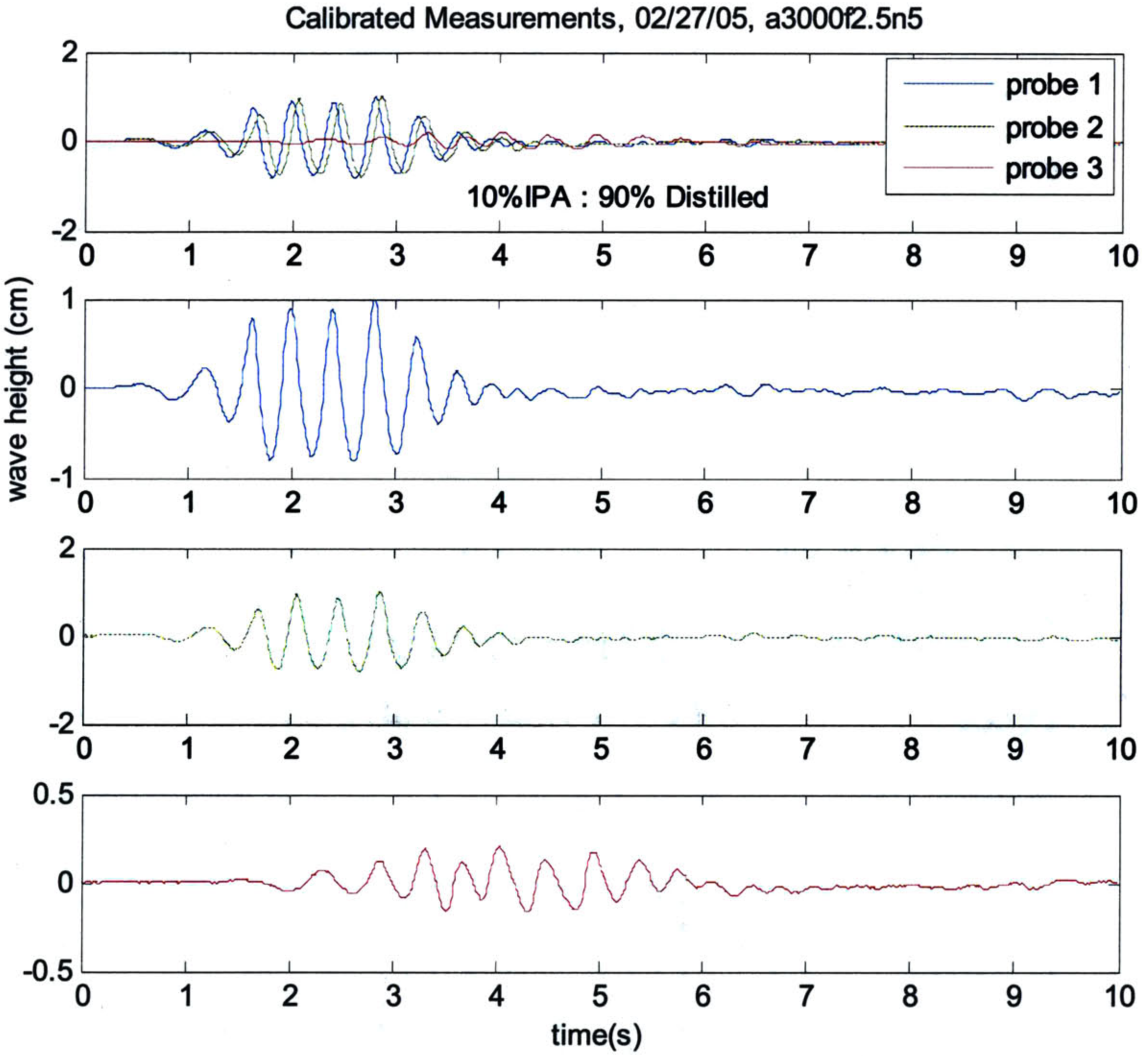

freq. (Hz)	Upstream amp. (cm)	Upstream ak	Dwnstrm amp. (cm)	Energy Remaining Dwnstrm	WE	RE	lambda (cm)	meas. Cp (m/s)	Breaking Details
2.5	0.84	0.206	0.16	3.57%	2436	1.58E+05	25.7	0.64286	spilling

Figure 4-17: Image frames (left page), probe data (top right), and wave kinematic (bottom right) parameters for the 2.5 Hz frequency case generated in five wave paddle cycles. The paddle amplitude was 1.5 cm.

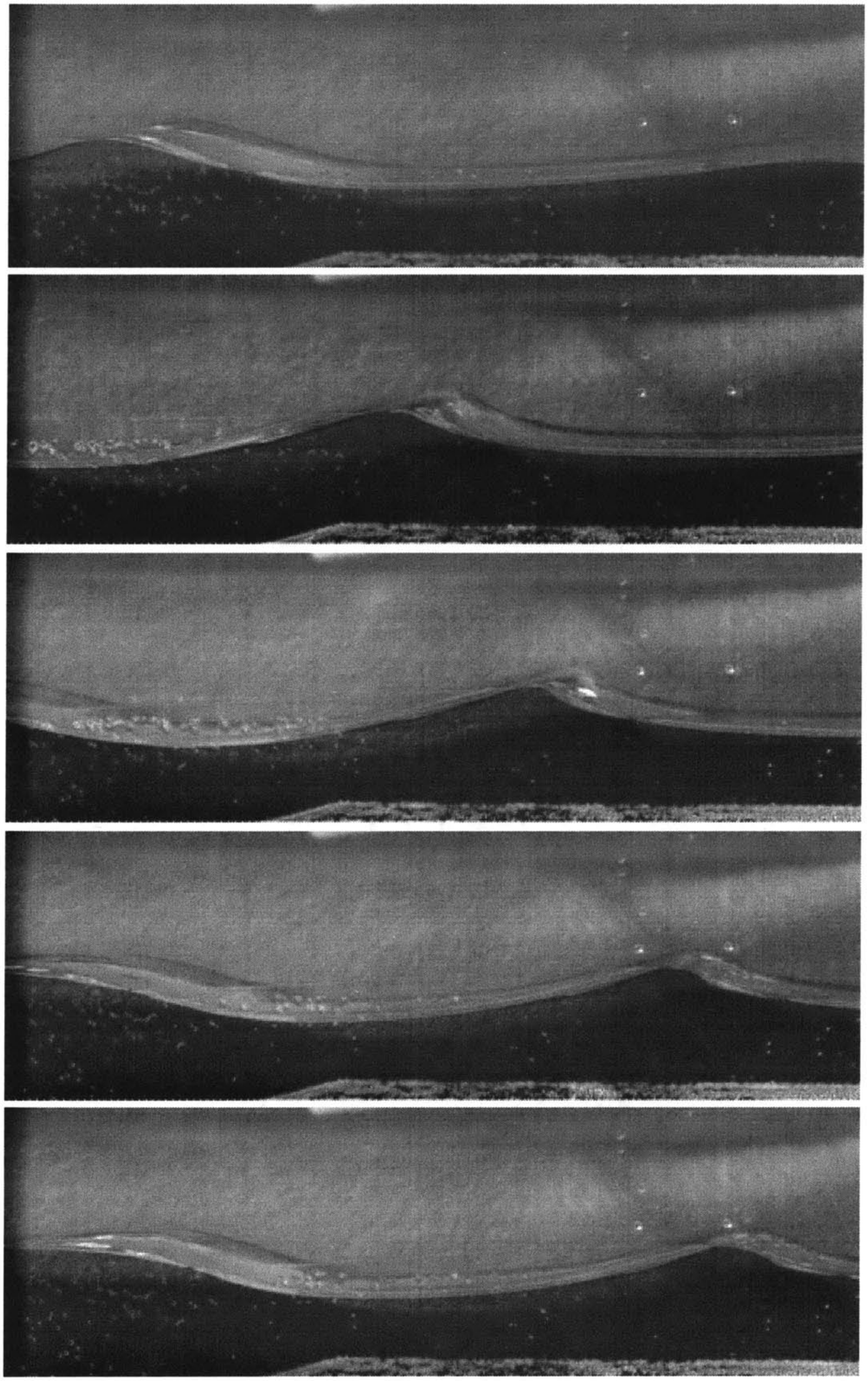

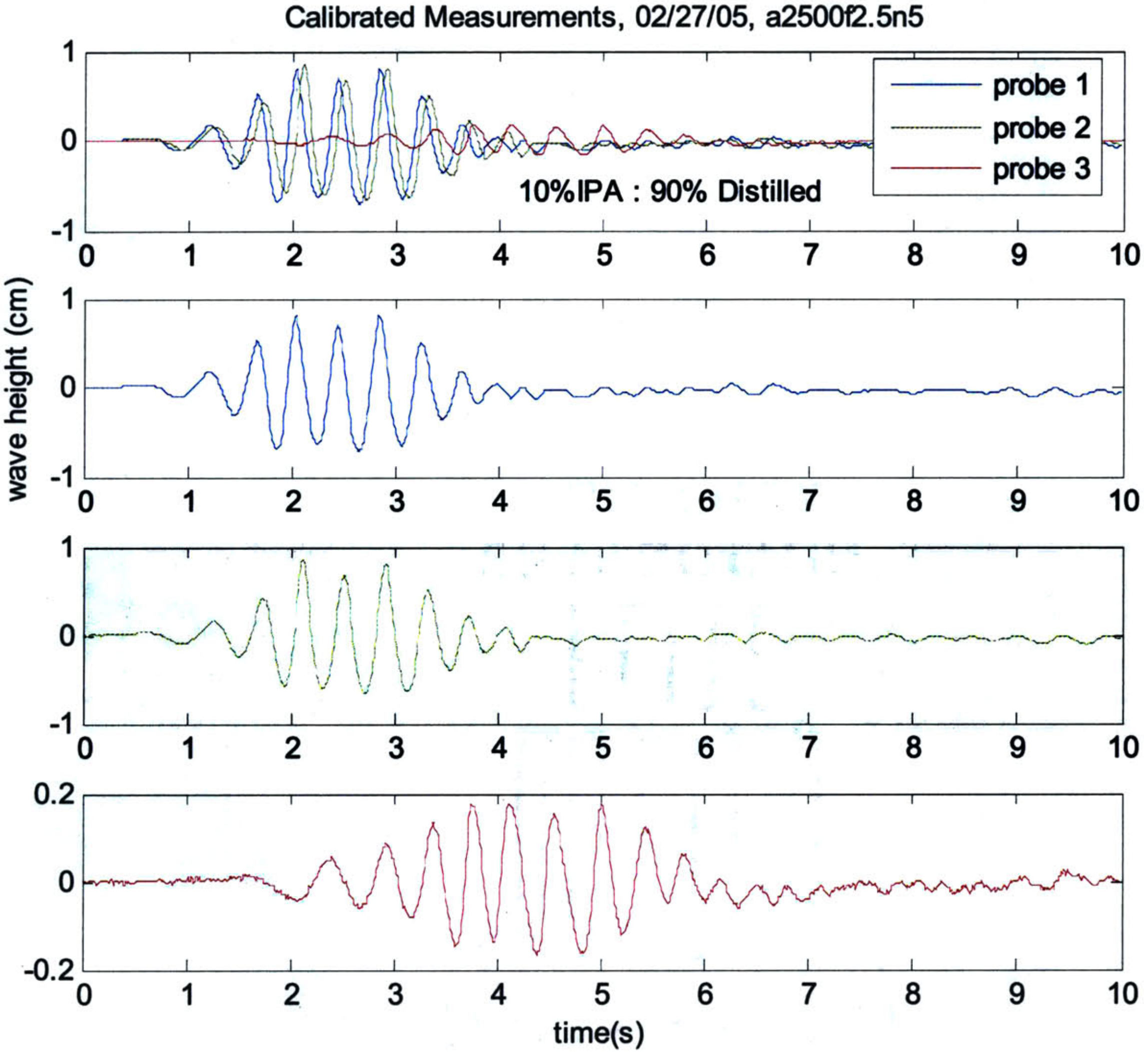

freq. (Hz)	Upstream amp. (cm)	Upstream ak	Dwnstrm amp. (cm)	Energy Remaining Dwnstrm	WE	RE	lambda (cm)	meas. Cp (m/s)	Breaking Details
2.5	0.73	0.171	0.16	4.76%	2760	1.72E+05	26.8	0.67021	spilling

Figure 4-18: Image frames (left page), probe data (top right), and wave kinematic (bottom right) parameters for the 2.5 Hz frequency case generated in five wave paddle cycles. The paddle amplitude was 1.25 cm.

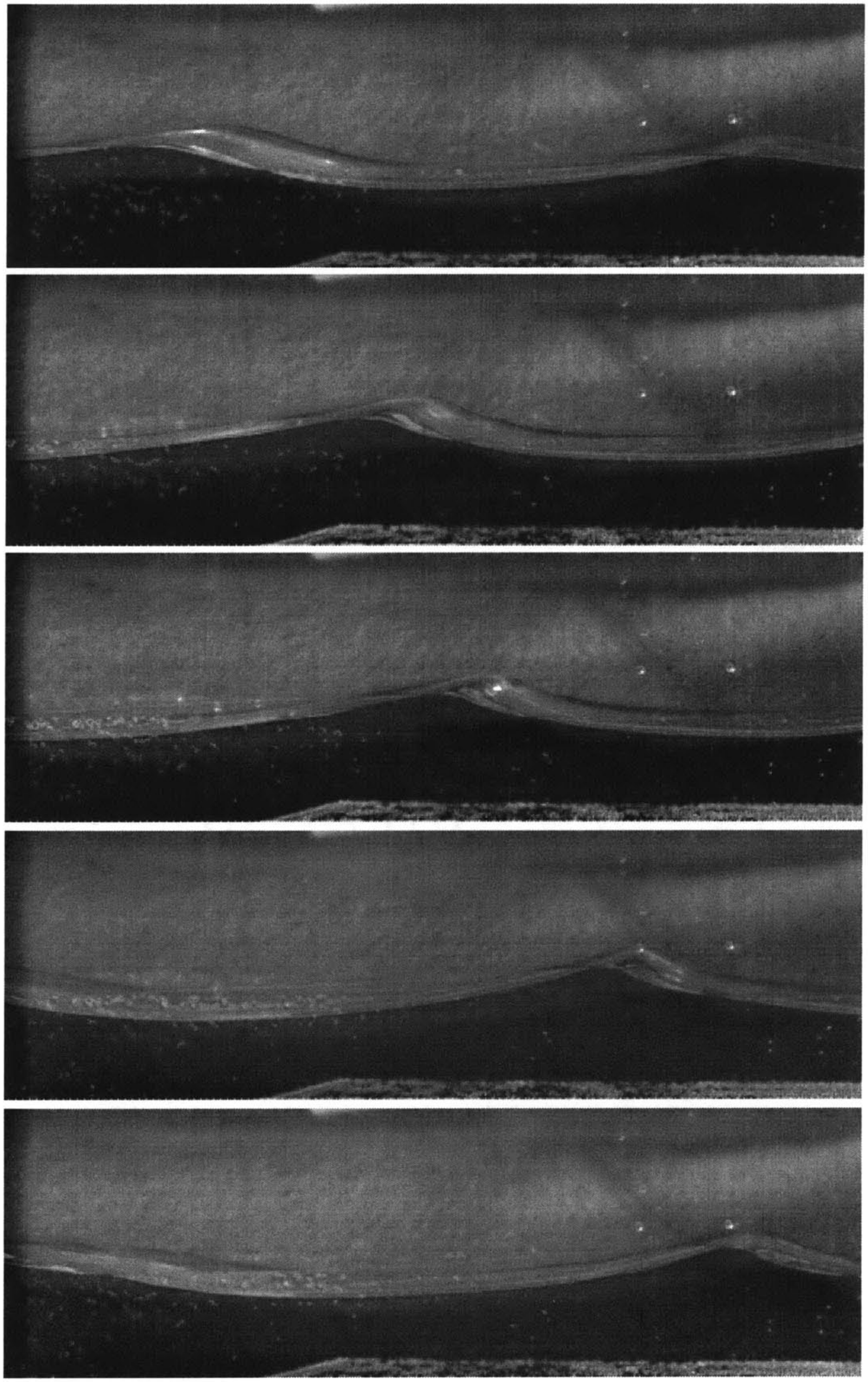

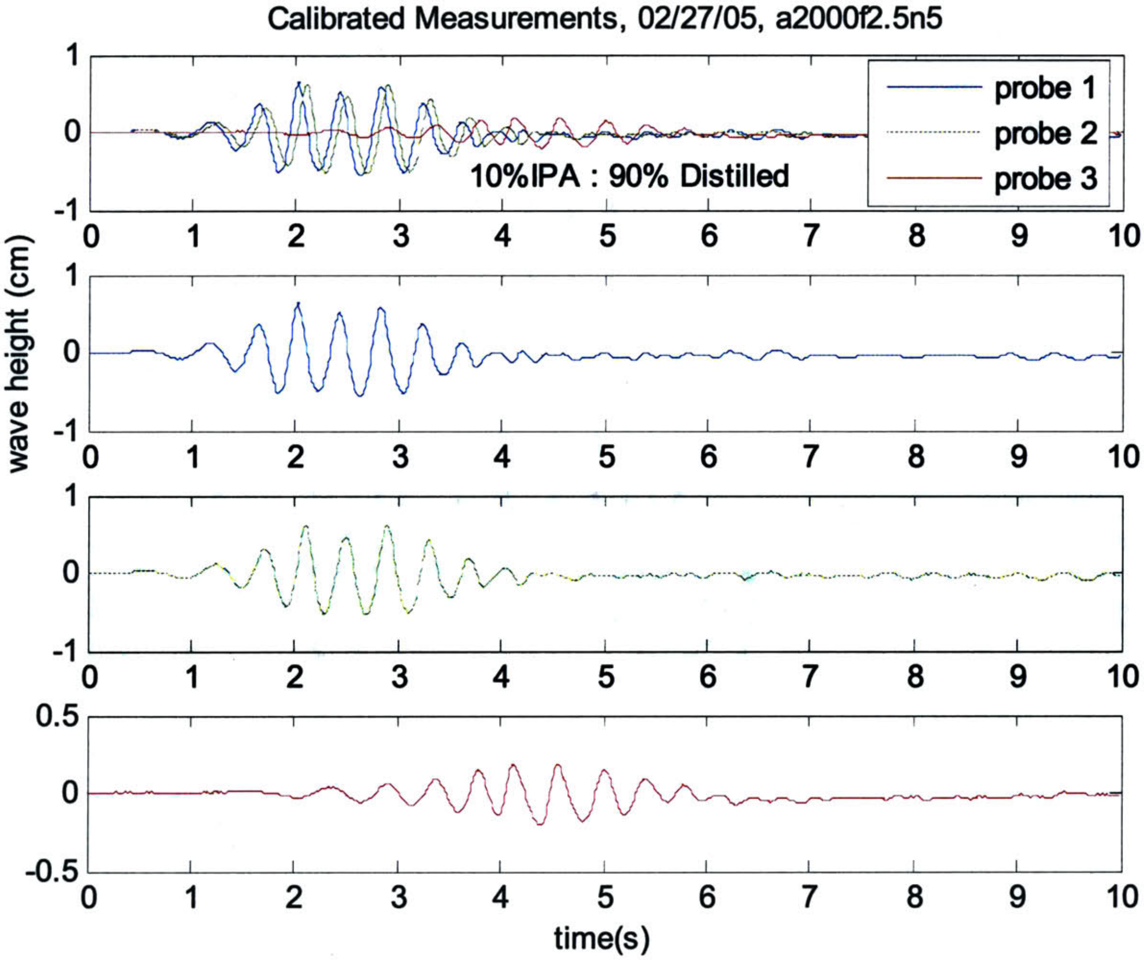

freq. (Hz)	Upstream amp. (cm)	Upstream ak	Dwnstrm amp. (cm)	Energy Remaining Dwnstrm	WE	RE	lambda (cm)	meas. Cp (m/s)	Breaking Details
2.5	0.57	0.142	0.14	6.22%	2292	1.52E+05	25.2	0.63	spilling

Figure 4-19: Image frames (left page), probe data (top right), and wave kinematic (bottom right) parameters for the 2.5 Hz frequency case generated in five wave paddle cycles. The paddle amplitude was 1.0 cm.

This page intentionally left blank.

4.3.4 Wave Frequency: 3 Hz

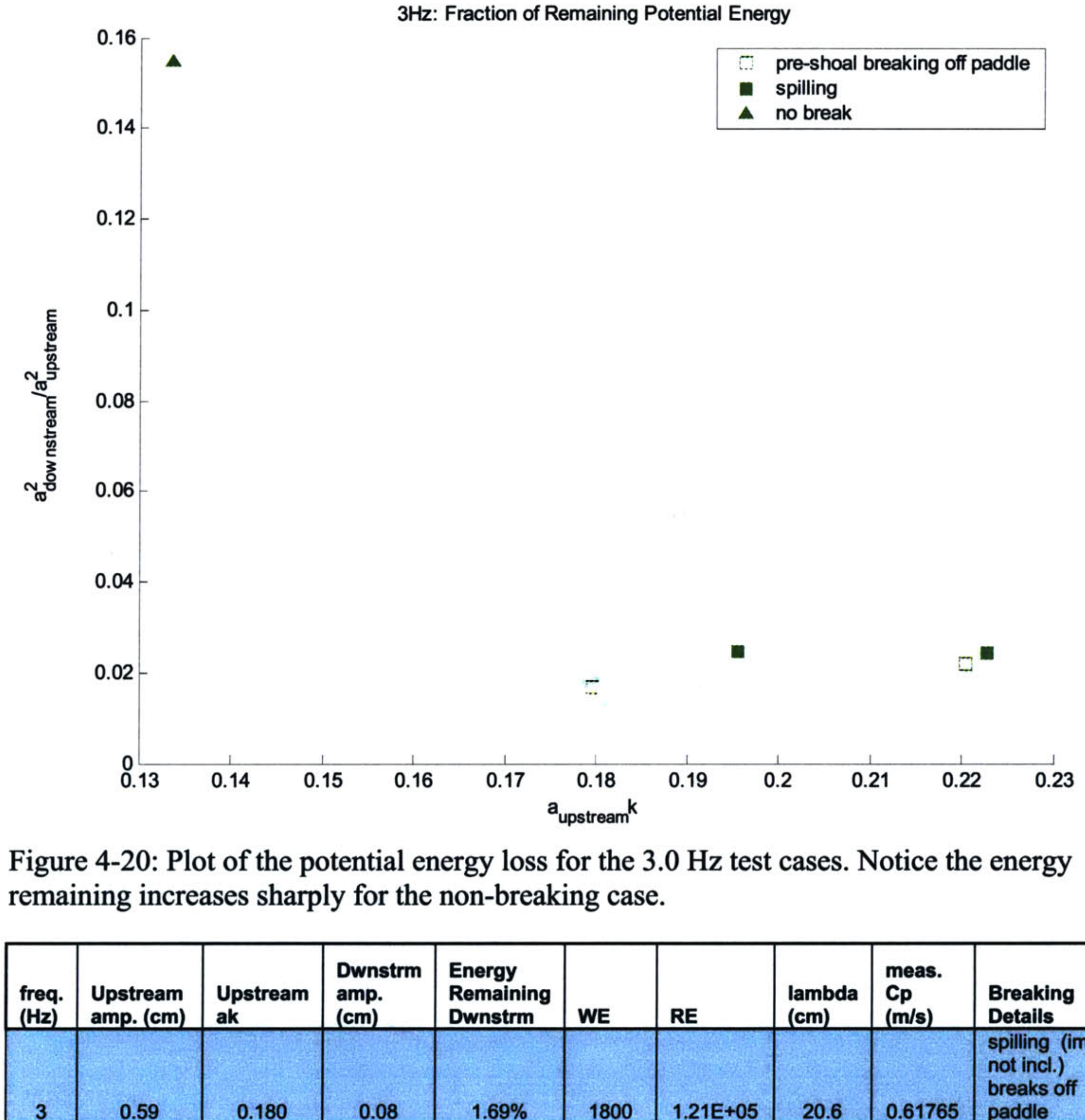

Figure 4-20: Plot of the potential energy loss for the 3.0 Hz test cases. Notice the energy remaining increases sharply for the non-breaking case.

freq. (Hz)	Upstream amp. (cm)	Upstream ak	Dwnstrm amp. (cm)	Energy Remaining Dwnstrm	WE	RE	lambda (cm)	meas. Cp (m/s)	Breaking Details
3	0.59	0.180	0.08	1.69%	1800	1.21E+05	20.6	0.61765	spilling (img. not incl.) breaks off paddle
3	0.65	0.221	0.10	2.18%	1289	9.72E+04	18.4	0.55263	spilling (img. not incl.) breaks off paddle
3	0.70	0.223	0.11	2.43%	1604	1.12E+05	19.8	0.59434	spilling
3	0.55	0.196	0.09	2.46%	1163	9.07E+04	17.8	0.5339	spilling
3	0.36	0.134	0.14	15.47%	1002	8.22E+04	16.9	0.50806	no break (imgs not incl.)

Table 4-4: Summary of parameters and results for all 3 Hz test cases.

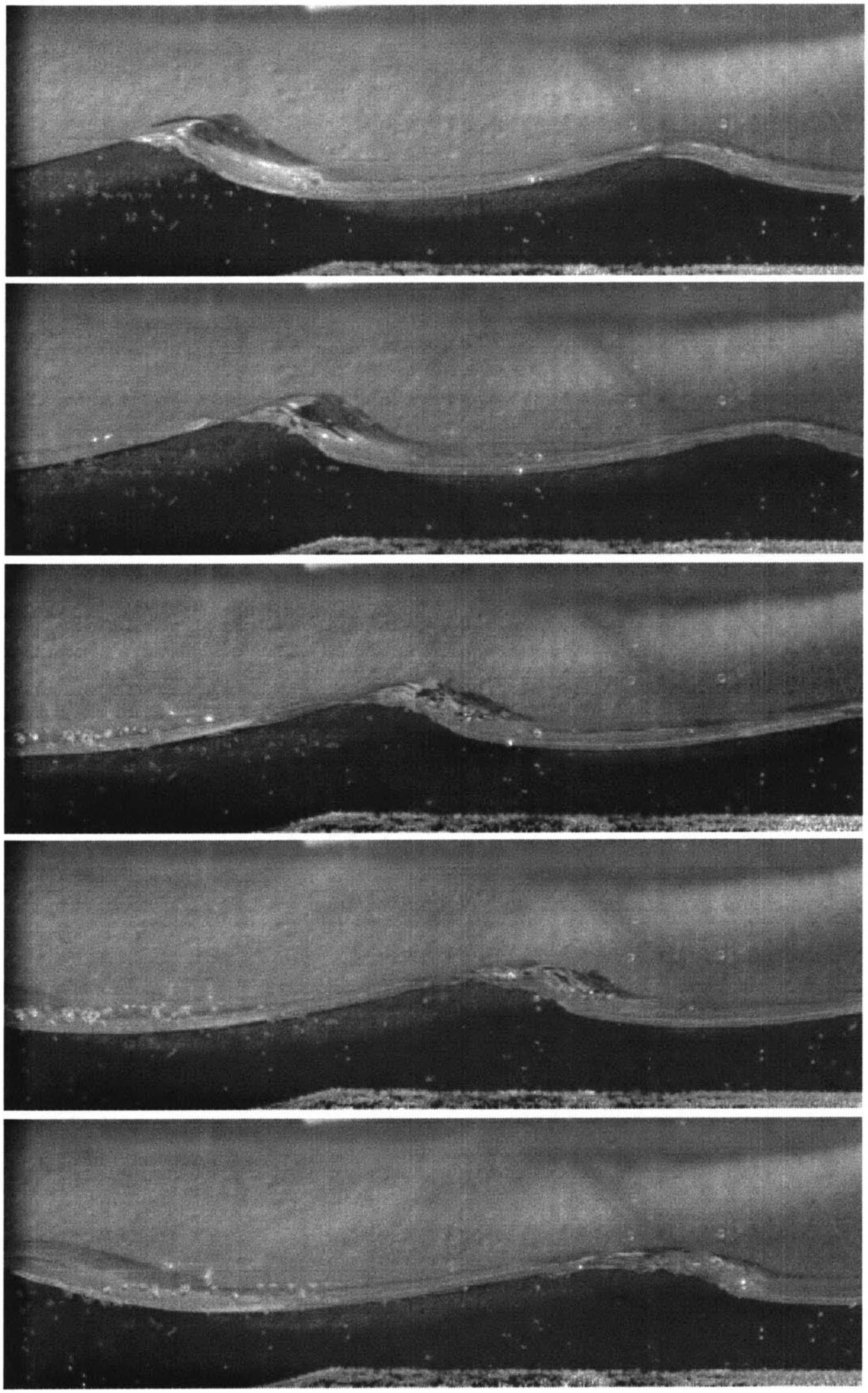

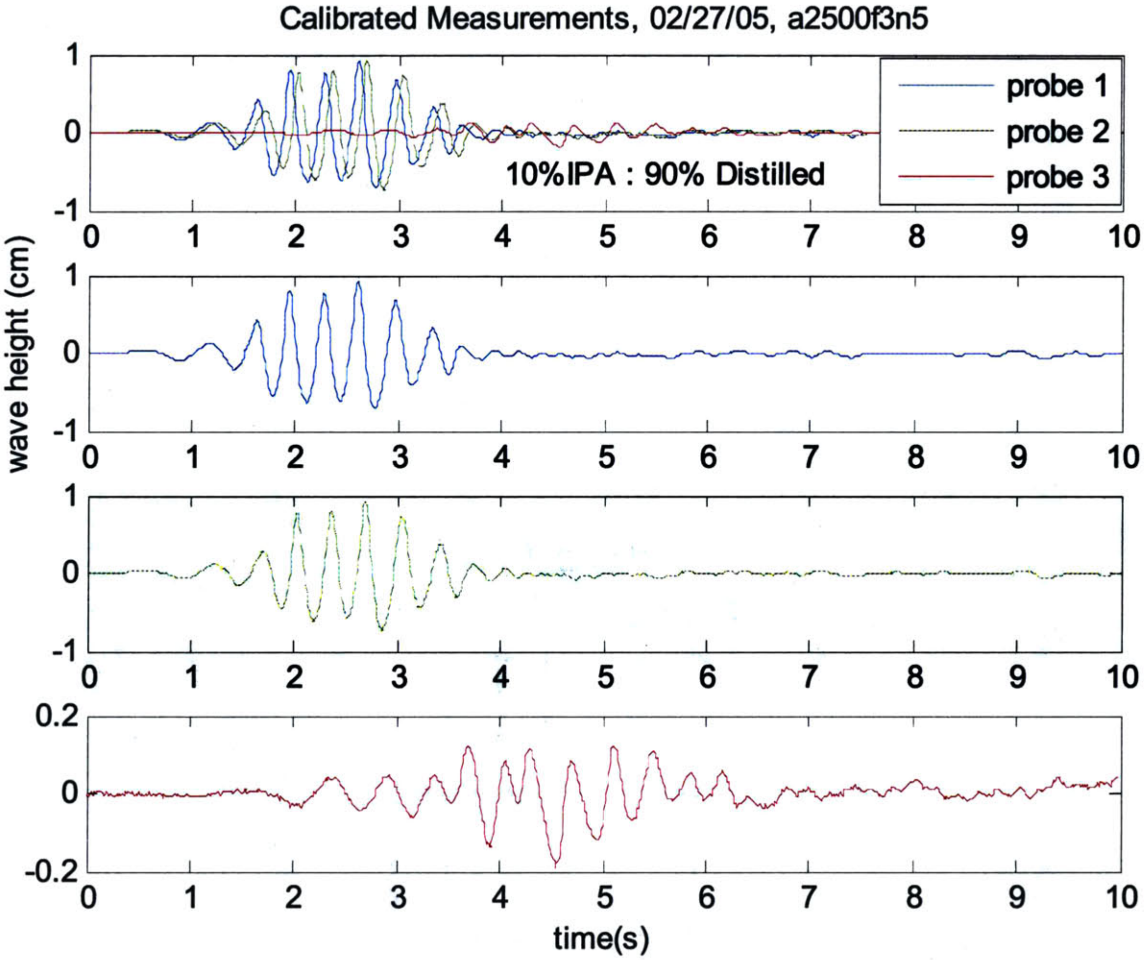

freq. (Hz)	Upstream amp. (cm)	Upstream ak	Dwnstrm amp. (cm)	Energy Remaining Dwnstrm	WE	RE	lambda (cm)	meas. Cp (m/s)	Breaking Details
3	0.70	0.223	0.11	2.43%	1604	1.12E+05	19.8	0.59434	spilling

Figure 4-21: Image frames (left page), probe data (top right), and wave kinematic (bottom right) parameters for the 3.0 Hz frequency case generated in five wave paddle cycles. The paddle amplitude was 1.25 cm.

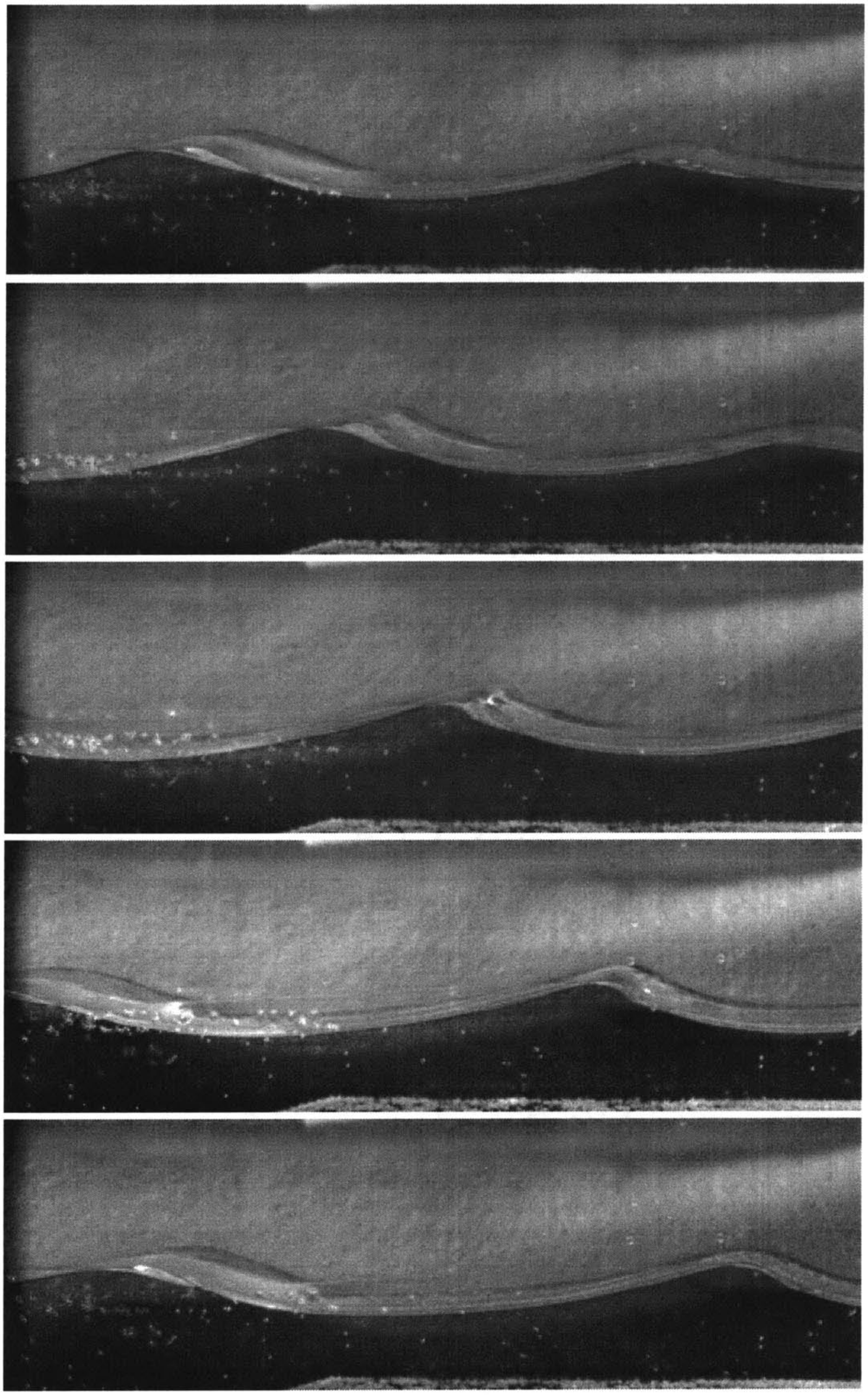

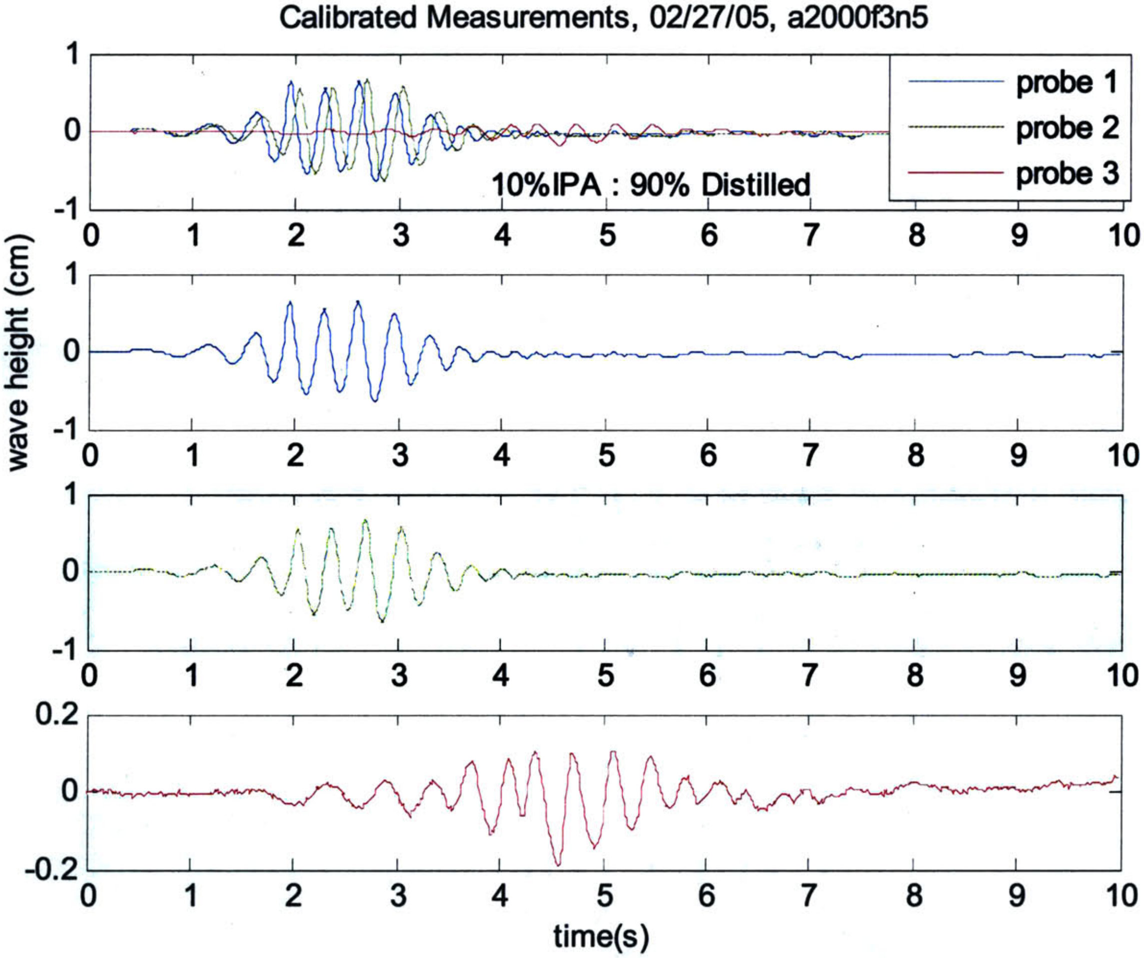

freq. (Hz)	Upstream amp. (cm)	Upstream ak	Dwnstrm amp. (cm)	Energy Remaining Dwnstrm	WE	RE	lambda (cm)	meas. Cp (m/s)	Breaking Details
3	0.55	0.196	0.09	2.46%	1163	9.07E+04	17.8	0.5339	spilling

Figure 4-22: Image frames (left page), probe data (top right), and wave kinematic (bottom right) parameters for the 3.0 Hz frequency case generated in five wave paddle cycles. The paddle amplitude was 1.0 cm.

This page intentionally left blank.

4.3.5 Wave Frequency: 3.5 Hz

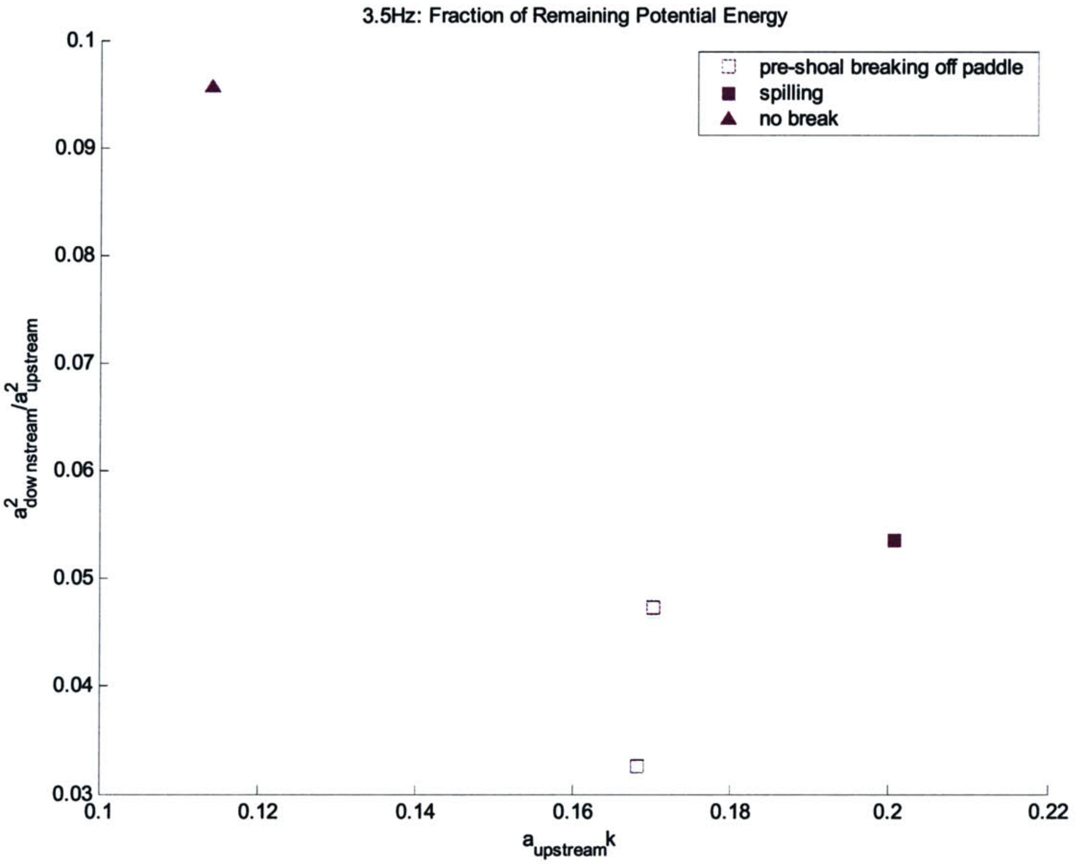

Figure 4-23: Plot of the potential energy loss for the 3.5 Hz test cases. Notice the energy remaining increases sharply for the non-breaking case.

freq. (Hz)	Upstream amp. (cm)	Upstream ak	Dwnstrm amp. (cm)	Energy Remaining Dwnstrm	WE	RE	lambda (cm)	meas. Cp (m/s)	Breaking Details
3.5	0.38	0.170	0.08	4.73%	745	6.41E+04	13.8	0.48462	spilling breaks off paddle
3.5	0.37	0.168	0.07	3.26%	712	6.21E+04	13.6	0.47727	spilling breaks off paddle
3.5	0.42	0.201	0.10	5.36%	623	5.69E+04	13.0	0.45652	spilling
3.5	0.23	0.114	0.07	9.56%	572	5.37E+04	12.7	0.44366	no break

Table 4-5: Summary of parameters and results for all 3.5 Hz test cases.

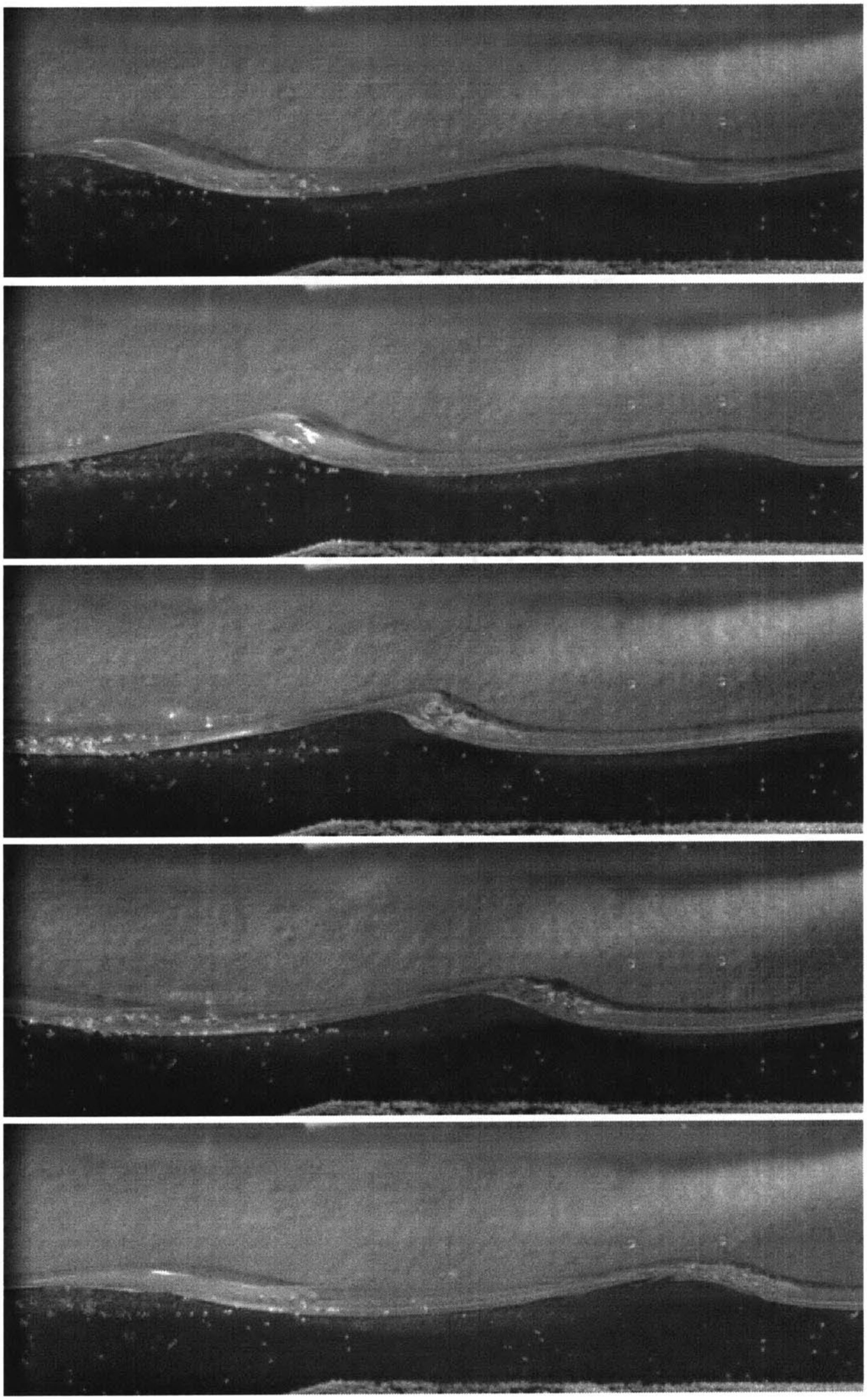

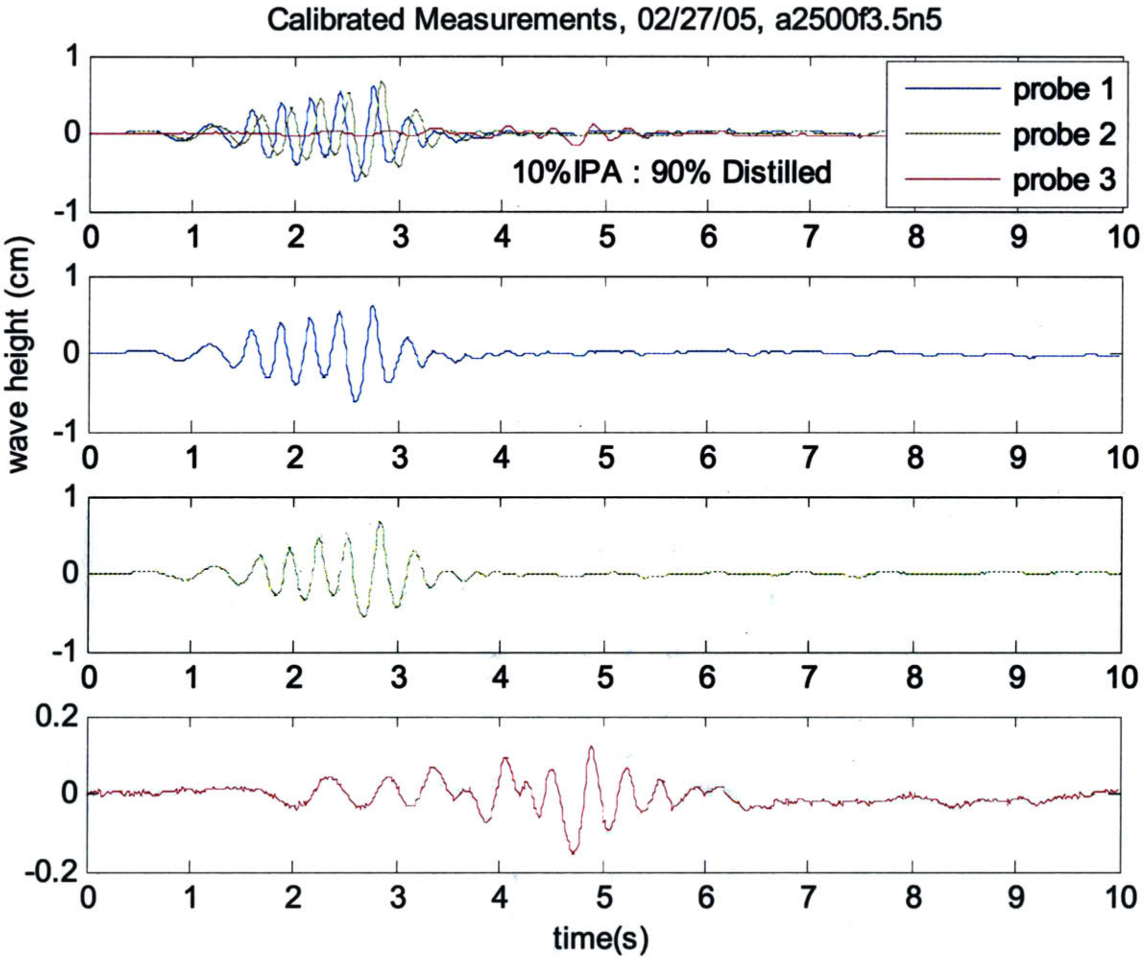

freq. (Hz)	Upstream amp. (cm)	Upstream ak	Dwnstrm amp. (cm)	Energy Remaining Dwnstrm	WE	RE	lambda (cm)	meas. Cp (m/s)	Breaking Details
3.5	0.38	0.170	0.08	4.73%	745	6.41E+04	13.8	0.48462	spilling breaks off paddle

Figure 4-24: Image frames (left page), probe data (top right), and wave kinematic (bottom right) parameters for the 3.5 Hz frequency case generated in five wave paddle cycles. The paddle amplitude was 1.25 cm.

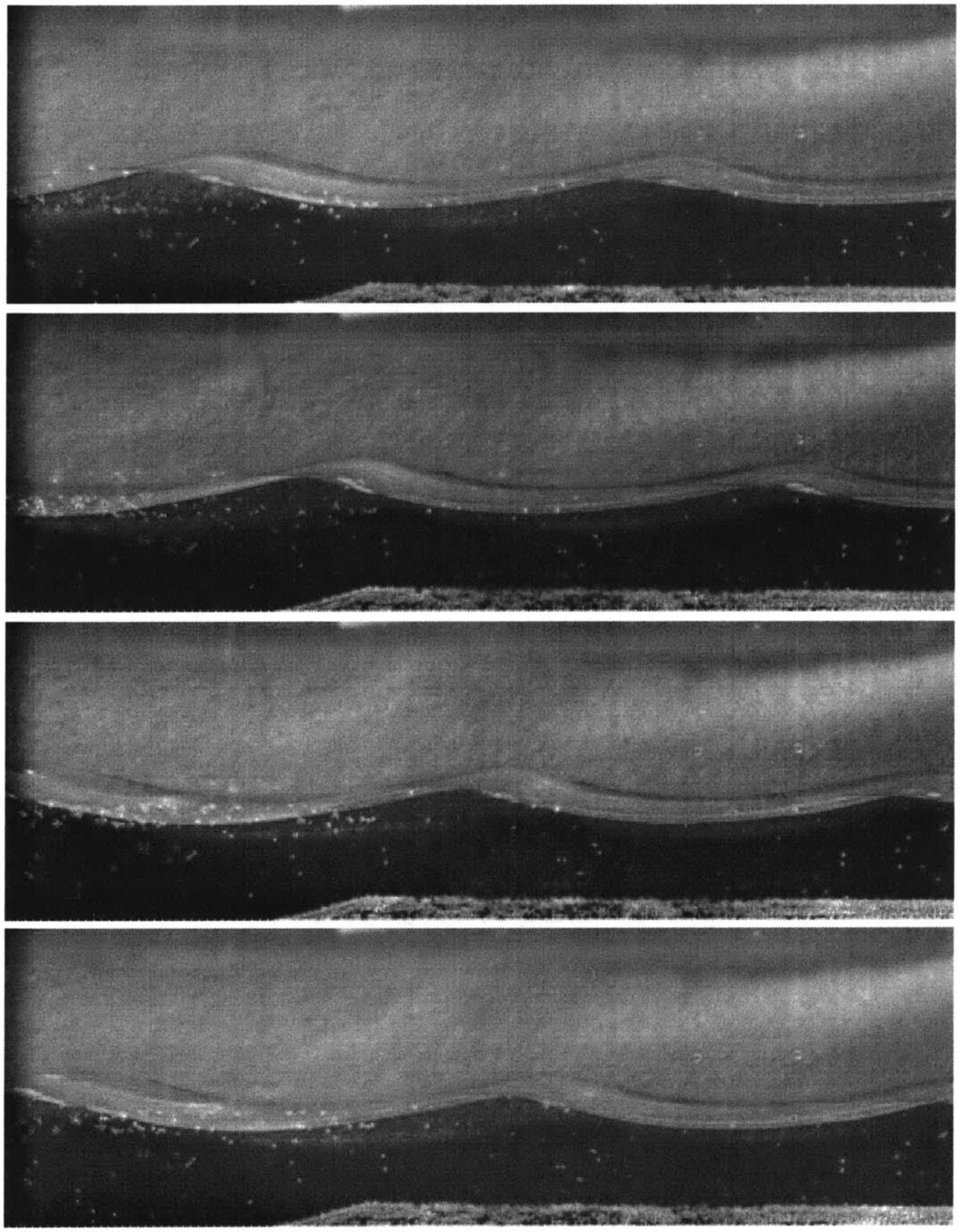

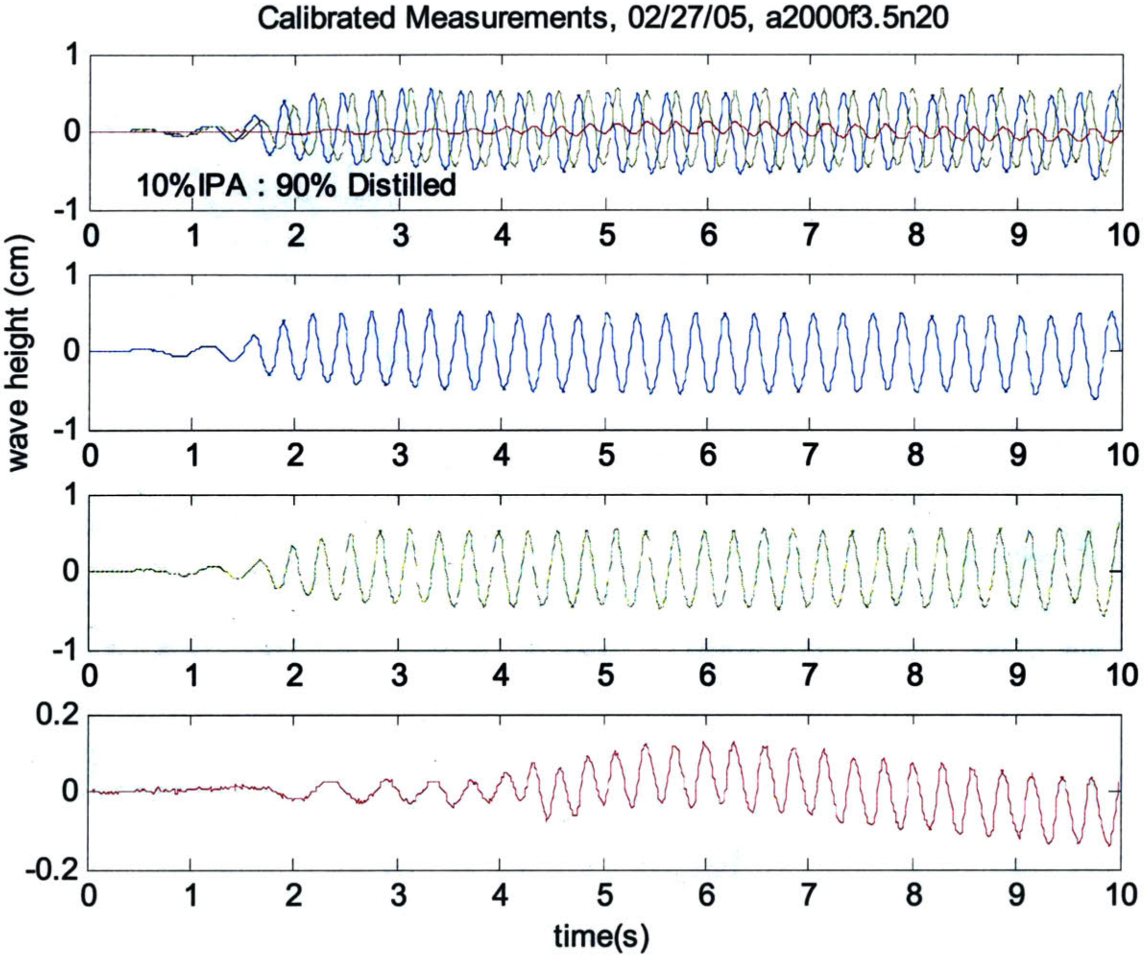

freq. (Hz)	Upstream amp. (cm)	Upstream ak	Dwnstrm amp. (cm)	Energy Remaining Dwnstrm	WE	RE	lambda (cm)	meas. Cp (m/s)	Breaking Details
3.5	0.37	0.168	0.07	3.26%	712	6.21E+04	13.6	0.47727	spilling breaks off paddle

Figure 4-25: Image frames, probe data, and relevant parameters for this 20 paddle cycle, 3.5Hz case. The paddle amplitude was 1 cm, and this run was also used to test the change in amplitude over a long train of waves.

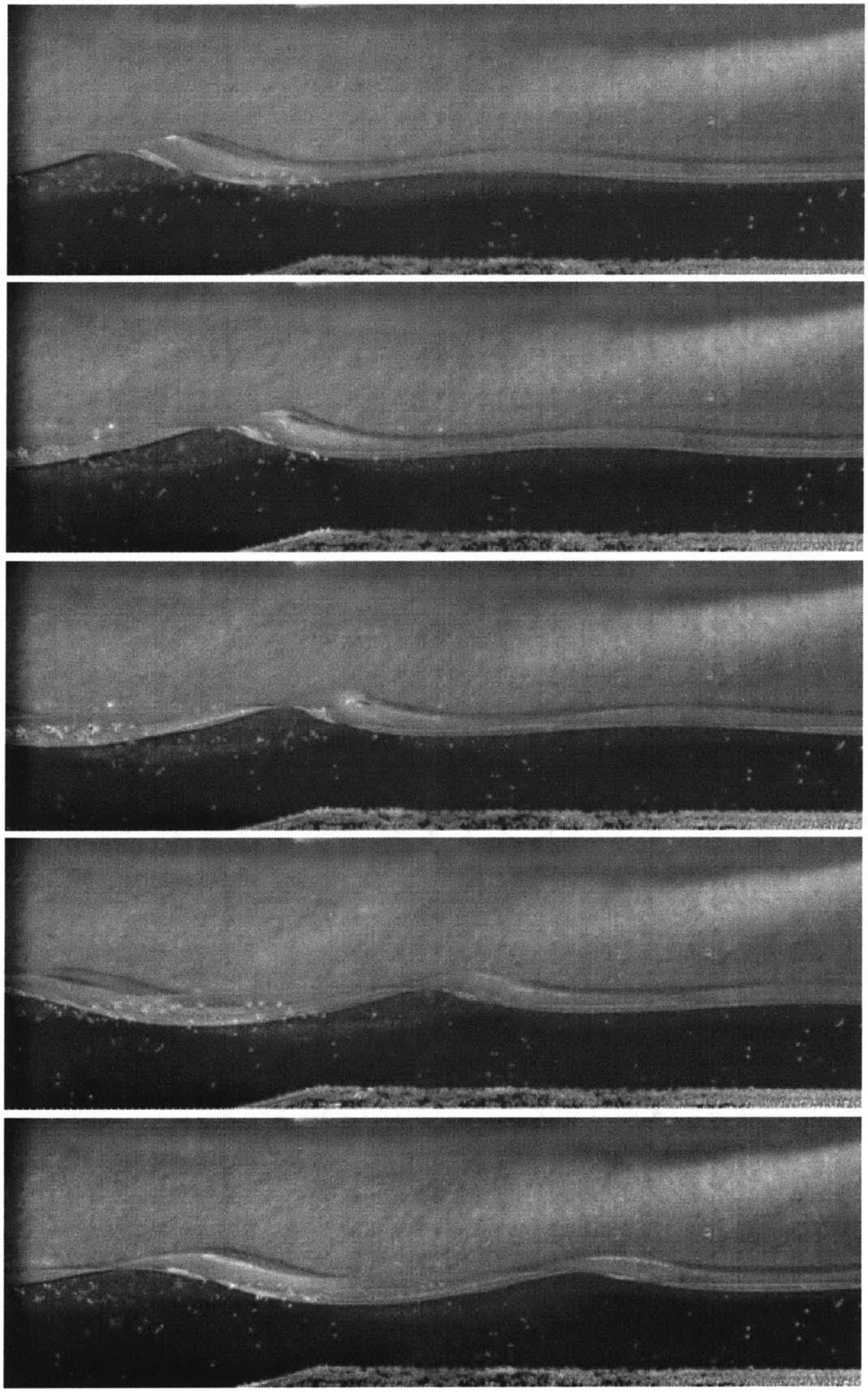

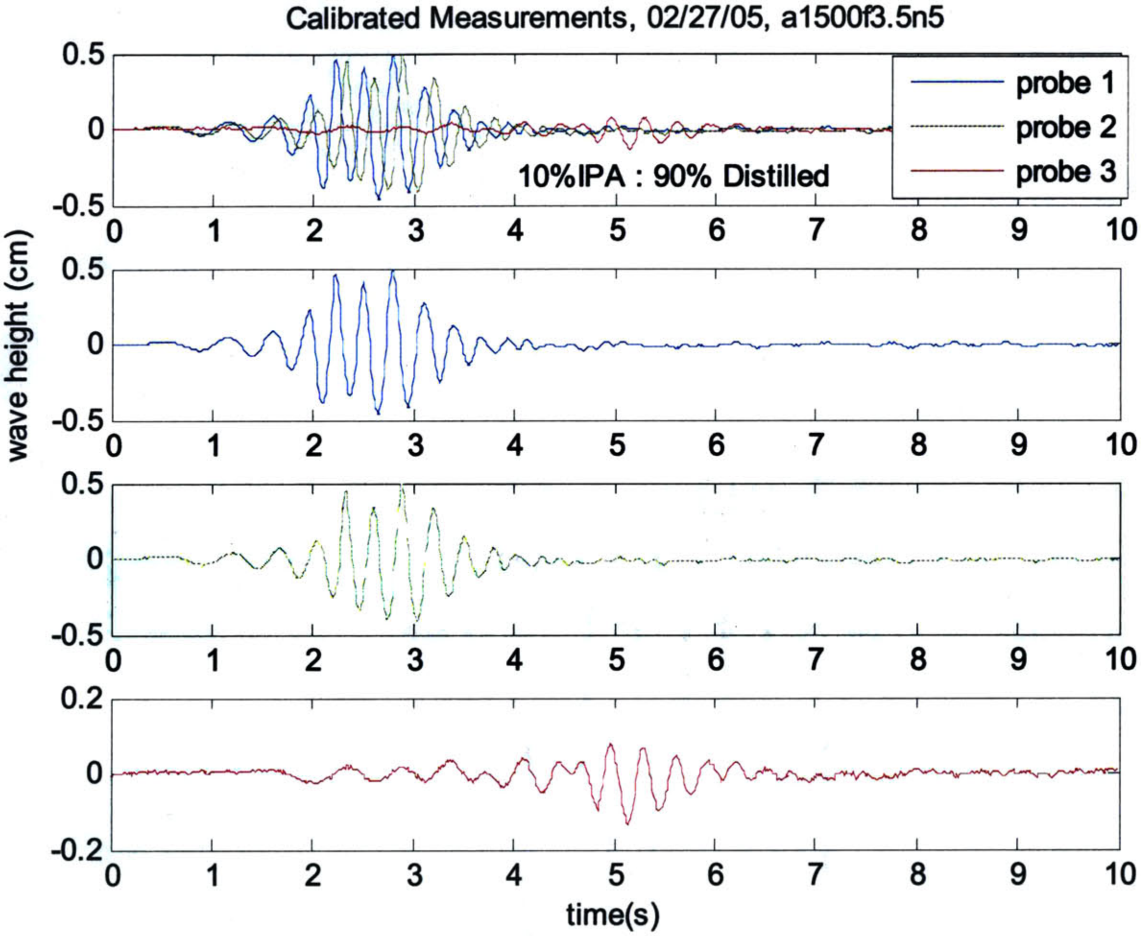

freq. (Hz)	Upstream amp. (cm)	Upstream ak	Dwnstrm amp. (cm)	Energy Remaining Dwnstrm	WE	RE	lambda (cm)	meas. Cp (m/s)	Breaking Details
3.5	0.42	0.201	0.10	5.36%	623	5.69E+04	13.0	0.45652	spilling

Figure 4-26: Image frames (left page), probe data (top right), and wave kinematic (bottom right) parameters for the 3.5 Hz frequency case generated in five wave paddle cycles. The paddle amplitude was 0.75 cm.

This page intentionally left blank.

4.3.6 Wave Frequency: 4 Hz

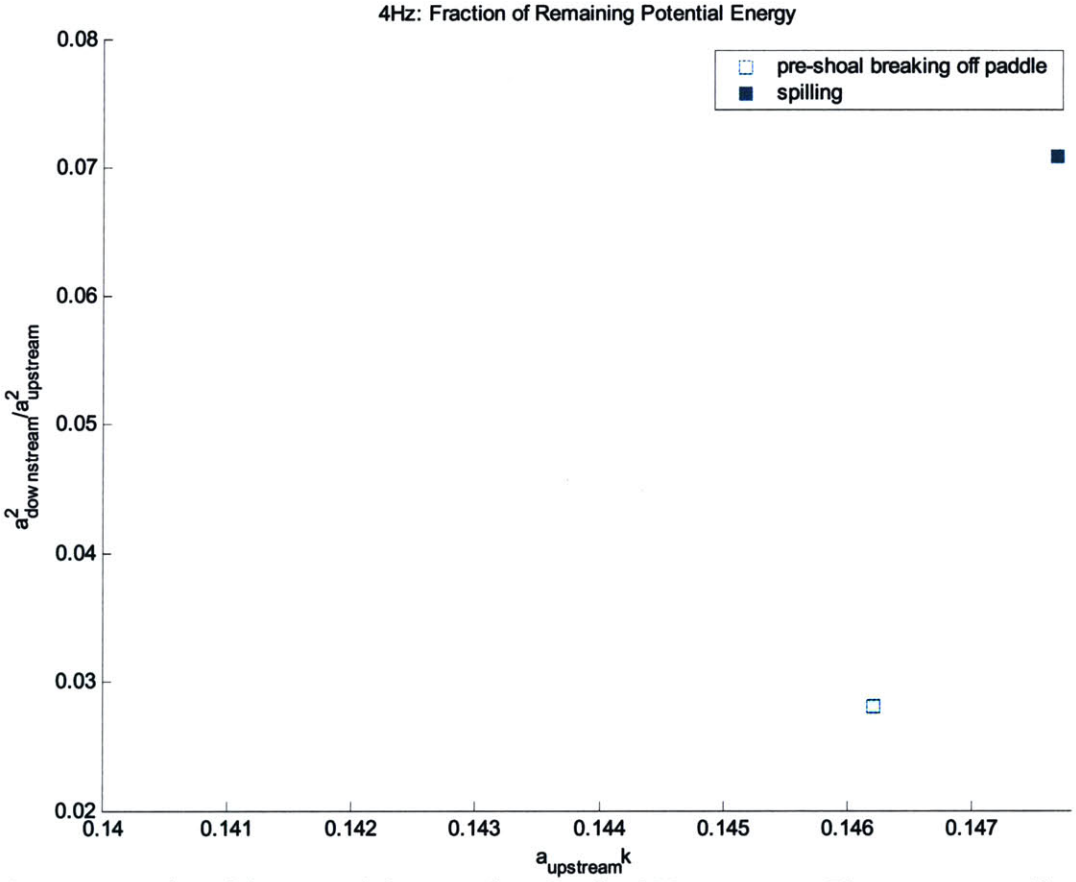

Figure 4-27: Plot of the potential energy loss for the 4 Hz test cases. There was a small range in waves which broke at the shoal without first breaking off the paddle.

freq. (Hz)	Upstream amp. (cm)	Upstream ak	Dwnstrm amp. (cm)	Energy Remaining Dwnstrm	WE	RE	lambda (cm)	meas. Cp (m/s)	Breaking Details
4	0.24	0.146	0.04	2.81%	420	4.18E+04	10.5	0.4186	spilling breaks off paddle
4	0.24	0.148	0.06	7.08%	367	3.82E+04	10.0	0.4	spilling
4	No probe data								no break

Table 4-6: Summary of parameters and results for all 3.5 Hz test cases.

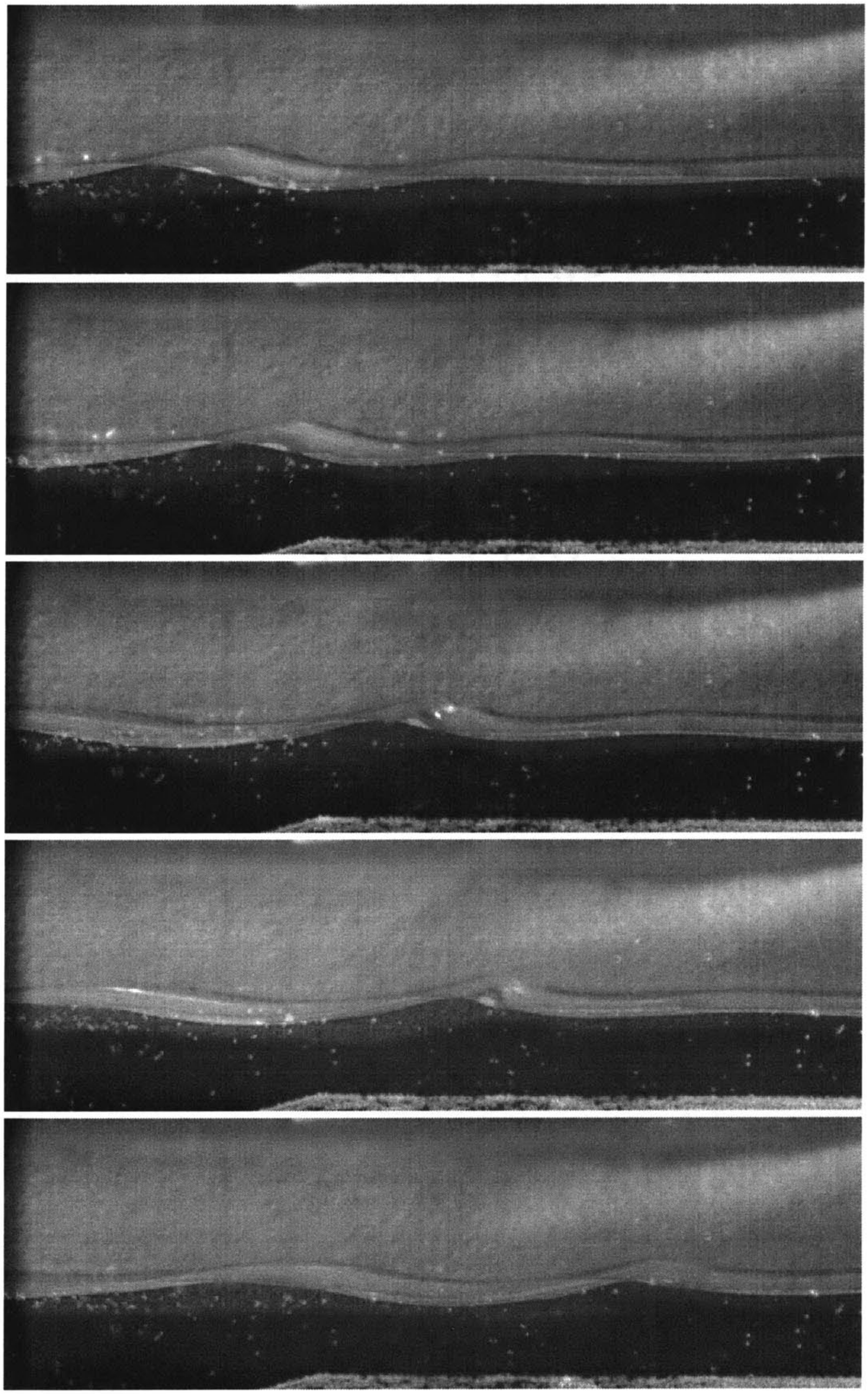

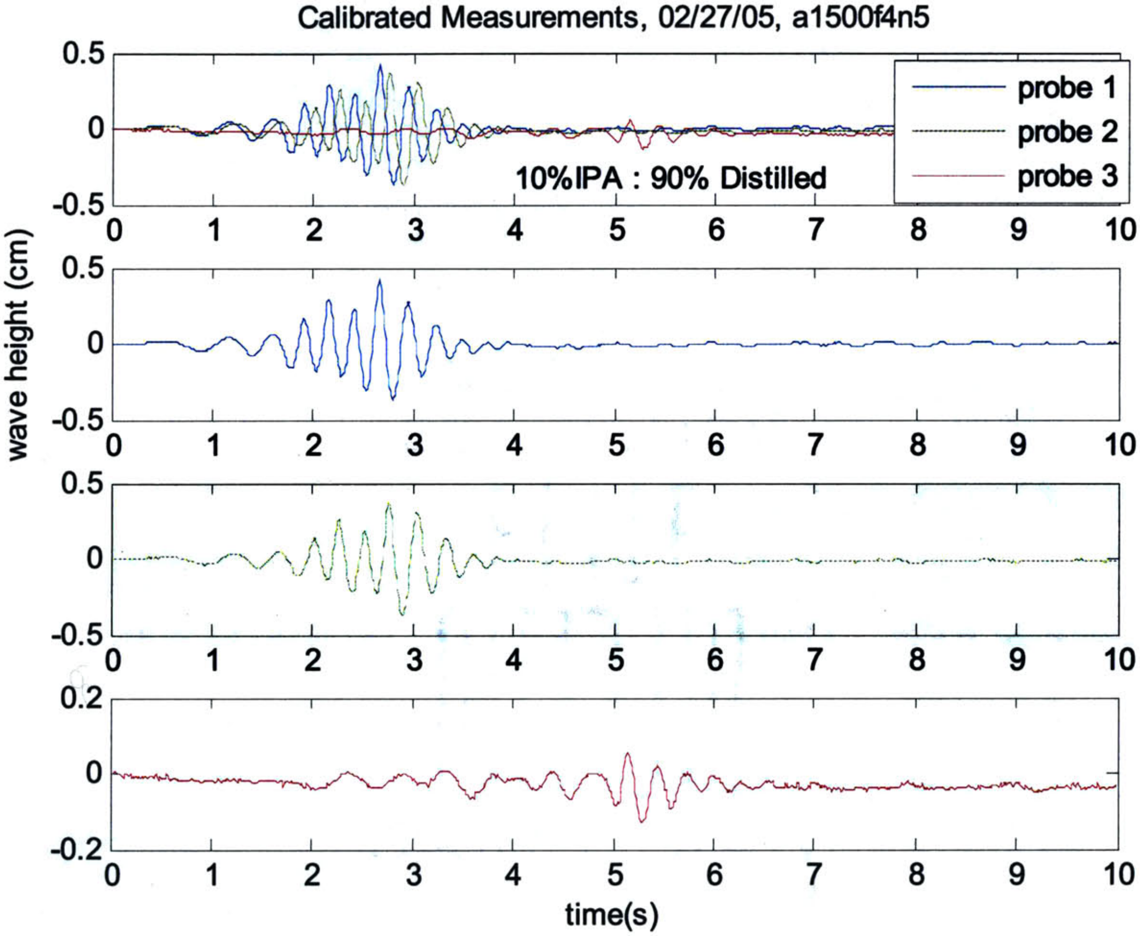

freq. (Hz)	Upstream amp. (cm)	Upstream ak	Dwnstrm amp. (cm)	Energy Remaining Dwnstrm	WE	RE	lambda (cm)	meas. Cp (m/s)	Breaking Details
4	0.24	0.146	0.04	2.81%	420	4.18E+04	10.5	0.4186	spilling breaks off paddle

Figure 4-28: Image frames (left page), probe data (top right), and wave kinematic (bottom right) parameters for the 4.0 Hz frequency case generated in five wave paddle cycles. The paddle amplitude was 0.75 cm.

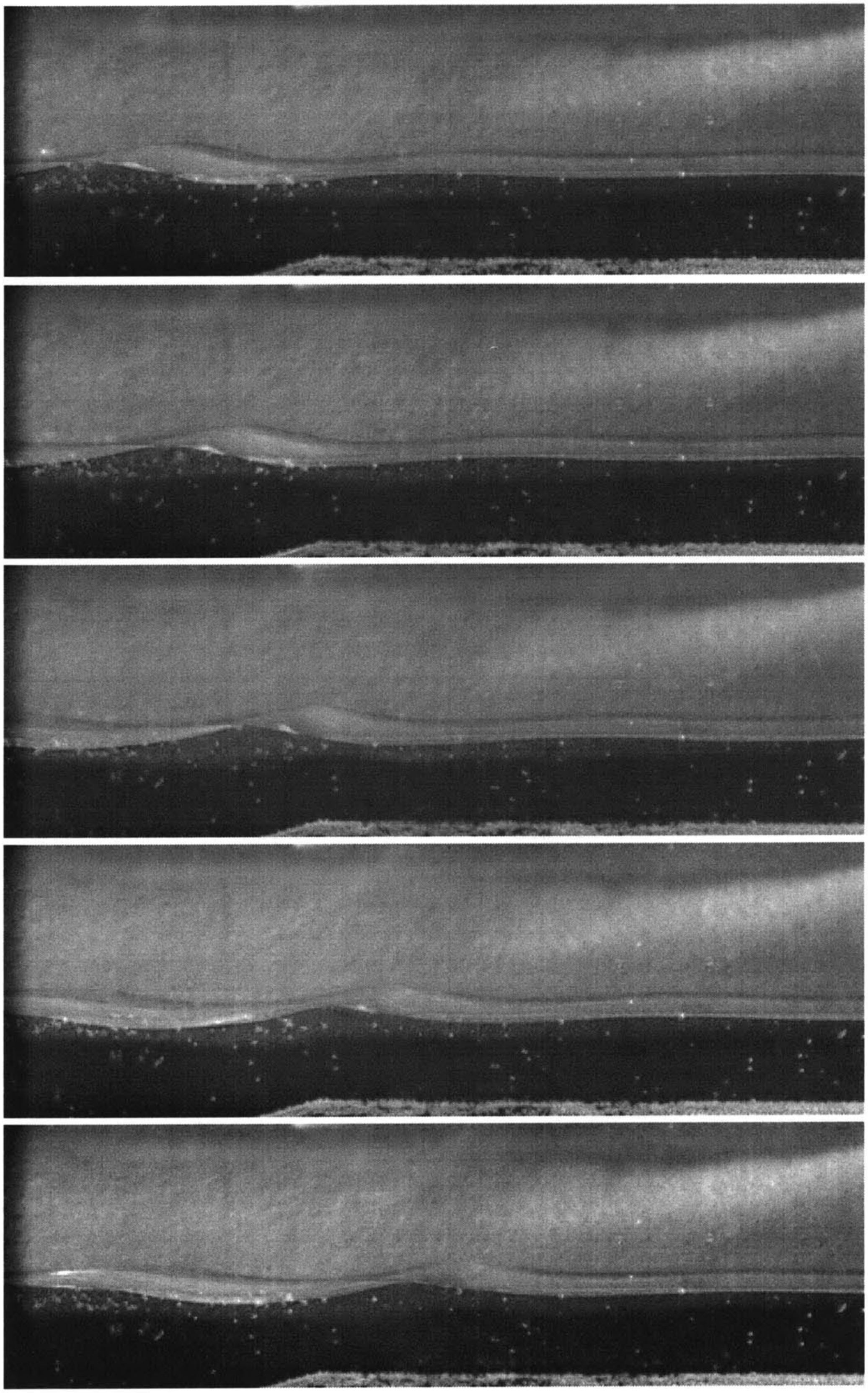

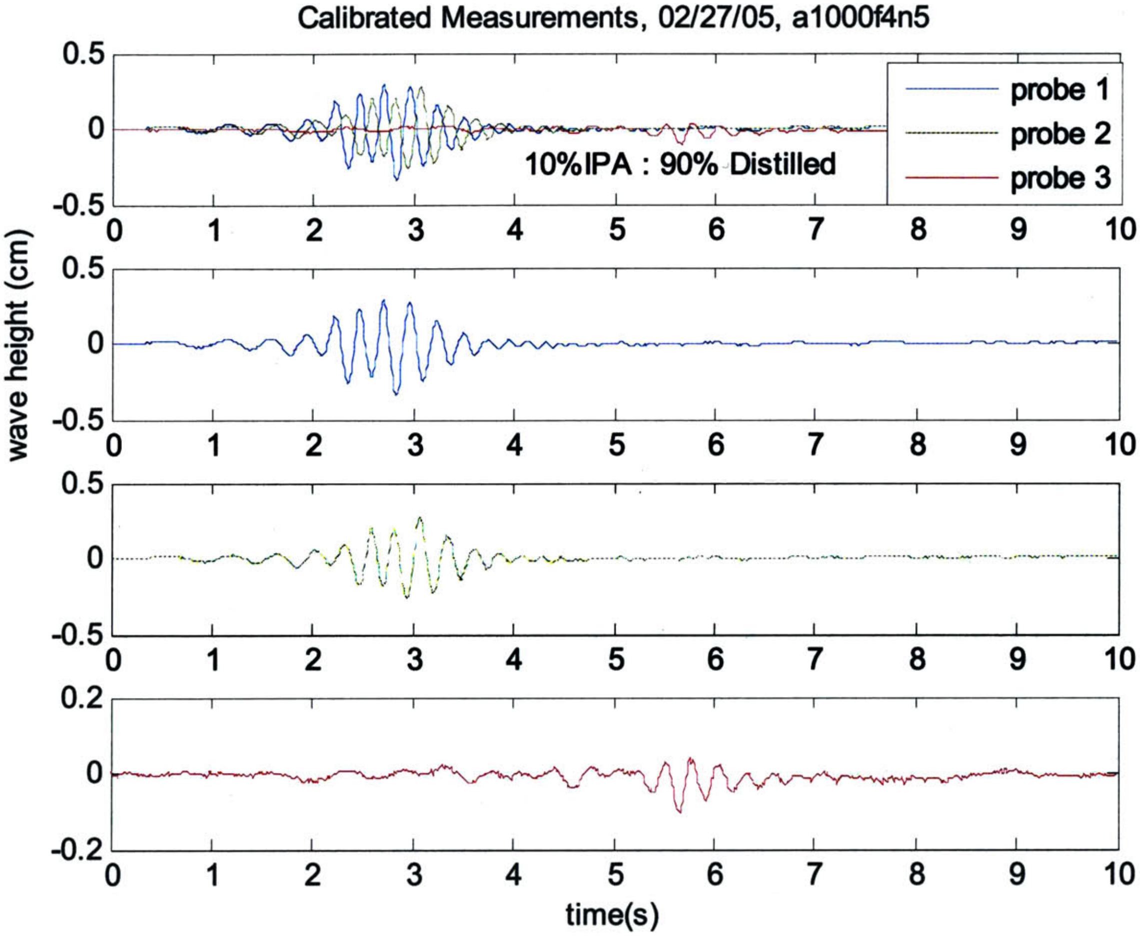

freq. (Hz)	Upstream amp. (cm)	Upstream ak	Dwnstrm amp. (cm)	Energy Remaining Dwnstrm	WE	RE	lambda (cm)	meas. Cp (m/s)	Breaking Details
4	0.24	0.148	0.06	7.08%	367	3.82E+04	10.0	0.4	spilling

Figure 4-29: Image frames (left page), probe data (top right), and wave kinematic (bottom right) parameters for the 4.0 Hz frequency case generated in five wave paddle cycles. The paddle amplitude was 0.5 cm.

4.4 Summary of Database Results

The results from the breaking wave database characterize the types of waves that can be created over a frequency band as well as providing a first order estimation of energy dissipation due to breaking. As can be seen from the images in section 4.3, non-breaking, spilling, and plunging waves were generated at frequencies between 1.5 and 4Hz. These waves have associated Reynolds numbers from approximately 38,000 through 702,000 and Weber numbers from 370 through 17,700. As is expected, waves with higher input amplitudes tend to have more energetic breaking and dissipate more energy. This is evident in the plots as well as through visual inspection of the video frames. Plunging waves were realized for frequencies of 2Hz and 2.5Hz, while spilling waves could be created at all test frequencies. The images show that the waves are not constant across the y-dimension, and they are effected by wall friction and small transverse waves. This is especially evident in the 2Hz plunging wave cases (figures 4-7 and 4-8), as the plunging jet forms in the center of the wave but only spills at the wall.

A plot of the potential energy loss across all cases is shown in figure 4-30. The general trend is that waves with higher initial slopes lose more energy to breaking and reflections when they encounter the shoal. With the exception of the 2Hz plot, there is a significant jump in energy loss between the non-breaking and spilling cases. The hollow shapes do not generally follow the trend, most likely due to the complexity of upstream breaking causing premature turbulent losses or shoal movement radiating additional wave energy. In all cases of breaking off the paddle, waves dissipated more energy between the probes than others of the same input frequency. The slope parameter on the x-axis is slightly misleading, because the data was recorded before the waves encountered the shoal. The sloping bottom concentrates the wave energy and the waves get steeper as they propagate over it. Thus, the slopes associated with the different types of breaking are well below the Stokes limiting height. They should not be interpreted as slopes at the onset of breaking or to establish a breaking criterion.

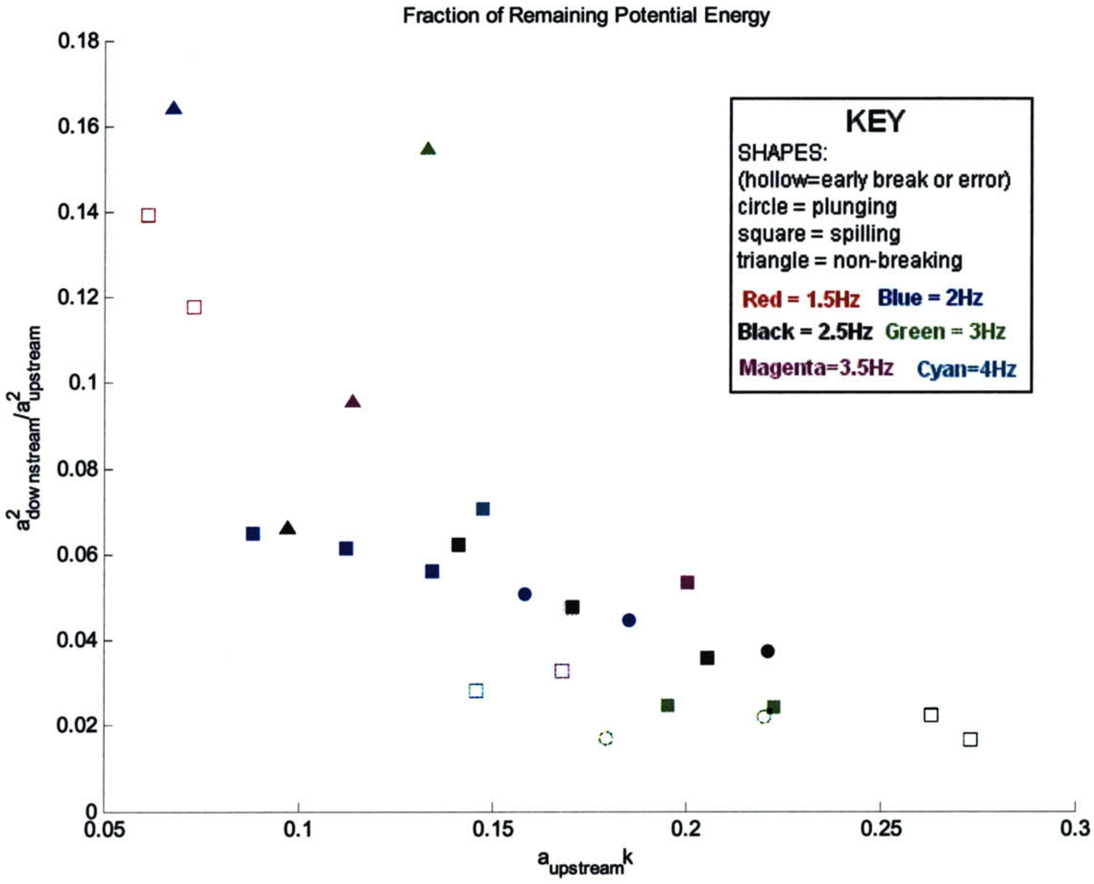

Figure 4-30: Plot of fractional remaining potential energy for all cases in the wave breaking database. The shape of the points (circle, square, triangle) indicates the type of breaking (plunging, spilling, non-breaking). The hollow shapes indicate cases of premature upstream breaking or shoal vibration. The colors represent the frequency of the wavetrain: red = 1.5Hz, blue = 2Hz, black = 2.5Hz, green = 3Hz, magenta = 3.5Hz, cyan = 4.0Hz.

The additional radiated energy is only speculated for the 1.5Hz cases, shown in red. During testing, the 1.5Hz waves caused the shoal to vibrate at an amplitude around 0.5cm. This movement is analogous to a secondary wave generator and the resulting wave field is quite complex. The limited stroke of the wave paddle resulted in a small slope for the 1.5Hz waves, even at maximum 2.5cm paddle amplitude. With a wavelength around 1/3 of the tank length, such waves are rather long for this facility.

These limitations resulted in only two test points for the 1.5Hz waves and such waves were not studied with PIV.

In contrast to the 1.5Hz case, the 2Hz waves were most ideal for the current experimental set-up. The full range of waves from plunging to spilling to non-breaking was realized by lowering the input amplitude from the maximum 2.5cm. The plot shows that the waves with the highest upstream slope lose the most potential energy. The transition from plunging to spilling occurs at a slope between 0.135 and 0.159. The remaining energy appears linear with slope through all the breaking cases with a sharp increase in the non-breaking case. Interestingly, the change in energy remaining between the most violent plunging and spilling waves is only 2%. This could be a result of the shallow plateau section reflecting the downward momentum of plunging jet and conserving the energy. If it were deep water, the plunging jet would transmit energy deeper into the water column and dissipate energy faster.

Plunging through non-breaking waves were also created at 2.5Hz. Unlike the previous case, the largest slopes did not produce plunging waves. The two largest measured upstream slopes, 0.273 and 0.263, had input amplitudes which was beyond the slope limit and the generated waves broke at the paddle. They spilled again once they reached the top of the shoal section, even though they had the large upstream slopes. These waves were turbulent before the shoaling and were able to dissipate the more energy than those which did not break upstream. Ignoring these two cases, the 2.5Hz waves transition from plunging through spilling through non-breaking as slope gets smaller. The relationship between slope and remaining potential energy is linear, even through the non-breaking test case, surprisingly. The sharp transition between energy lost to spilling and non-breaking is evident for all other tested frequencies which include the non-breaking data. The lack of such a transition could be due to wave probe errors, as there were no visual signs of breaking for this case.

The potential energy loss transition is most evident for the 3Hz waves. There is a 13% difference in remaining energy between the non-breaking and spilling cases. There is not a significant change in energy loss between the waves that broke off the paddle and those that only broke at the shoal. Although these premature breaking cases began with high slopes, the breaking caused a reduction in amplitude such that they were nearly equivalent to the others when they reached the upstream probe.

In the 3.5Hz case, the upstream breaking caused a large reduction in amplitude for the waves the broke off the paddle, resulting in small measured slopes for these spillers. They also lost more energy to the breaking at the shoal. The plot also shows transition between the non-breaking and breaking case. Only two tests were recorded for the 4Hz waves. At this frequency, there is a very limited range of input amplitudes which do not initially cause breaking and which are large enough to cause the waves to break at the shoal.

The results from the plot of potential energy losses due to breaking agree with expectations, at least qualitatively. These measurements are subject to error of the wave probes, which was discussed in Chapter 2. Although there was significant drift in the signal over time, the linearity of the calibration function means that on short time scales, the probes function well. A repeat of the first, large amplitude 2Hz run was performed 4 hours after the previous test. Although there is a 10% increase in measured upstream amplitude, there is a similar increase in downstream amplitude of 12%. The resulting percentage of potential energy remaining is nearly equivalent to the first test: 4.56% and 4.46% respectively. Thus, the probe drift cancels out in the energy comparison. Several cases from the wave breaking database are analyzed further with PIV, and the details are discussed in Chapter 5.

Chapter 5

Flow Field Measurements

5.1 PIV Methodology

Advances in laser and digital recording technologies over the last few decades have brought the cost of quantitative flow measurements down considerably, both in the processing time and price of the equipment. Two-dimensional, planar flow measurements can be readily performed using Particle Image Velocimetry (PIV) with a laser, or similar light source, and video or image recording device, such as a CCD video camera. The details of the PIV technique and processing algorithms are detailed in [30] [53]. Today PIV is used extensively to find instantaneous velocity fields for many fluid problems. Typically the flow is seeded uniformly with neutrally buoyant particles, or seeding, which are illuminated by a sheet of laser light. This illuminated region is imaged by a video camera, and pairs of successive images, separated by a short time interval, are processed to determine the movement of particles and thus the velocity of the flow field.

In this project the IDT high speed video camera, detailed in Chapter 2, was synched with a Lasiris brand Magnum near-IR, TTL Diode, line-generator laser, which was used to illuminate the flow. The seeding material was 10 μm diameter silver-coated hollow glass spheres. During the Wilhelmy plate tests it was noted that the seeding did not have significant effect on the surface tension measurements. Images were taken at 500 Hz in a modified field of view with 1260H x 404 V pixels. The laser sheet was aligned vertically in the direction of wave propagation and the camera imaged through the side of the wave tank. The images were processed using the LaVision DaVis software package with multi-pass time-series cross-correlation and final window size of 16 x 16 pixels. Vorticity was calculated from the velocity fields, and the resulting plots show regions of clockwise vorticity in red, regions of counter clockwise vorticity in blue and zero vorticity in green.

An objective of this study is to examine the flow fields around a wave during the breaking event. Sections 5.2 and 5.3 present the results of PIV of the water-IPA solution for plunging and spilling cases. The IR laser sheet of negligible thickness in the y-direction illuminates the fluid for processing planar flows. In addition to using the images for PIV post-processing, the recorded video was used to create profiles of the 2D wave deformation during breaking. To study the entire flow field around the breaking wave, a novel technique was developed to seed the air and water and perform simultaneous PIV of the two-phased flow. Unfortunately, the values of vector magnitudes and vorticity in the plots that that follow are not included, and the accuracy of the PIV processing has not been fully verified. Nonetheless, the images are qualitatively reasonable and agree with numerical results.

While seeding in the water was straight-forward, seeding in the air was quite complex. Typical air-seeding techniques such as atomized oil droplets are not appropriate in this study as the oil would influence the surface tension significantly. Thus a water-based fog was used to seed the air. High speed video results show the formation of the vortex aft of the breaking wave and reveal strong counterclockwise vorticity in the air side of the interface. Conversely in the water, the majority of the vorticity has clockwise rotation for waves traveling from left to right.

Figure 5-1 shows a snapshot of velocity (top) and vorticity (bottom) for a plunging breaker after the jet from the face of the wave has impacted the free surface and the air cavity has collapsed into smaller bubbles. Vector colors and length in the top plot represent magnitude of velocity from high (red) to low (blue). In the vorticity plot, the red represents clockwise vorticity and the blue counterclockwise vorticity. The red line shows a profile of the surface above which there is no water. Below this line is water except where air bubbles have been entrained due to the plunging jet. More images from the processed results are presented in section 5.4.

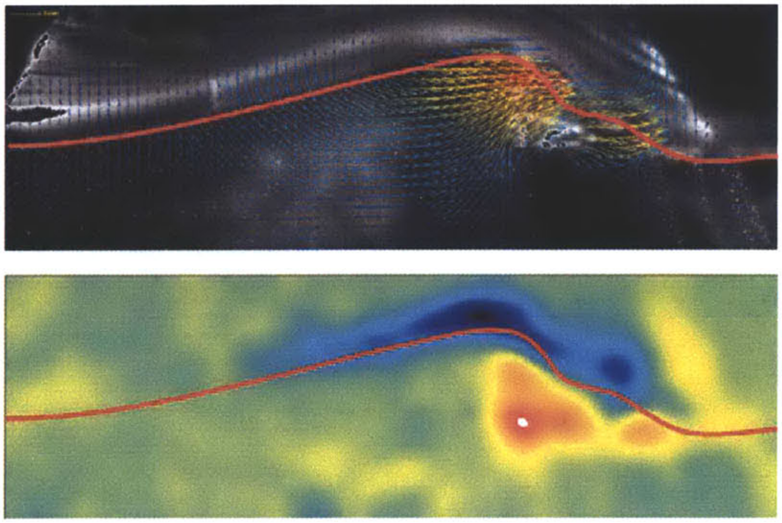

Figure 5-1: PIV measurements of the flow field, velocity (top) and vorticity (bottom), for a breaking wave just after the jet has plunged into the free-surface. The wave is moving from left to right. Red represents clockwise vorticity and blue counterclockwise vorticity in the lower plot.

5.2 Spilling Breaker

The typical characteristics of a small scale spilling wave described by Duncan [19] are illustrated in figure 5-2. The image displays 4 superimposed wave profiles which describe the spilling event of a 3Hz wave with the same input parameters as figure 4-21. The profiles were generated using a Sobel edge-finding method which is included in the MATLAB image processing toolkit. This edge-finding algorithm was applied to the spilling images obtained using the high speed camera, laser sheet and seeded solution. The wave steepens at the top of the slope and forms a bulge-toe shape at the crest. The toe spills then down the face of the wave under the influence of gravity and forms a turbulent region. The turbulence engulfs the front face of the wave just as it moves beyond the illuminated region. While the laser sheet illuminates a 2D section of the flow, 3D effects and a weak laser make it difficult to resolve the edge precisely. Thus, some edges are non-existent while others are blurred and spotty. The velocity and vorticity fields from a similar spilling wave are presented in figure 5-3 and 5-4.

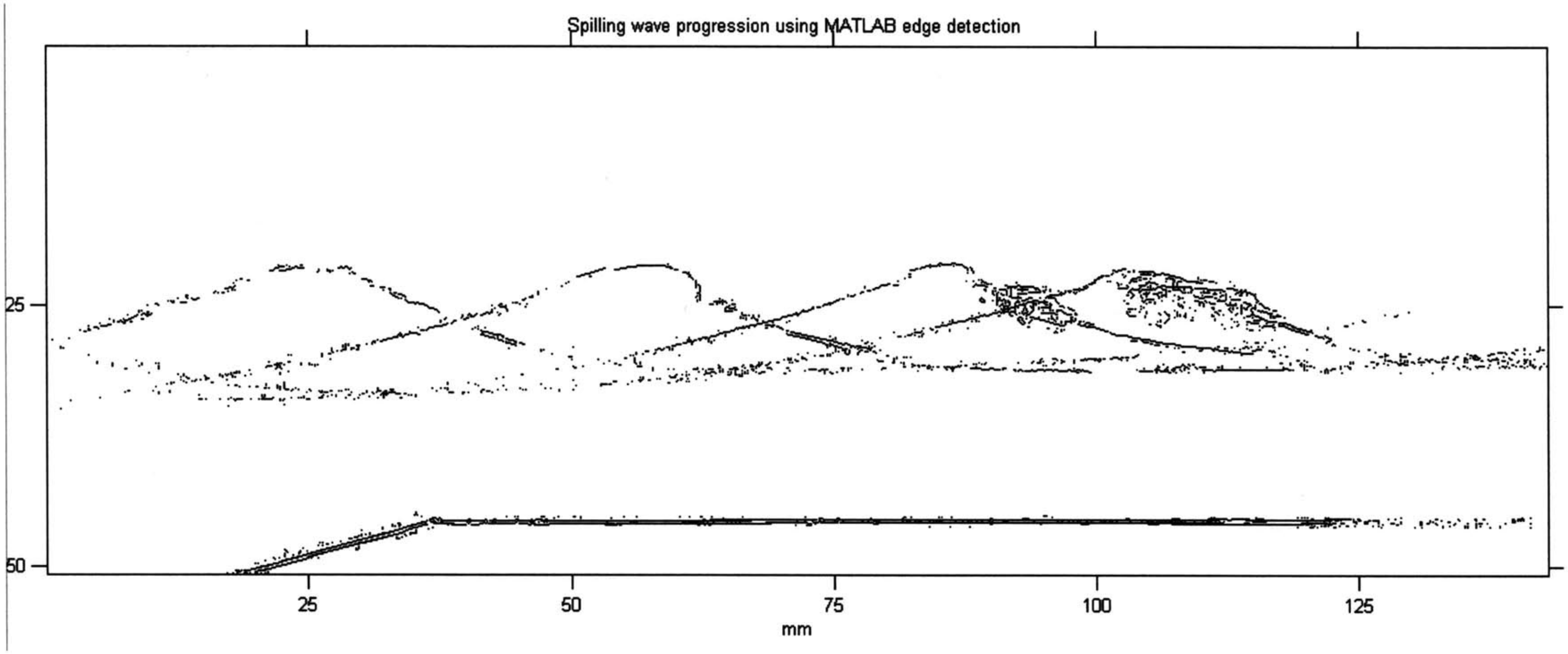

Figure 5-2: Spilling wave profiles generated with the Sobel edge-finding method on MATLAB. Notice the characteristic bulge-toe formation that leads to turbulent flow on the front face of the wave. This is a 3Hz wave corresponding to figure 4-21 in the breaking wave database.

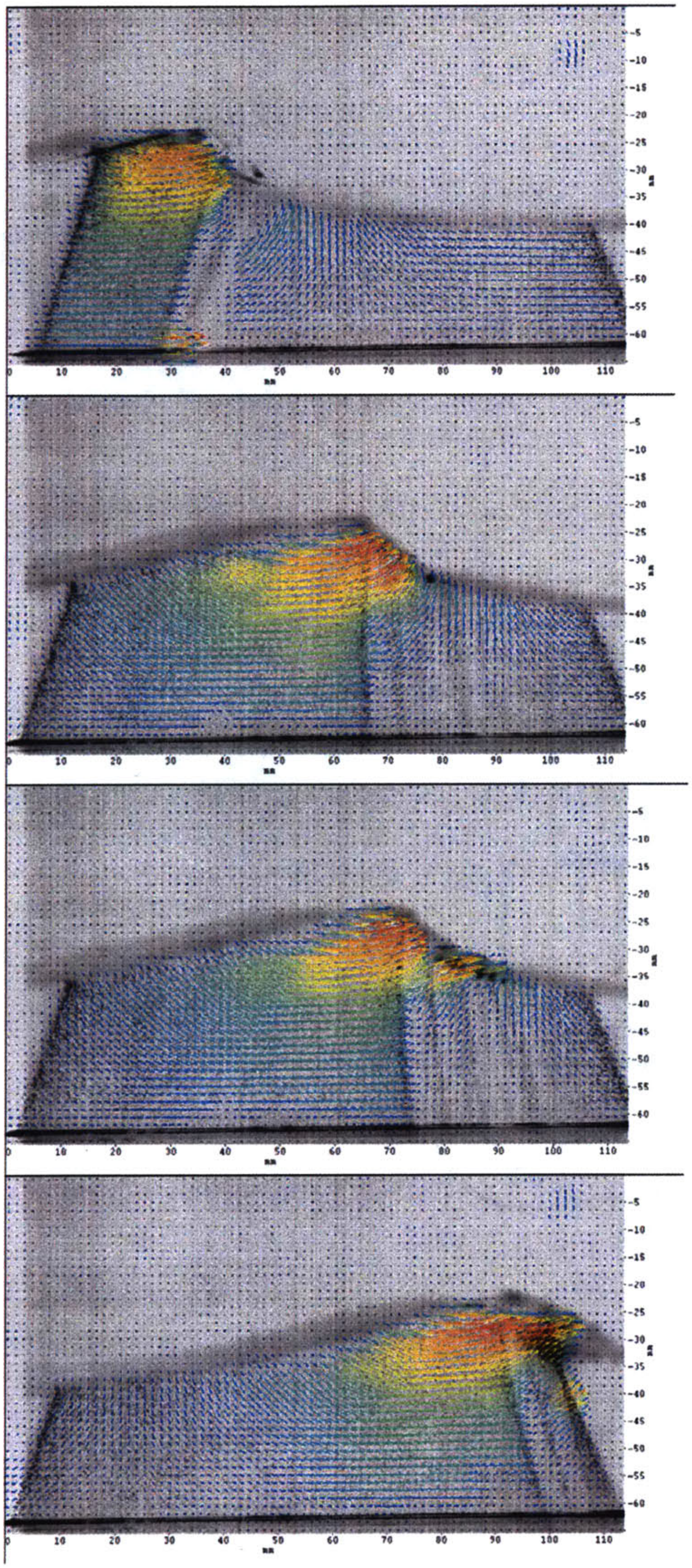

Figure 5-3: Velocity fields for a 2Hz spilling breaking wave with the same parameters as figure 4-10 in the breaking wave database. The highest velocity region is in the crest and the magnitude seems to increase (become more red) through the breaking.

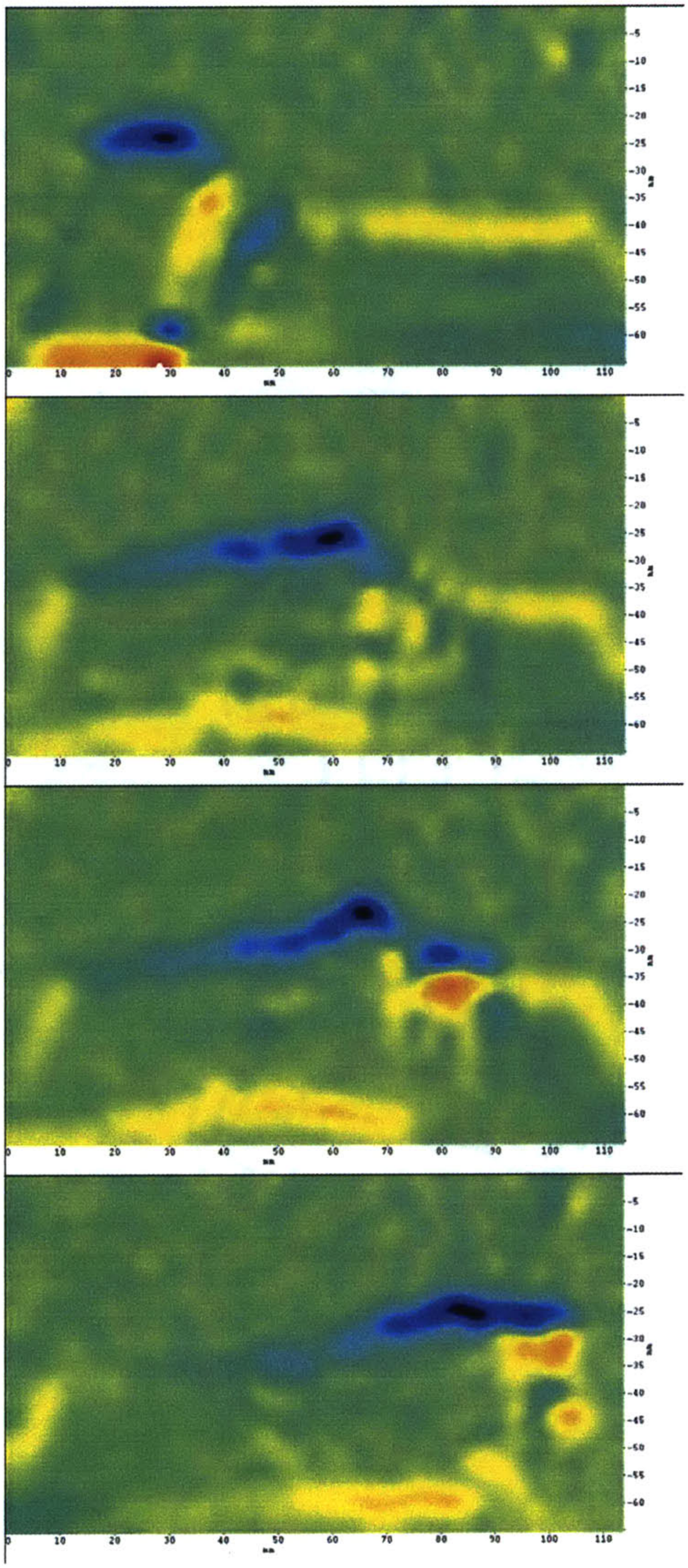

Figure 5-4: Vorticity fields for the same 2Hz spilling breaking wave as in figure 5-3. Blue is counterclockwise vorticity and red is clockwise. Since the air was not seeded, the blue vorticity may be an artifact of processing. Most of the vorticity develops in the positive direction through frame 3 and 4.

In regards to figure 5-3, the black diagonal lines near edges mark the area illuminated by the laser. The other dark lines are a result of the curved profile refracting the laser light. The low intensity laser and curved fluid surface resulted in refractions which moved in time and illuminated different parts of the flow. Thus, some parts of the flow field or more resolved than others. The velocity field shows that most of the particle motion takes place near the free surface, with the highest particle velocity at the crest. Also, the magnitude of the motion increases through breaking. Most of the velocity arrows trace a concave up, counterclockwise path toward the front face of the wave, while the particles to the right of the trough trace a concave up, clockwise path. Unfortunately, the velocity field within the turbulent bulge is not well resolved.

Aside from the blue region of vorticity on top of the wave in figure 5-4, there is not much vorticity in this spilling breaker. This is expected for the spilling case, since vorticity does not develop in the wave until the bulge propagates down the front face of the wave. The blue region above the crest may be an artifact of processing. The particles near the crest are in motion, but there is nothing on the air-side of the flow. The rapid change in velocity across the free surface is misinterpreted as vorticity. In the top frame, the diagonal lines of positive and negative vorticity are a result of the laser refraction. The positive vorticity near the base is a result of fluid shear along the plateau wall. The red region developing on the front face in frames 3 and 4 is real and a result of the turbulent flow developing as the wave breaks down.

5.3 Plunging Breaker

The use of isopropyl alcohol in the solution changed the surface tension such that a plunging breaker could be created. The profile of such a breaking wave is illustrated in figure 5-5, featuring a plunging jet forming as the face gets vertical. This wave is the most dramatic plunging wave from the database (4-7). The wave is much larger and creates more turbulence than in the spilling case after the jet impacts the free surface. Figures 5-6 and 5-7 illustrate the velocity and vorticity fields for this wave.

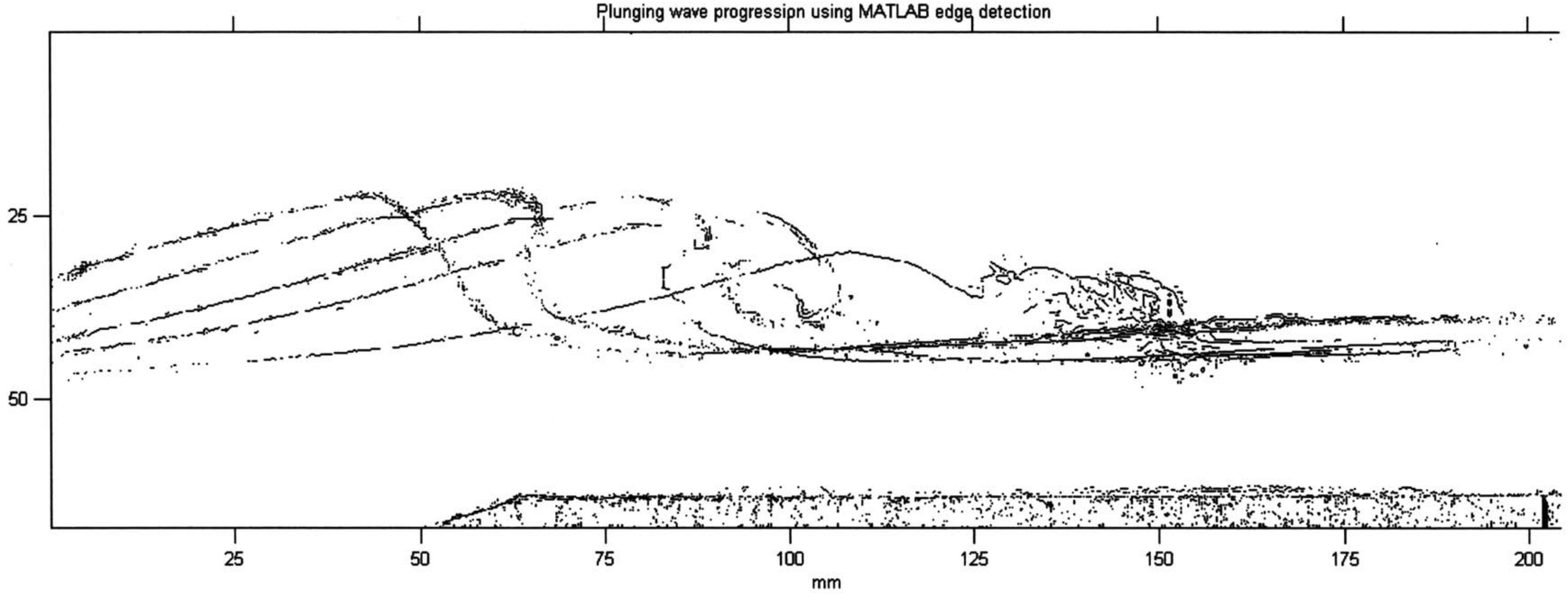

Figure 5-5: Plunging wave profiles generated with the Sobel edge-finding method on MATLAB. Notice the plunging jet that forms and entrains air as it impinges on the free surface. This is a 2Hz wave corresponding to 4-7 in the breaking wave database.

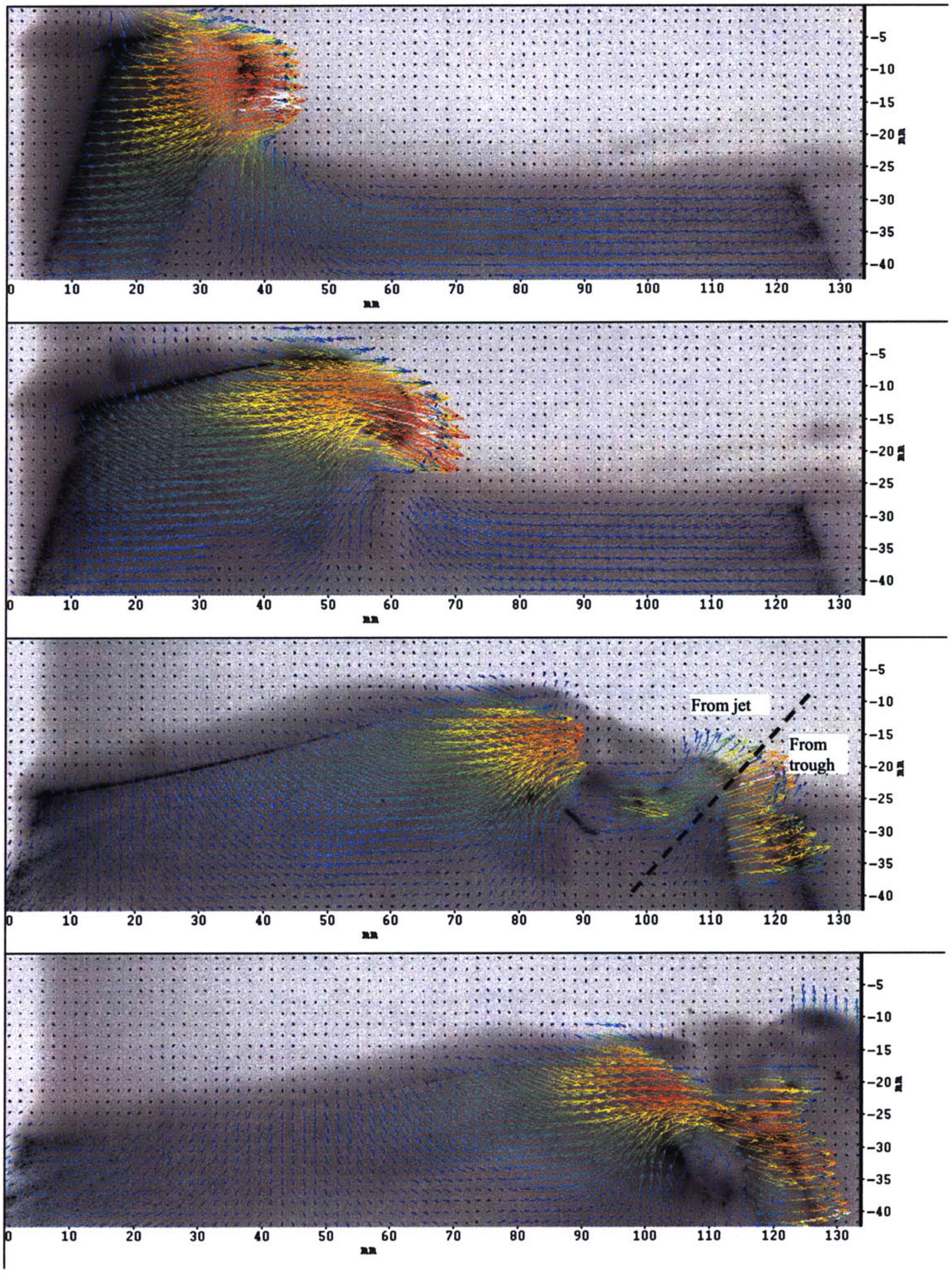

Figure 5-6: Velocity field for the plunging wave with the same input parameters as figure 4-7 in the database. The plunging jet entrains air and causes a significant slash-up. The dotted line divides source the splash-up. A mixed gas-liquid flow develops.

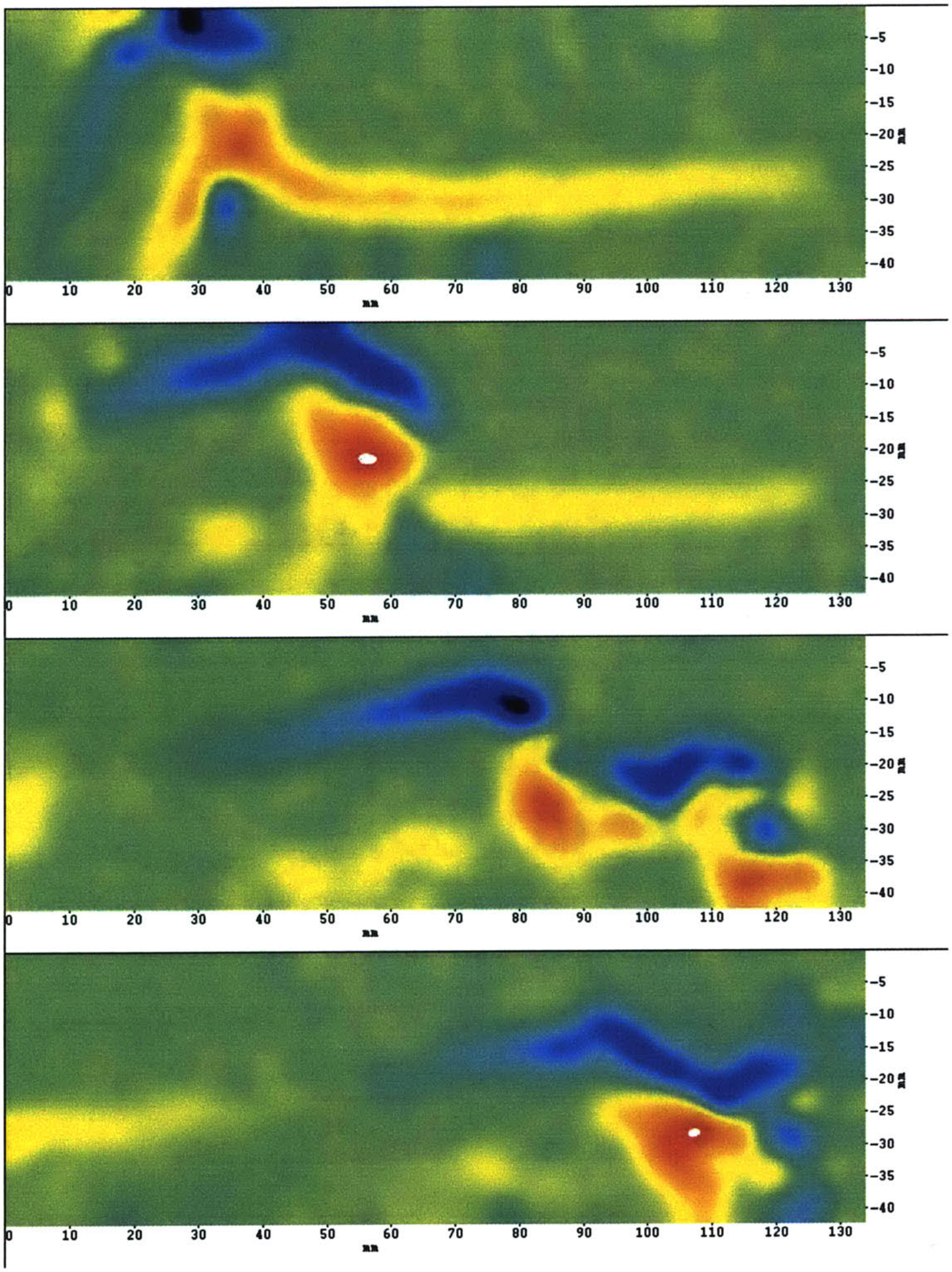

Figure 5-7: Vorticity fields for the plunging wave in figure 5-6. Red represents clockwise vorticity and blue is counterclockwise. Notice the strongly positve (red) region in frame 2 and the development of a second positive region during the splash-up in frame 3.

The velocity fields in figure 5-6 show that the highest particle velocities are near the crest. The arrows trace paths which converge at the crest where the jet develops. As wave slope transitions beyond vertical, the plunging jet shadows some of the wave from the laser light, preventing it from being resolved well. The maximum velocity appears in frame 2, as the wave ejects and the jet falls under gravity. In frame 3, the jet has just impacted the surface, causing the splash-up phenomenon described in [7]. It appears as though the upper region of the splash up is made of particles from the reflected jet, while the underside is composed primarily of fluid from the trough. As plunging motion continues, the entrained air and water undergo turbulent mixing. Unfortunately, the turbulent region is not fully resolved spatially.

Figure 5-7 shows that the vorticity present in the plunging wave is much greater than in the spilling case. Again, the negative blue vorticity is likely caused by a processing error. The primary vorticity region, in red, is located just beneath the crest and is most strong in the second frame. When the jet impacts the surface, a second patch of positive vorticity forms under the splash-up. The sum of the two individual regions of positive vorticity in frame two appear to equal the vorticity in frame 2. The second region moves beyond the laser field in frame 4.

5.4 Air-Water Flow Visualization

Air flow structures above the breaking wave were visualized by injecting fog into the tank. The same plunging wave discussed in 5.3 was examined in these tests, with Reynolds and Weber numbers around 280,000 and 5200, respectively. The unprocessed high speed video displays air vortices developing at the back of the wave after it plunges. One large primary vortex appears in figure 5-8 which revolves counter-clockwise. This feature is comparable to the vortex shed in the classic problem of flow over a hill. In this case, it expands and moves upward as the broken wave propagates forward. Figure 5-9 shows a close-up view of the boxed region in figure 5-8 over time. A closer look reveals the formation of smaller vortices near the primary vortex.

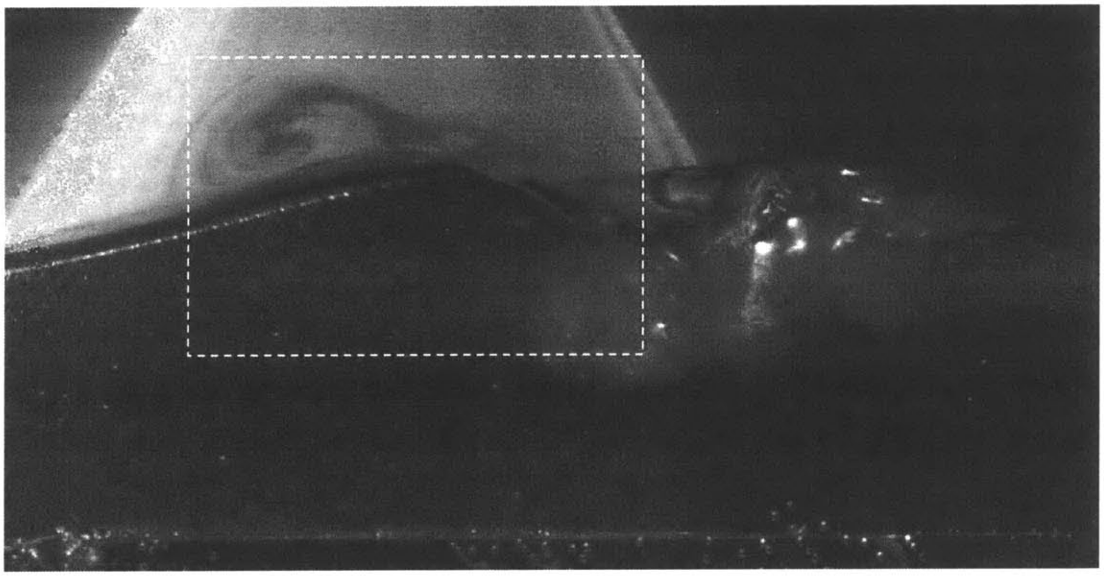

Figure 5-8: A wide angle view of a vortex in the air above a plunging breaker, after the plunging jet has impacted the water and caused splash-up.

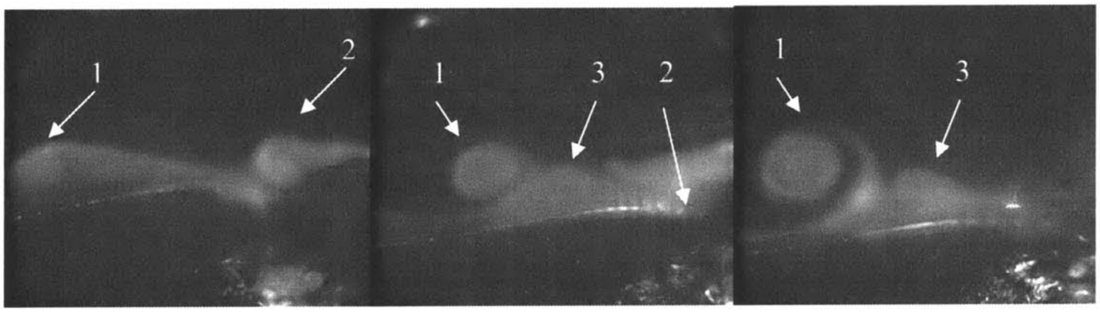

Figures 5-9: Visualization of the vortices developing in the air after the plunging jet has impacted the water and caused splash-up. The evolution of smaller vortices can be seen in temporal progression from left to right and the individual vortices are labeled.

In [7], Bonmarin discusses the structures present after the jet has impacted the water through the splash-up and flow degeneration. In addition to the pocket of air entrained as the jet impacts the surface, he describes a process where air entrainment occurs due to the interaction of the plunging jet with the rear vortex of the splash-up. This process is evident in figure 5-9, as vortex "2" is consumed in the fluid wedge. As vortex "1" moves upward from the free surface, a third vortex appears which also rotates in the counter-clockwise direction. A fourth, clockwise vortex much smaller than the ones pictured above was also observed to occur underneath vortex "1". It was not present in the result displayed in figure 5-9. PIV results are shown in figures 5-10 and 5-11.

Difficulties associated with achieving uniform fog seeding made resolution of the air flow imprecise. The fog particles being much smaller than the tracers in the water along with the laser reflection off the curved free surface further complicated the measurements. As a result, the velocity fields primarily map large scale motions rather than individual particles. However, the processed velocity and vorticity fields in the mixed seeding case do yield reasonable results. The rotating region from the splash-up described by Bonmarin appears in frames 3 and 4 of figure 5-11. In figure 3, the approximate wave profile and splash-up directional arrows were added, and they agree with a frame 1923 Bonmarin's results. Frame 2 depicts vorticity field of the wave as the crest ejects out over the free surface, and it is compared to Hendrickson's numerical results in figure 5-12.

Using direct simulation of the Navier-Stokes equations, Hendrickson computes a plunging wave profile using an impulsively started Airy wave. The Reynolds number for her simulation was 2,000 and the Weber number was set at 73,868 to reduce the influence of surface tension. A frame from the simulation is depicted in figure 5-12 along with a similar result from this research. Though the breaking mechanism and scaling parameters were different than in Hendrickson's study, the resulting vorticity plots and profiles are similar. It should be noted that the tip of the plunging jet and region of air beneath it were not well resolved in the high speed video. The negative vorticity on the back of the plunging wave is similar to region in the numerical model, and figures 5-8 and 5-9 illustrate vortices being shed in this area. The region of positive vorticity in the experimental results extends further into the fluid and deeper than in the simulated result. This discrepancy could be a result of bottom interaction with the shoal and plateau. Hendrickson's simulation also shows more positive vorticity in the air, which may actually exist. Improvements to the air seeding technique could improve the flow resolution and show such vorticity. Despite these differences and possible improvements to the technique, the results from this first attempt at imaging flow fields in the air and water agree well with the numerical model.

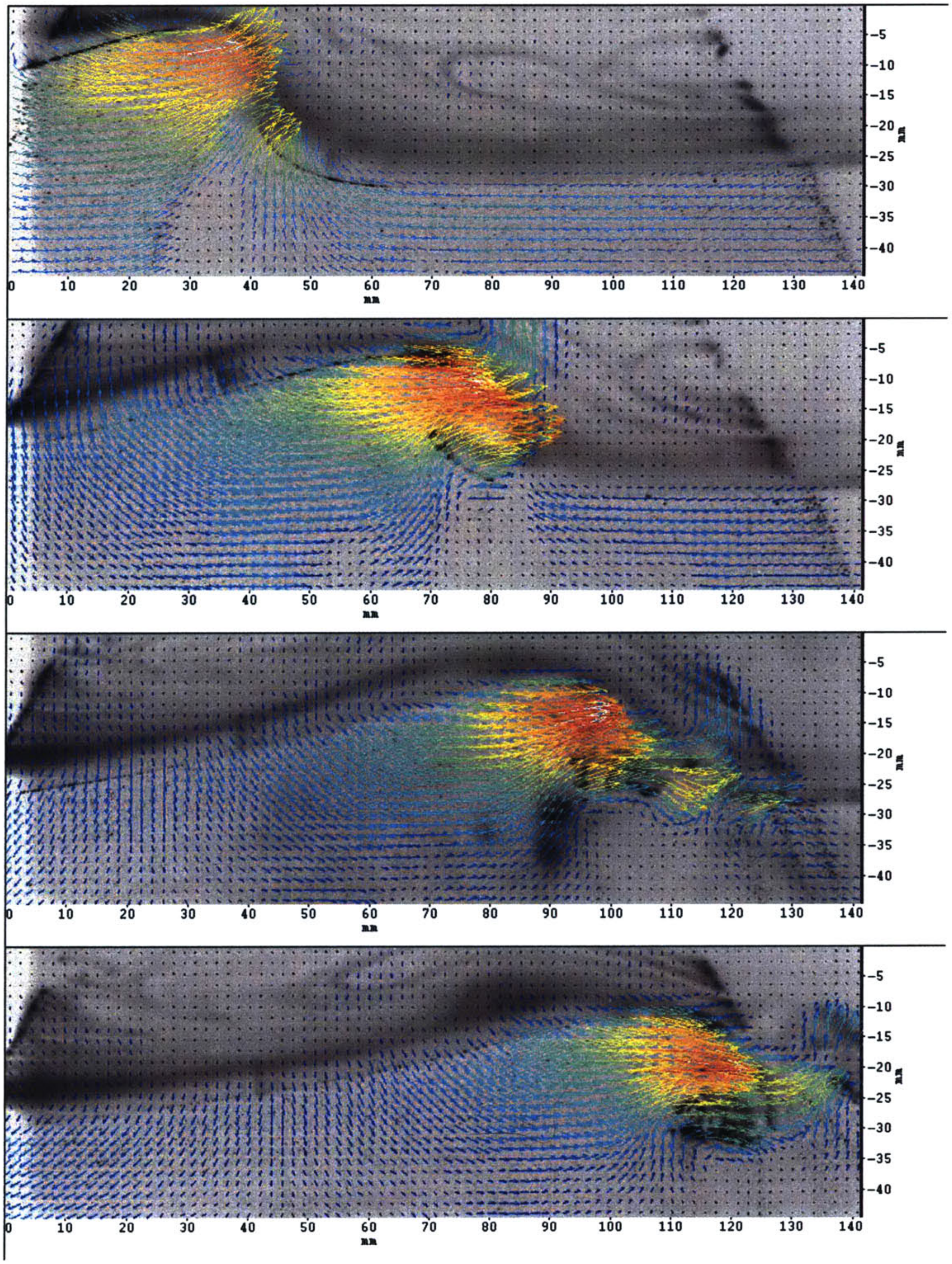

Figure 5-10: Processed velocity field for the plunging wave with fog seeding in the air. The largest particle velocities in the air and water occur near the plunging jet.

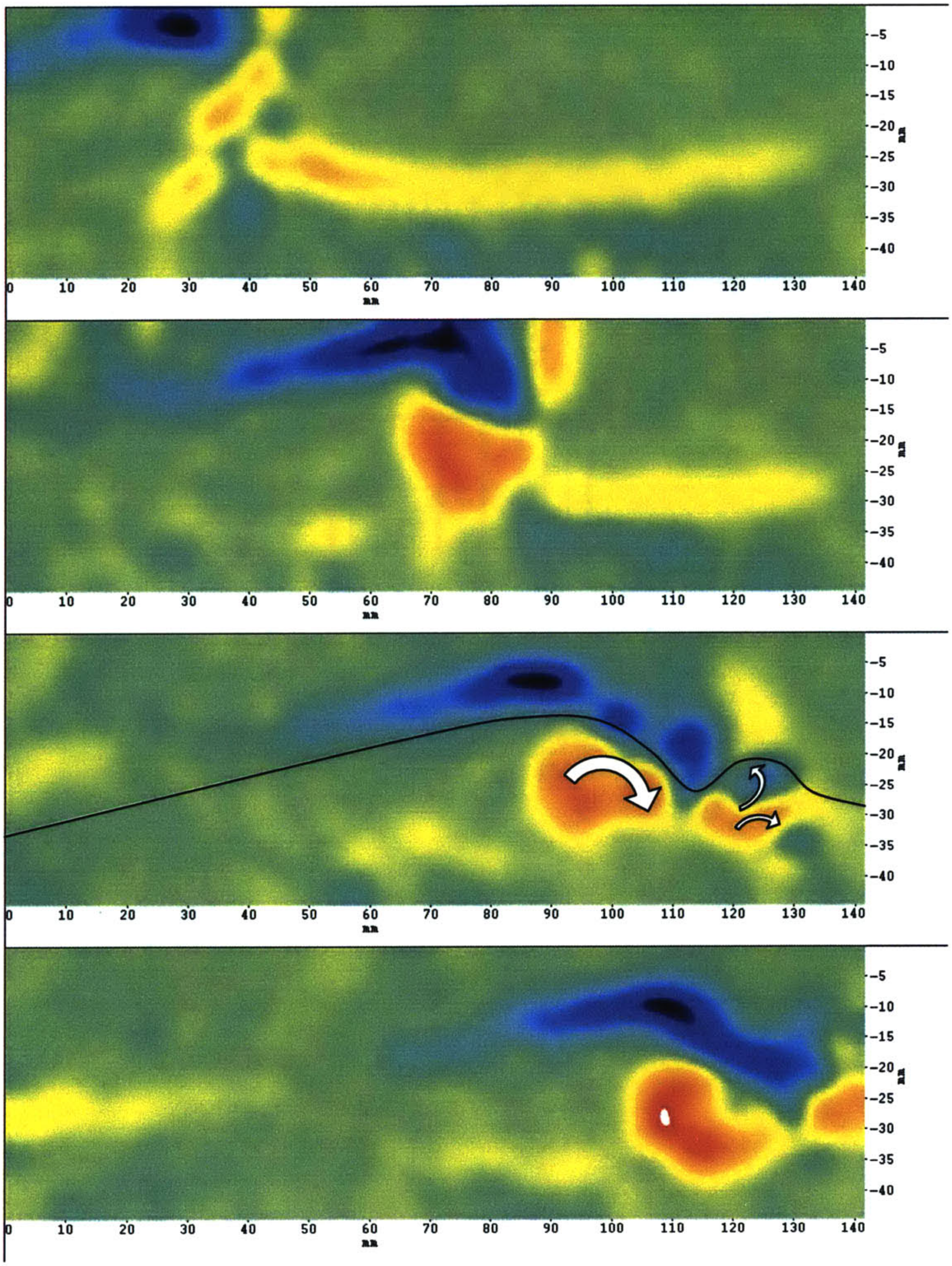

Figure 5-11: Vorticity fields for the plunging case with fog particle seeding. The secondary region of vorticity appears in figure 3. The approximate wave profile and slash-up arrows in frame 3 are similar to Figure 19 in Bonmarin's paper [7].

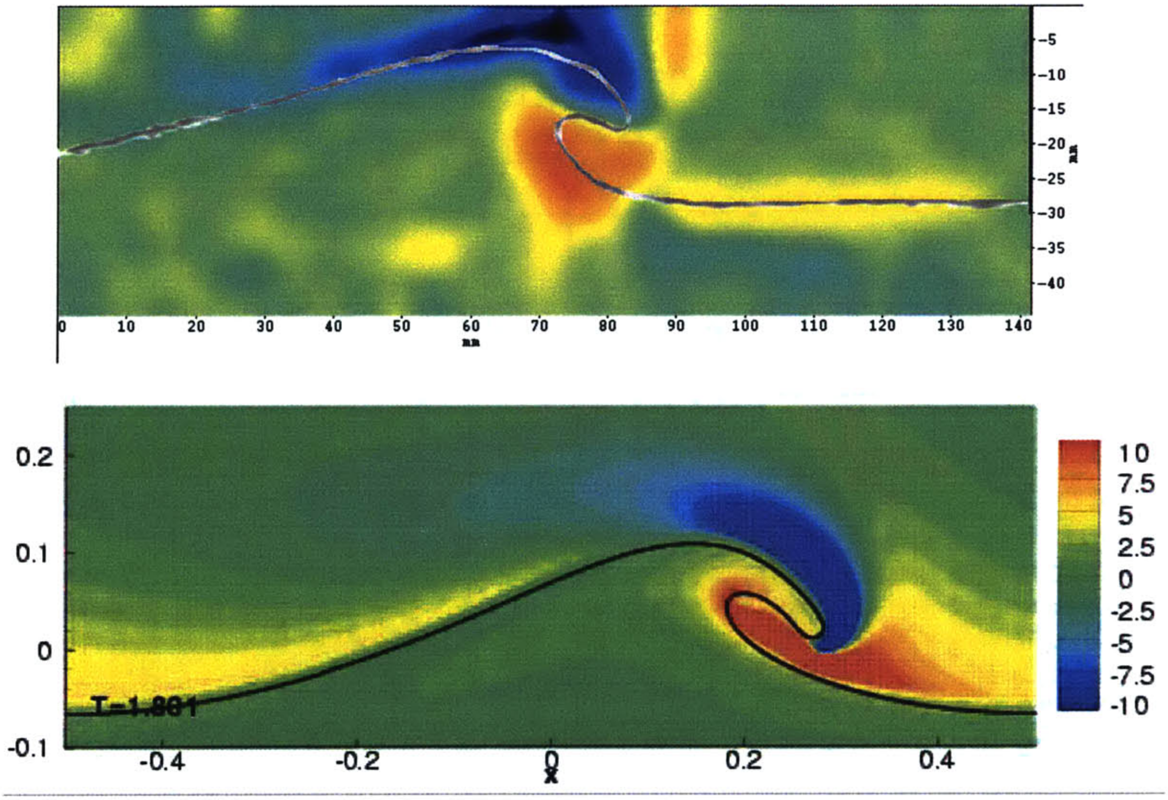

Figure 5-12: Frame 2 from figure 5-11 is reproduced with the surface profile of the wave superimposed. The result agrees qualitatively with the numerical results from Hendrickson [25].

Chapter 6

Conclusions

6.1 Summary

In this thesis, an experimental investigation was performed using advanced fluid measurement techniques with the objective of providing insight into the non-linear phenomena of wave breaking at small scales. Understanding the dynamics of these events has relevance in the design of efficient and undetectable ships as well as offshore and coastal structures. On a global scale, wave breaking affects the atmospheric and ocean circulations which influence climate. Traditionally, researchers have used observations to classify the type of breaking based on kinematics as spilling, plunging, surging, and collapsing. Waves are also characterized temporally as either steady, unsteady, or quasi-steady. The unsteady spilling and plunging waves occur most often in nature, and accordingly, they have received the most attention in the previous research. Since wave fields in the open ocean and other bodies of water are typically large and chaotic, they are difficult to study using conventional techniques. Linear wave theory falls short of describing steep and breaking waves, and the governing, non-linear, partial differential equations are too difficult to solve analytically at this point. Researchers have thus used laboratory facilities and numerical codes to model and study the physics of breaking waves. Additionally, most studies have used the approximation of two-dimensional waves to limit spatial complexity.

There have been many laboratory studies of breaking waves completed over the past hundred years. The results of these studies have generated empirical relationships describing characteristics such as wave steepening on slopes as well as examining the potential energy losses due to breaking. The unsteady research typically involves waves with wavelengths on the order of 1m, and breaking is generated using dispersive focusing, bottom shallowing, or converging tank walls. Steady and quasi-steady waves have been studied in experiments by towing objects near the free surface, flowing water over fixed objects, or through the use of hydraulic jumps.

In addition to experimental studies, solutions to the governing equations through the use of numerical approximations have enhanced knowledge of breaking waves. Most early results relied upon potential flow simulations which model the dynamics quite well through steepening, but do not allow for vorticity or viscous effects. These simulations can be performed up to the point where the jet impinges on the free surface for plunging waves and up to bulge-toe formation in the spilling case. Recent advances in computer processing capability have improved upon the early simulations by the allowing for the inclusion more physical effects and resolving some turbulent structures. A direct simulation of the Navier-Stokes equations performed by Hendrickson [25] resulted in a database of breaking waves which includes viscous effects, surface re-entry, and air effects. As with all computer simulations, the significance of the results is based upon their ability to accurately model real-life events. The Hendrickson simulations were performed for deep water waves at a much smaller scale than current experimental results. They also include the air-water flow fields, an interaction that has not been well-examined in a laboratory tank. Though the simulated wavelength may be too small to actualize in a conventional wave-tank, the objective of this research was to explore wave breaking at a scale smaller than current experimental results and to examine the air effects using Particle Image Velocimetry.

The research described in this thesis was performed in a small, narrow wavetank described in Chapter 2. A computer-controlled wavemaker consisting of a linear motor and hinged paddle was positioned at one end of the tank, while an energy absorbing beach placed at the far end mitigated wave reflections. A 15 degree ramp leading to a level plateau section forced waves to break as propagated down the tank. Three surface piercing wave gauges were used to record time traces of the wave signal before and after the breaking event. High speed video and PIV were also used to record and analyze the breaking waves in this study.

The scale of the waves in this research was sufficiently small for the breaking dynamics to be strongly influenced by the surface tension of the fluid. Early experimental results revealed that plunging breakers could not be realized in filtered tap water or distilled water. However, adding a small amount of isopropyl alcohol resulted in the creation of a plunging wave. The Wilhelmy plate technique was used to quantify surface tension changes over a variety of test conditions. A primary result from this testing was that, although IPA is soluble in water, the solution must be well-mixed in order to prevent the lower density IPA from concentrating near the surface. A constant low surface tension can be maintained by using an initially stirred mix of IPA and distilled water in a covered container. As such, a well-mixed solution of 10% IPA was used throughout the wave breaking experiments.

To characterize the range of breaking waves which could be created in the facility, a breaking wave database was generated. This database included 26 different wave trains studied over a frequency band of 1.5-4Hz. The corresponding Weber numbers ranged from around 14,600 down to 400, with Reynolds numbers from 280,000 to 38200. Plunging, spilling and non-breaking waves were recorded with a video camera and wave probes. The camera revealed that even with a uniform paddle across the y-dimension creating the waves, the shape of breaking waves varies across the tank, and the kinematics are significantly affected by the presence of the side walls.

Comparing the amplitudes of the upstream and downstream wave probes allowed for a first-order approximation of the potential energy lost to breaking. The plot of fractional remaining potential energy downstream shows that the relationship between energy loss and slope is frequency dependent. For the most part, the results agree with expectations and show that waves with the highest upstream slope lose the most energy as they propagate over the shoal. The exception to this is that waves which initially broke off the paddle lost the most energy between the probes, regardless of slope. They experienced turbulent losses before reaching the shoal and continued to dissipate energy when they broke again at the ramp. Limited quantitative arguments or empirical relations can be derived due to the errors associated with the wave probe repeatability.

A plunging and spilling case were selected from the wave breaking database for further study through the use of PIV. In both cases, the highest velocity region was in the breaking crest, as predicted by previous research. There was very little vorticity present in the spilling wave, with a small region apparent on the front face after the bulge-toe formation breaks down. Conversely, significant regions of vorticity were found in the plunging case. The primary area of positive vorticity was located just under the plunging jet where the surface curvature is most extreme. When the jet impacts the surface, positive and negative regions of vorticity occur in the splash-up. Additionally, the splash-up appears to be composed of particles from the falling jet and the trough in a relatively equal ratio. Refraction and reflection of the laser sheet along with shadowing effects prevented the flow fields from being completely resolved through the breaking event. In addition to PIV processing, the video was used with an edge detection algorithm to capture surface deformation as the wave breaks.

A novel technique was employed by seeding both the air and water to examine the interaction of the flow fields with PIV. Tracer particles of water soluble fog (which did not affect the surface tension) were injected above the fluid for a plunging wave case. The raw video results show air vortices developing behind the plunging crest. In the processed vorticity plot, the structures were qualitatively similar to Hendrickson's numerical results, despite the differences in wave breaking mechanisms and scale. The resolution of the processed results was limited by difficulties in creating a uniform seeding in the air and due to the size differences between the fog particles and reflective glass spheres.

6.2 Future Work

The high degree of complexity of the breaking problem leaves much room for future research through experiments, numerical simulations, and in examining the large-scale wave field. Even the small waves examined in this research were by no means studied exhaustively. If the current experimental set-up was used again, the PIV technique could be improved by implementing a stronger laser and illuminating the flow from other angles. The results from this experiment could be examined further to test the quantitative accuracy of the PIV processing. Better seeding in the air side would allow for a true, quantitative measurement of the flow fields to be obtained. Additionally, more precise and repeatable wave probes could be used to look more closely at potential energy dissipation.

More generally, different wave breaking mechanisms such as different angled shoals could be implemented to compare the resulting waves. Wave focusing would allow for deep water breaking waves to be studied, eliminating the reflections and complex interactions with the sloping bottom. To more accurately compare the results to Hendrickson's simulations, smaller waves need to be created. As such, the surface tension would need to be reduced even more. It is difficult to say whether plunging waves on the order of those in the simulations are physically realizable, but regardless, there are some scalability issues that need to be resolved. Even the largest waves studied in laboratories are influenced by surface tension effects. In order for all of the experimental and numerical results to apply to the full-scale wave field, further research is needed to examine the scalability of breaking waves.

Bibliography

[1] Adam NK. 1946. *The Physics and Chemistry of Surfaces*. Oxford University Press, London.

[2] Azarmsa SA, Yasuda T. 1997. Deformation and Decay of Different Classes of Breakers. *J. Waterway, Port, Coastal, and Ocean Engineering*. July/August: 200-207.

[3] Baba, E. 1969. Study on separation of ship resistance components. Technical Report 59, Mitsubishi Heavy Ind. Tech. Bull., Tokyo, Japan.

[4] Baldock TE, Swan C, Taylor PH. 1996. A Laboratory Study of Nonlinear Surface waves on Water. *Phil. Trans. R. Soc. Lond.* A 354: 649-676.

[5] Battjes JA, Sakai T. 1981. Velocity field in a steady breaker. *J. Fluid. Mech.* 111: 421-437.

[6] Bigg, GR. 2000. The Oceans and Climate. *Issues in Environmental Science and Technology No. 13: Chemistry in the Marine Environment*. The Royal Society of Chemistry.

[7] Bonmarin P. 1989. Geometric properties of deep-water breaking waves. *J. Fluid Mech.*209:405-433.

[8] Ceniceros HD, Hou TY. 1999. Dynamic generation of capillary waves. *Phys. Fluids*. 11(5): 1042-1050.

[9] Chang KA, Liu PLF. 1999. Experimental investigation of turbulence generated by breaking waves in water of intermediate depth. *Phys. Fluids*. 11 (11) 3390-3400.

[10] Chang KA, Hsu TJ, Liu PLF. 2001. Vortex generation and evolution in water waves propagating over a submerged rectangular obstacle, Part I. Solitary waves. *Coastal Engineering*. 44: 13-36.

[11] Chen DJ. 1994. Designing Wave-measuring Instruments. *Masters Thesis*. MIT/Ocean Engineering.

[12] Chen et al. 1999. Two-dimensional Navier-Stokes simulation of breaking waves. *Phys. Fluids*. 11(1): 121-133.

[13] Dabiri D, Gharib M. 1997. Experimental investigation of the vorticity generation within a spilling water wave. *J. Fluid Mech.* 330: 113-139.

[14] Davies JT, Rideal EK. 1963. *Interfacial Phenomena.* Academic Press, NY.

[15] Davis MC, Zarnick EE. 1964. Testing ship models in transient waves. *Fifth Symposium on Naval Hydrodynamics*. p. 507.

[16] Dommermuth et al. 1988. Deep-water plunging breakers: a comparison between potential theory and experiments. *J. Fluid Mech.* 189:423-442.

[17] Dong RR, Katz J, Huang TT. 1997. On the structure of bow waves on a ship model. *J. Fluid Mech.* 346:77-115.

[18] Duncan, JH. 1981. An experimental investigation of breaking waves produced by a towed hydrofoil. *Proc. R. Soc. London Ser. A*. 377:331-348.

[19] Duncan JH. 2001. Spilling Breakers. *Annu. Rev. Fluid Mech.* 33:519-547.

[20] Duncan JH, Philoman V, Behres M, Kimmel J. 1994. The formation of spilling breaking water waves. *Phys. Fluids*. 6 (8) 2558-2560.

[21] Duncan JH, Liu X. 2003. The effects of surfactants on spilling breaking waves. *Nature.* 421: 520-523.

[22] Francis CT, Kirby JT. 1995. Dynamics of surf-zone turbulence in a spilling breaker. *Coastal Engineering.* 27:131-160.

[23] Francis CT, Kirby JT. 1996. Dynamics of surf-zone turbulence in a strong plunging breaker. *Coastal Engineering.* 24:177-204.

[24] Grilli ST, Svendsen IA, Subramanya R. 1997. Breaking Criterion and Characteristics for Solitary Waves on Slopes. *J. Waterway, Port, Coastal, and Ocean Engineering*. May/June: 102-112.

[25] Hendrickson KL. 2005. Navier-Stokes Simulation of Steep Breaking Water Waves with a Coupled Air-Water Interface. *PhD Thesis*, MIT/Ocean Engineering.

[26] Hirschfelder, JO. 1954. *Molecular theory of gases and liquids*. Wiley, New York. pp.630.

[27] Iafrati A, Di Mascio A, Campana EF. 2001. A level set technique applied to unsteady free surface flows. *Inter. J. Numer. Methods Fluids*. 35:281-297.

[28] Kanegsberg B, Kanegsberg K. 2003. Measuring Surface Tension: Part 2. A2C2 Magazine: Contamination Control for Life Sciences and Microelectronics. September.

[29] Kittle PA. 2002. Removing foam particles with a foam medium. A2C2 Magazine: Contamination Control for Life Sciences and Microelectronics. January.

[30] Kompenhans J, et al. 1998. *Particle Image Velocimetry:* A Practical Guide. Germany.

[31] Longuet-Higgins MS. 1974. Breaking Waves-In deep or shallow water. *Proc. 10th Conf. on Naval Hydro.*

[32] Longuet-Higgins MS, Cokelet ED. 1976. The deformation of steep surface waves on water I. A numerical method of computation. *Proc. R. Soc. Lond. A.* 350: 1-26.

[33] Longuet-Higgins MS, Cokelet ED. 1978. The deformation of steep surface waves on water II. growth of normal mode instabilities. *Proc. R. Soc. Lond. A.* 364: 1-28.

[34] Masutani G, Stenstrom, MK. 1984. A Review of Surface Tension Measuring Techniques, Surfactants, and Their Implication for Oxygen Transfer in Wastewater Treatment Plants. Published for the Water Resources Program, School of Engineering and Applied Sciences, UCLA.

[35] McKenna SP. 1997. The Influence of Surface Films on Interfacial Flow Dynamics. *Masters Thesis.* MIT/Ocean Engineering.

[36] Melling A. 1997. Tracer Particles and Seeding for Particle Image Velocimetry. *Meas. Sci Technol.* 8: 1406-1416.

[37] Melville, WK. 1996. The Role of Surfac-Wave Breaking in Air-Sea Interaction. *Ann. Rev. Fluid Mech.* 28: 279:321.

[38] Melville WK, Veron F, White CJ. 2002. The velocity filed under breaking waves: coherent structures and turbulence. *J. Fluid Mechanics.* 454: 203-233.

[39] Peirson WL. 1997. Measurement of surface velocities and shears at a wavy air-water interface using particle image velocimetry. *Experiments in Fluids.* 23:427-437.

[40] Peregrine DH. 1983. Breaking Waves on Beaches. *Ann. Rev. Fluid Mech.* 15:149-178.

[41] Perlin M, He J, Bernal L. 1996. An Experimental Study of Deep Water Plunging Breakers. *Phys. Fluids.* 8 (9) 2365-2374.

[42] Rapp RJ. 1986. Laboratory Measurements of Deep Water Breaking Waves. *PhD Thesis*, MIT Ocean Engineering.

[43] Rapp RJ, Melville WK. 1990. Laboratory Measurements of Deep-Water Breaking Waves. *Phil. Trans. R. Soc. Lond.* A 331: 735-800.

[44] Rosen, MJ. 1978. *Surfactants and Interfacial Phenomena.* John Wiley and Sons, USA. pp 149-153.

[45] Roth GI, Mascenik DT, Katz J. 1999. Measurements of the flow structure and turbulence within a ship bow wave. *Phys. Fluids.* 11(11):3512-3523.

[46] Shultz WW, Huh L, Griffin OM. 1994. Potential energy in steep and breaking waves. J. Fluid Mech. 278:201-228.

[47] Shuto, N., 1974. Nonlinear long waves in a channel of varied section. *Coastal Engineering in Japan.* 17, 1–12.

[48] Stansell P, MacFarlane C. 2002. Experimental Investigation of Wave Breaking Criteria Based on Wave Phase Speeds. *J. Phys. Oceanography.* 32: 1269-1283.

[49] Stokes, GG. 1847. On the theory of oscillatory waves. *Trans. Cambridge. Phil. Soc.* 8: 441-455.

[50] Tulin MP. 1996. Breaking of Ocean Waves and Downshifting. *Waves and Nonlinear Processes in Hydrodynamics*, ed. J Grue, B Gjevik, JE Weber, pp. 177-90. Dordrecht, Neth.: Kluwer Acad.

[51] Tsai CP, Chen HB, Hwung HH, Huang MJ. 2005. Examination of empirical formulas for shoaling and breaking on steep slopes. *Ocean Engineering.* 32: 469-483.

[52] Van Dorn WG, Pazan SE. 1975. Laboratory investigation of wave breaking. Part II: deep water waves. *Scripps Inst. Ocean. Ref. No. 75-21 AOEL Rep. No 71.* Scripps Inst. Ocean., San Diego, CA.

[53] Willert CE, Gharib, M. 1991. Digital particle image velocimetry. *Exp. Fluids.* 10:181-193.

[54] Whitman, W. "After the Sea-Ship." *Leaves of Grass*: Comprehensive Reader's Edition. New York University Press, 1965. pp. 263.

[55] Young T. 1805. An essay on the cohesion of fluids. *Phil. Trans. R. Soc. Lon.* 95: 65-87.